Department of Physics and Astronomy

University of Heidelberg

Master thesis

in Physics

submitted by

Philippe d'Argent

born in Stuttgart

December 2014

Amplitude analysis of $B^+ \rightarrow J/\psi\, K^+\pi^+\pi^-$ decays

at the LHCb experiment

This Master's thesis has been carried out by Philippe d'Argent

at the

Physikalisches Institut Heidelberg

under the supervision of

Prof. Dr. Ulrich Uwer

Abstract

This thesis investigates the resonant substructure of the decay $B^+ \to J/\psi\, K^+ \pi^+ \pi^-$. The study uses proton-proton collision data corresponding to an integrated luminosity of $3\,\text{fb}^{-1}$ recorded by the LHCb detector. Approximately $110\,000$ signal events are reconstructed and selected with a purity of 96%. A Dalitz plot analysis exploiting the full information provided by the seven-dimensional phase space is performed in order to disentangle the numerous intermediate state contributions. For this purpose, the spin-dependent angular distributions for various decay chains are derived in a covariant tensor formalism. The complex coupling constants to these decay channels, from which their fractional contributions can be inferred, are extracted from data by performing an unbinned maximum likelihood fit, where the theoretical distribution is corrected for the variation in selection efficiency over phase space. In doing so, a total of seventeen intermediate state components are identified. The prominent contribution is found to be the $K_1(1270)$ resonance in the decay modes $K_1(1270) \to K^+ \rho(770)$, $K_1(1270) \to K^*(892)\,\pi^+$, $K_1(1270) \to K_0^*(1430)\,\pi^+$ and $K_1(1270) \to K^+ f_0(980)$ with decay fractions 26.34%, 7.05%, 6.63% and 3.61%, respectively.

Kurzfassung:

In der vorliegenden Arbeit wird die Resonanzstruktur von $B^+ \to J/\psi\, K^+ \pi^+ \pi^-$ Zerfällen untersucht. Die benutzten Daten wurden in Proton-Proton Kollisionen mit dem LHCb-Detektor aufgenommen und entsprechen einer integrierten Luminosität von $3\,\text{fb}^{-1}$. Es können etwa $110\,000$ Signalereignisse mit einer Reinheit von 96% rekonstruiert und selektiert werden. Eine Dalitz-Analyse wird durchgeführt, um die verschiedenen Zwischenzustände zu trennen. Um die gesamte Information des sieben dimensionalen Phasenraums auszunutzen, werden die Winkelverteilungen für die verschiedenen Zerfallskanäle in einem kovarianten Tensorformalismus hergeleitet. Die komplexen Kopplungskonstanten und damit die relativen Beiträge der Zerfallskanäle werden durch einen Likelihood-Fit aus den gemessenen Daten extrahiert, wobei die Variation der Selektionseffizienz über den Phasenraum berücksichtigt wird. Die $K_1(1270)$ Resonanz mit den Zerfallskanälen $K_1(1270) \to K^+ \rho(770)$, $K_1(1270) \to K^*(892)\,\pi^+$, $K_1(1270) \to K_0^*(1430)\,\pi^+$ und $K_1(1270) \to K^+ f_0(980)$, mit den relativen Beiträge von 26.34%, 7.05%, 6.63% und 3.61% zum Zerfall $B^+ \to J/\psi\, K^+ \pi^+ \pi^-$, ist der dominierende Zwischenzustand.

Contents

Introduction

Although the predictions made by the Standard Model of particle physics have been probed with astonishing precision in numerous experiments all over the world, no experimental result contradicting the underlying theory has yet been observed. On the contrary, the discovery of the Higgs boson, the last missing elementary particle predicted by the Standard model in 2012 has confirmed the mechanism of spontaneous electroweak gauge symmetry breaking giving rise to fermion and electroweak gauge boson masses. Nonetheless, the Standard Model is known to be incomplete since several phenomena observed in nature remain unexplained. Among them are the predominance of matter over antimatter in the universe as well as the origin of dark matter and dark energy accounting for nearly 95% of the energy content in the universe. Furthermore, gravity is not incorporated in the Standard Model in contrast to the electromagnetic, strong and weak force.

The **L**arge **H**adron **C**ollider (LHC), the most powerful particle accelerator ever built, is dedicated to search for answers to these open questions. Where the primary purpose of the ATLAS and CMS experiments at the LHC resides in the search for new heavy particles thereby probing several Standard Model extensions such as supersymmetry, the LHCb experiment is devoted to precision measurements of b- and c-hadron decays. These decays provide an excellent laboratory for the spectroscopy of excited hadronic states which emerge as intermediate resonances in the transition to the ground state hadrons. The precise knowledge of the physical bound states is crucial for the understanding of the strong interaction. At the energy scale of hadrons, **Q**uantum **C**hromo **D**ynamics (QCD) is a strongly coupled field theory such that perturbative methods are not applicable. Therefore, the prediction of hadronic properties relies on the numerical evaluation of the field equations on a discrete space-time lattice (lattice QCD) or phenomenological approaches such as the quark constituent model. To validate these approaches, the identification of hadron resonances and the measurement of their basic properties such as masses, spins, parities and decay rates are essential. The most recent milestone was the discovery of the charged charmonium-like $Z(4430)$ resonance and with that, a new form of hadronic matter, most likely a tetraquark system.

This thesis investigates the resonant substructure of the decay $B^+ \to J/\psi\, K^+\pi^+\pi^-$.[1] The $K^+\pi^+\pi^-$ system comprises a broad spectrum of interfering exited kaon resonances with similar masses and large widths making it difficult to distinguish them. On top of that, there might be contributions from several charmonium(-like) resonances to the decay $B^+ \to J/\psi\, K^+\pi^+\pi^-$, where most of them need confirmation. An amplitude (or Dalitz plot) analysis is performed in oder to isolate the various intermediate state contributions based on the spin-dependent angular distributions of the decay products.

This thesis is organized as follows: Chapter 1 introduces the Standard Model of particle physics and the spectroscopic classification of mesons. Furthermore, the general formalism of the Dalitz plot analysis technique is presented. After laying out the theoretical framework, an overview of the current experimental status is given. Chapter 2 explains the amplitude

---

[1] The inclusion of the charge-conjugate decay is implied throughout the thesis.

formalism utilized to describe the dynamics of the decay $B^+ \to J/\psi\, K^+\pi^+\pi^-$ in detail. The experimental apparatus and the collected data sample are discussed in Chapter 3. Chapter 4 introduces important analysis techniques necessary to extract physical parameters from the measured data while Chapter 5 covers the reconstruction and selection of the signal decay. There are several experimental effects which have to be accounted for when interpreting the observed data. Where Chapter 6 deals with the non-uniform selection efficiency, the momentum resolution of the detector is studied in Chapter 7. The results of the amplitude analysis are presented in Chapter 8, followed by a discussion of the limitations and further enhancements of the method. Finally, Chapter 9 summarizes the achievements of the analysis and gives an outlook to prospective applications of the developed analysis methods.

1 Dalitz plots and meson spectroscopy

This chapter gives a brief overview of the Standard Model focusing on the particle content and the formation of bound states, followed by a summary of the spectroscopic classification of mesons. Moreover, the Dalitz plot analysis technique and its application in the study of the resonance structure in $B^+ \to J/\psi\, K^+\pi^+\pi^-$ decays is discussed.

1.1 The Standard Model of particle physics

The Standard Model builds the foundation of modern particle physics.[2] It describes the properties of the known elementary particles and their mutual interactions. Figure 1.1 summarizes the particle content of the Standard Model along with the measured masses, charges and spins.

The fundamental building blocks of matter are particles of spin $\frac{1}{2}$ called fermions, which are classified into leptons and quarks. There are three different "flavours" of leptons, where each contains a charged particle (e^-, μ^- or τ^-) along with its neutral counterpart ν_e, ν_μ or ν_τ. Similarly, quarks are grouped into three generations ordered by their mass. Each generation contains an "up-type" quark of charge $+\frac{2}{3}e$ and a "down-type" quark of charge $-\frac{1}{3}e$. Furthermore, for each fermion a corresponding antiparticle having the same mass but reversed additive quantum numbers exists.

The Standard Model combines the electroweak theory developed by Glashow [2], Salam [3] and Weinberg [4] with the theory of the strong interactions, **Q**uantum **C**hromo **D**ynamics (QCD). The mediators of the fundamental interactions are the gauge bosons of spin 1.

The electromagnetic force, mediated by the photon γ, is responsible for binding atoms and molecules together. The photon itself being electric neutral couples to electric charge. The fact that the photon is massless leads to the long range of electromagnetic interactions.

In contrast, the weak interaction mediated by the massive $W^\pm$ and Z^0 bosons is short ranged. The weak force has the unique property that it is able to change the quark flavour and is thus responsible for radioactive processes such as the nuclear β-decay. Furthermore, weak interactions are not invariant under the parity transformation, unlike interactions via the electromagnetic or strong force.[3]

The exchange particles of the strong interaction are eight massless gluons g coupling to color charge (red, blue, green). Only quarks and gluon themselves carry color charge such that leptons do not participate in strong interactions. The color charge of the gluons enables gluon-gluon couplings with the consequence that the QCD coupling "constant" has a strong energy dependency.[4] At low energies, the QCD coupling increases leading to a phenomenon called (color) confinement, which means that free quarks cannot be

---

[2]For an introduction into the underlying theory of the Standard Model see *e.g.* Ref. [1].

[3]The parity transformation inverts the spatial coordinates: $\vec{x} \to -\vec{x}$.

[4]The coupling constant determines the strength of the interaction.
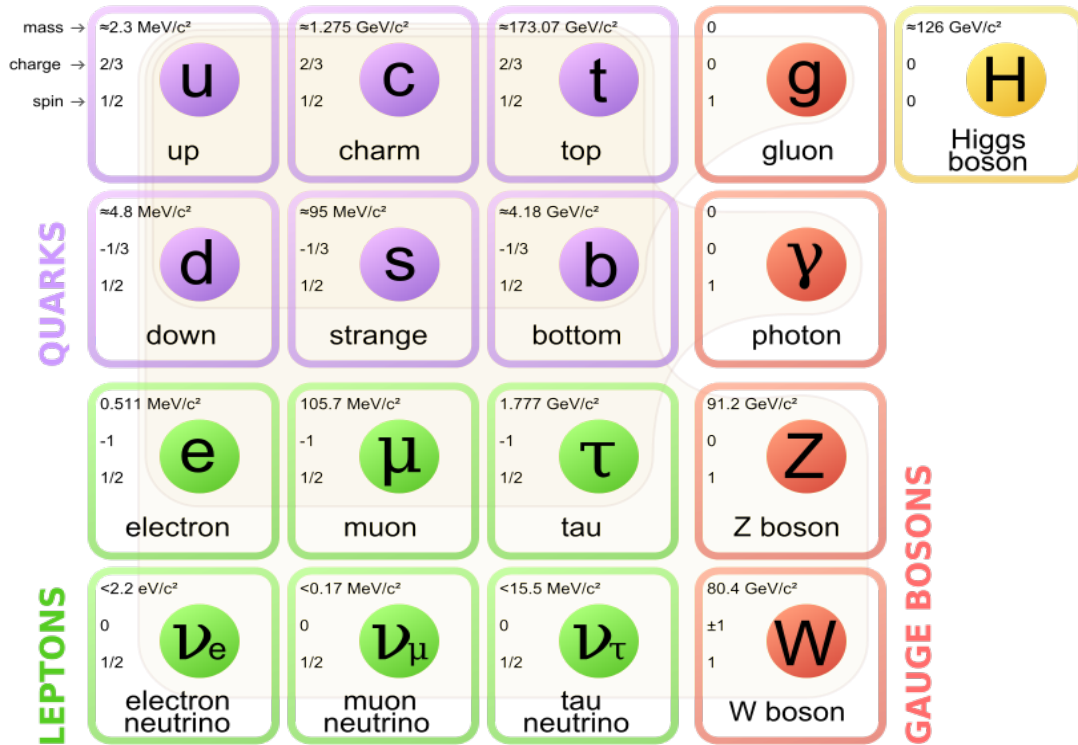
Figure 1.1: Fundamental particles of the Standard Model with their measured masses, charges and spins. Figure taken from Ref. [6].

observed. Quarks are only observable in composite, color-neutral bound states, called hadrons.[5] However, quarks are asymptotically free at high energies (or small distances).

The internal structure of hadrons is a complicated synergy of valence quarks, which define the basic properties of the hadron such as spin and parity, as well as virtual quark anti-quark pairs and virtual gluons. Hadrons are classified into baryons and mesons according to their (valence) quark content. While mesons are formed from one quark and one anti-quark ($q\bar{q}$), baryons are composed of three quarks (qqq) such as the proton with quark content uud. Other combinations, for example tetra quark states $qq\bar{q}\bar{q}$, are supported by QCD as well [5].

---

[5]Either the combination of a color with its respective anti-color or the combination of all thee (anti-)colors result in a color-neutral or "white" state.

1.2   Meson spectroscopy

Despite the fact that there are only 21 combinatoric possibilities to form quark anti-quark pairs out of six quark species, a whole plethora of mesonic states is observed in experiments. Figure 1.2 shows the light meson spectrum. The meson spectrum can be understood in analogy to the spectral emission spectrum of the hydrogen atom. While the energy levels of the hydrogen atom are caused by the electromagnetic force, exited mesonic states are a result of the strong interaction. Within the constituent quark model, different mesonic states of the same quark content arise as a result of the intrinsic spins of the two quarks being either parallel or antiparallel aligned leading to a total spin of $S = 1$ or $S = 0$. Furthermore, the quark-antiquark system can exhibit an orbital excitation depending on the relative angular momentum between the quarks ($L = 0, 1, 2, \ldots$) as well as a radial excitation ($n = 1, 2, 3, \ldots$). Spin S and orbital angular momentum L couple to a state of total angular momentum J. Mesons are classified into types according to their total angular momentum and parity $P = (-1)^{L+1}$ as shown in Table 1.1.[6] The pseudoscalar ground states of the $u\bar{d}$, $u\bar{s}$ and $u\bar{b}$ systems named pion, kaon and B-meson as well as the $c\bar{c}$ ground state named J/ψ meson with quantum numbers $J^P = 1^-$ are of particular importance for this analysis.

The observation of the $X(3872)$ meson in the decay mode $B^+ \rightarrow X(3872)\,K^+$ with $X(3872) \rightarrow J/\psi\,\pi^+\,\pi^-$ by the Belle collaboration in 2003 [7] has triggered a resurgence of interest in particle spectroscopy. While the quantum numbers of the $X(3872)$ meson have been measured to be $J^{PC} = 1^{++}$ by the LHCb collaboration in 2013 [8], its nature is still unclear. The interpretations range from conventional charmonium ($c\bar{c}$ bound state) [9] to exotic states as $D^{*0}\bar{D}^0$ molecules [10], tetra quarks ($c\bar{c}q\bar{q}$) [11] or quark-gluon hybrids ($c\bar{c}g$) [12]. With the discovery of the charged charmonium-like $Z^+(4430)$ state in the decay mode $B^0 \rightarrow Z^-(4430)\,K^+$ with $Z^-(4430) \rightarrow \psi(2S)\pi^-$ by the LHCb collaboration in 2014 [13] a new era in particle spectroscopy beyond the established bound states of quarks (mesons $q\bar{q}$ and baryons qqq) has been heralded. The charged nature of the $Z(4430)$ state excludes a conventional charmonium interpretation making it a prime candidate for a tetra quark state with minimal quark content $c\bar{c}u\bar{d}$.

Table 1.1: Meson types.

Type	Notation	J^P
scalar	S	0^+
pseudoscalar	P	0^-
vector	V	1^-
axialvector	A	1^+
tensor	T_+	2^+
pseudotensor	T_-	2^-

---

[6]The intrinsic parity defines how the state transforms under space inversion.

$\nu \approx m[\text{GeV}]$

$$\frac{2S+1}{n} L_J = J^{PC}$$

$^3_2P_2 = 2^{++}$ $\quad$ $^3_2P_1 = 1^{++}$ $\quad$ $^3_1D_3 = 3^{--}$ $\quad$ $^3_1D_2 = 2^{--}$

a$_2$(1700)
K$_2$*(1980)
f$_2$(2010)
f$_2$(1950)

a$_1$(1640)

ρ$_3$(1690)
K*$_3$(1780)
ω$_3$(1670)
φ$_3$(1850)

K$_2$(1820)

π(1800)
K(1830)
η(1760)

2

π$_2$(1670)
K$_2$(1770)
η$_2$(1645)
η$_2$(1870)

ρ(1700)
K*(1680)
ω(1650)

$^1_3S_0 = 0^{-+}$ $\quad$ $^3_3S_1 = 1^{--}$

$^3_1P_2 = 2^{++}$ $\quad$ $^3_1P_1 = 1^{++}$ $\quad$ $^1_1D_2 = 2^{-+}$ $\quad$ $^3_1D_1 = 1^{--}$

a$_2$(1320)
K$_2$*(1430)
f$_2$(1270)
f$_2$'(1525)

a$_1$(1260)
K$_{1a}$
f$_1$(1285)
f$_1$(1420)

π(1300)
K(1460)
η(1295)
η(1440)

ρ(1450)
K*(1410)
ω(1420)
φ(1680)

1

a$_0$(1450)
K$_0$*(1430)
f$_0$(1370)
f$_0$(1710)

b$_1$(1235)
K$_{1b}$
h$_1$(1170)
h$_1$(1380)

n

$^1_2S_0 = 0^{-+}$ $\quad$ $^3_2S_1 = 1^{--}$

$^3_1P_0 = 0^{++}$ $\quad$ $^1_1P_1 = 1^{+-}$

π
K
η
η'

ρ(770)
K*(892)
ω(782)
φ(1020)

0

L

$^1_1S_0 = 0^{-+}$ $\quad$ $^3_1S_1 = 1^{--}$

0 $\qquad$ 1 $\qquad$ 2 $\qquad$ L

Figure 1.2: Spectrum of mesonic states formed from the three light quarks u, d, s. Mesons are classified according to their total angular momentum J, relative angular momentum L, spin multiplicity $2S + 1$ and radial excitation n. The horizontal axis gives the angular momentum L and the vertical axis the radial number $v = n + L - 1$ which is an approximate mass scale $v \approx m[\text{GeV}]$. The shaded states are established while the others need confirmation. Figure taken from [14].

1.3 Dalitz Plots

This section introduces the basic concepts of a Dalitz plot analysis. A Dalitz plot is a visual representation of a decay process providing access to the dynamics of the interaction. The first application of this method was the determination of spin and parity of the K^+ meson ($J^P = 0^-$) using $K^+ \to \pi^+\pi^+\pi^-$ decays by R. H. Dalitz in 1953 [15]. It has been established as an important analysis technique in particle physics and, in particular, particle spectroscopy with a broad range of applications as discussed in the following.

1.3.1 Differential decay rate

In quantum field theory, the transition from an initial state $|i\rangle$ to a final state $|f\rangle$, with four-momenta p_i and p_f respectively, is described by the so-called scattering matrix

$$\langle f|S|i\rangle = \delta_{fi} + i\,(2\pi)^4\,\delta^4(p_f - p_i) \cdot \mathcal{M} \tag{1.1}$$

which is separated into an interacting and a non-interacting part [1]. The first term in Eq. 1.1 denotes the case of identical initial and final states which is henceforth excluded while the non-trivial scattering case is described by the transition amplitude $\mathcal{M}$ given by the underlying physics process. The delta function in Eq. 1.1, $\delta^4(p_f - p_i)$, ensures energy-momentum conservation.

Now, consider the decay of a particle with mass m_0 and four-momentum p_0 into n particles with four momenta $p_i = (E_i, \vec{p}_i)$ $(i = 1, 2, \ldots, n)$. The decay rate, defined as the transition probability per unit time is given by [1]

$$\mathrm{d}\Gamma = \frac{1}{2m_0}\,|\mathcal{M}|^2\,\mathrm{d}\phi_n \tag{1.2}$$

where the n-body phase space element is defined as

$$\mathrm{d}\phi_n = (2\pi)^4\,\delta^4\left(p_0 - \sum_{i=1}^{n} p_i\right) \prod_{i=1}^{n} \frac{\mathrm{d}^3\vec{p}_i}{2(2\pi)^3 E_i}\,. \tag{1.3}$$

As indicated in Eq. 1.3, each final state particle contributes three degrees of freedom, manifested in their three-momentum, summing up to $3n$ degrees of freedom in total. Due to four-momentum conservation four of them are redundant resulting in $3n - 4$ degrees of freedom. After integrating over the delta function in Eq. 1.3, the phase space element can be written in terms of the $3n - 4$ independent kinematic variables:

$$\mathrm{d}\phi_n = \phi_n(X)\,\mathrm{d}X \tag{1.4}$$

where X is the set of all independent kinematic variables and $\phi_n(X)$ is the phase space density function which accounts for the kinematic constraints among the final state momenta. Convenient choices for the kinematic variables are the invariant mass combinations of the final state particles:

$$m_{ij}^2 = (p_i + p_j)^2 \tag{1.5}$$

$$m_{ijk}^2 = (p_i + p_j + p_k)^2\,. \tag{1.6}$$

However, only $3n - 7$ of them are independent. These specify the relative orientation of the n three-momenta $\{\vec{p}_i\}$ in a chosen reference frame. The remaining degrees of freedom are three Euler-angles which describe the relative orientation of the reference system with respect to the initial state. Note that deviations from the phase space distribution $\phi_n(X)$ of the kinematic variables are due to the dynamics of the interaction. Therefore, the underlying physics, *i.e.* $|\mathcal{M}|^2$, can be investigated by measuring the differential decay width. In fact, this is the fundamental concept of a Dalitz plot analysis which is further illustrated by the example of a three-body decay in the next subsection and then extended to the more complex case of $B^+ \to J/\psi\,K^+\pi^+\pi^-$ decays in Sec. 1.4.

1.3.2 Dalitz analysis of three-body decays

Let the decay $D_s^+ \to K^+ K^- \pi^+$ serve as an example of a three body decay of a pseudo-scalar particle to all pseudoscalar final states. Since only spin-0 particles are involved, there is no preferred direction in space so that the overall orientation of the system can be integrated out. As consequence, two invariant mass combinations, *e.g.* $m_{K^+K^-}^2$ and $m_{K^-\pi^+}^2$, are sufficient to describe the phase space fully. In this specific choice of independent kinematic variables, the phase space distribution is flat so that the differential decay rate can be written as [1]:

$$\mathrm{d}\Gamma = \frac{1}{(2\pi)^3} \frac{1}{32 m_{D_s}^3} |\mathcal{M}(m_{K^+K^-}^2, m_{K^-\pi^+}^2)|^2 \, \mathrm{d}m_{K^+K^-}^2 \, \mathrm{d}m_{K^-\pi^+}^2 \, . \tag{1.7}$$

From Equation 1.7 follows that the dynamics of a three body decay can be visualized by a scatter plot of $m_{K^+K^-}^2$ versus $m_{K^-\pi^+}^2$, also referred to as Dalitz plot. If $|\mathcal{M}|^2$ is constant, the Dalitz plot distribution is uniform within the boundary fixed by energy-momentum conservation. Any visible structure in the Dalitz plot provides immediately information on $|\mathcal{M}|^2$. For example, the decay $D_s^+ \to K^+ K^- \pi^+$ can proceed via an intermediate resonance as $D_s^+ \to (\phi(1020) \to K^+ K^-)\pi^+$ resulting in a resonance band around $m_{K^+K^-} = m_{\phi(1020)} \approx 1020\,\mathrm{MeV}$ as shown in Fig. 1.3. In general, not only one, but many intermediate resonances contribute to a common final state. Therefore, the total amplitude is given by the coherent sum over the intermediate-state amplitudes $\mathcal{A}_i$:

$$|\mathcal{M}|^2 = \left| \sum_i a_i \, \mathcal{A}_i \right|^2 \tag{1.8}$$

where the complex couplings $a_i = |a_i| e^{i\phi_i}$ describe the relative strength and phase between the amplitudes. The fractional contribution of a single decay channel is defined as the phase space integral of the respective amplitude squared divided by the integral of the coherent sum of all amplitudes squared:

$$F_j = \frac{\int |a_j \, \mathcal{A}_j(X)|^2 \, \mathrm{d}\phi(X)}{\int |\sum_i a_i \, \mathcal{A}_i(X)|^2 \, \mathrm{d}\phi(X)} \, . \tag{1.9}$$

Note that the sum of the fractions F_j does not necessarily sum up to unity due to potential interference effects. These are quantified by the interference term fractions, defined as

$$F_{jk} = \frac{\int 2\,\Re(a_j \, \mathcal{A}_j \, a_k^* \, \mathcal{A}_k^*) \, \mathrm{d}\phi(X)}{\int |\sum_i a_i \, \mathcal{A}_i(X)|^2 \, \mathrm{d}\phi(X)} \tag{1.10}$$

with $j > k$, which are not positive definite in contrast to the fractions F_j. Thus, the overall normalization is given by:

$$\sum_j F_j + \sum_{j>k} F_{jk} = 1 \, . \tag{1.11}$$

An amplitude analysis aims to measure the couplings a_i from which the corresponding branching fractions can be determined. Furthermore, the intensity pattern across the Dalitz plane depends on the angular momentum between the final state particles as well as on the quantum numbers, *i.e.* spin and parity, of the involved intermediate states. In this way, the Dalitz plot allows to infer properties of short-lived resonances which are otherwise not accessible.

To summarize, Dalitz plots are a powerful tool to measure the mass, decay width, spin and parity of particles in addition to branching fractions and interference effects.
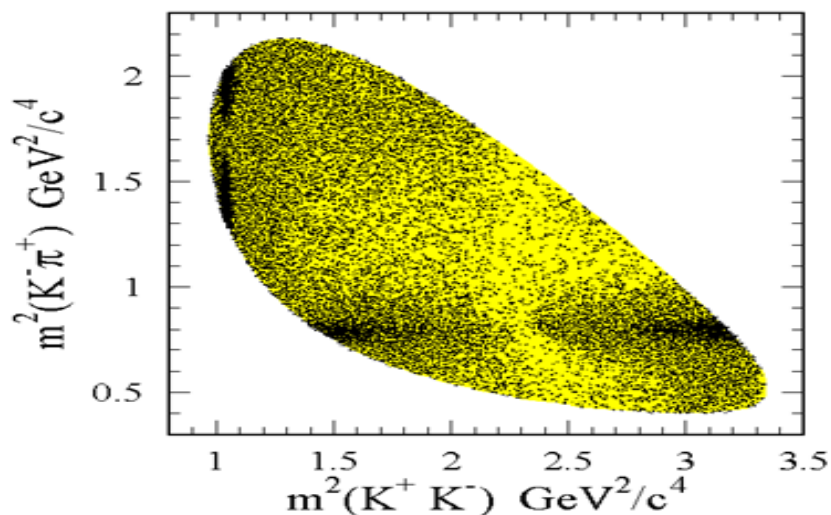
Figure 1.3: Dalitz plot for $D_s^+ \to K^+ K^- \pi^+$ decays. The vertical band corresponds to the $\phi(1020)$ resonance and the horizontal band corresponds to the $K^*(892)$ resonance. The changing intensity along the resonance bands is a result of the intrinsic spins of the intermediate states. Figure taken from Ref. [16].

1.4 Amplitude analysis of $B^+ \to J/\psi\, K^+\pi^+\pi^-$ decays

This analysis studies the resonant structure of $B^+ \to J/\psi\, K^+\pi^+\pi^-$ decays. The light meson spectrum in Fig. 1.2 comprises several exited Kaon resonances which are expected to contribute to $B^+ \to J/\psi\, K^+\pi^+\pi^-$ decays as intermediate states. This cornucopia of broad, overlapping resonances which, in addition, interfere renders it impossible to identify the resonances based on their mass alone. Therefore, an amplitude analysis is required exploiting the full phase space information in order to disentangle the various contributions. In this section, the phase space variables are introduced, followed by a brief overview of the current experimental status.

1.4.1 Phase space variables

Since the J/ψ meson is a vector particle, it is necessary to choose a quantization axis (z-axis) in order to define the polarization state of the J/ψ meson, *i.e.* its spin projection to the z-axis. For this purpose, the following coordinate system is defined in the rest frame of the $K^+\pi^+\pi^-$ system:

- The z-axis is chosen to be the normal to the $K^+\pi^+\pi^-$ decay plane:

$$\hat{e}_z := \hat{p}_{\pi^+}^{(K\pi\pi)} \times \hat{p}_{\pi^-}^{(K\pi\pi)} \tag{1.12}$$

  where $\hat{e}_z$ is the unit vector in z-direction and $\hat{p}_i^f$ denotes the unit vector in direction of the three-momentum of particle i in the rest frame of system f.

- Once the z-axis is chosen, the physical system is invariant under rotations around it removing one of the three degrees of freedom required to describe the orientation of the final system, *cf.* Sec. 1.3.1. The x-axis is arbitrarily chosen so that the J/ψ momentum lies in the x-z-plane. This implies for the y-axis:

$$\hat{e}_y := \hat{e}_z \times \hat{p}_{J/\psi}^{(K\pi\pi)} \tag{1.13}$$

  and consequently

$$\hat{e}_x := \hat{e}_y \times \hat{e}_z\,. \tag{1.14}$$

In that frame, the angular observables are defined as the polar and azimuthal angles of the J/ψ momentum:

$$\cos\theta := \hat{p}_{J/\psi}^{(K\pi\pi)} \cdot \hat{e}_z \tag{1.15}$$

$$\phi := 0 \tag{1.16}$$

where the latter is fixed by definition and a residual azimuthal rotation around the J/ψ momentum. The rotation around $\hat{p}_{J/\psi}^{(K\pi\pi)}$ is specified by the angle between the decay plane containing the J/ψ and π^+ and the decay plane containing the J/ψ and K^+:

$$\cos\chi := (\hat{p}_{J/\psi}^{(K\pi\pi)} \times \hat{p}_{\pi^+}^{(K\pi\pi)}) \cdot (\hat{p}_{J/\psi}^{(K\pi\pi)} \times \hat{p}_{K^+}^{(K\pi\pi)}) \tag{1.17}$$

$$\sin\chi := \left[(\hat{p}_{J/\psi}^{(K\pi\pi)} \times \hat{p}_{\pi^+}^{(K\pi\pi)}) \times (\hat{p}_{J/\psi}^{(K\pi\pi)} \times \hat{p}_{K^+}^{(K\pi\pi)})\right] \cdot (\hat{p}_{J/\psi}^{(K\pi\pi)} + \hat{p}_{K^+}^{(K\pi\pi)})\,. \tag{1.18}$$

Figure 1.4 illustrates the definition of the angles θ and χ. Note that $\hat{p}_{J/\psi}^{(K\pi\pi)} = \hat{p}_{B^+}^{(K\pi\pi)}$ and thus the chosen angular basis specifies, indeed, the orientation of the final state with respect to the initial state. The angular observables given by the set $\Omega = (\cos\theta, \chi)$ in combination with five invariant mass combinations define the total set of seven independent kinematic variables:

$$X = (m_{K^+\pi^+\pi^-}^2, m_{K^+\pi^-}^2, m_{\pi^+\pi^-}^2, m_{J/\psi\,\pi^+\pi^-}^2, m_{J/\psi\,\pi^+}^2, \cos\theta, \chi) \tag{1.19}$$

which are henceforth denoted as phase space variables while the subset

$$D = (m_{K^+\pi^+\pi^-}^2, m_{K^+\pi^-}^2, m_{\pi^+\pi^-}^2, m_{J/\psi\,\pi^+\pi^-}^2, m_{J/\psi\,\pi^+}^2) \tag{1.20}$$

refers to the Dalitz plot variables only. Finally, the differential decay rate follows from Eq. 1.2:

$$\frac{\mathrm{d}\Gamma}{\mathrm{d}X} = \frac{1}{2m_{B^+}} |\mathcal{M}(X)|^2 \, \phi_4(X). \tag{1.21}$$

In contrast to three-body decays, the four-body phase space is not uniform in any set of independent kinematic variables, but proportional to the square-root of the inverse of the so-called Grahm determinant [17]:

$$\phi_4(X) = \frac{\pi^2}{32\,m_{B^+}^2} \left(\begin{vmatrix} x_{11} & x_{12} & x_{13} & x_{14} \\ x_{21} & x_{22} & x_{23} & x_{24} \\ x_{31} & x_{32} & x_{33} & x_{34} \\ x_{41} & x_{42} & x_{43} & x_{44} \end{vmatrix} \right)^{-\frac{1}{2}} \tag{1.22}$$

where $x_{ij} := p_i \cdot p_j$ and $i = (1, 2, 3, 4)$ refers to $(J/\psi, K^+, \pi^+, \pi^-)$.
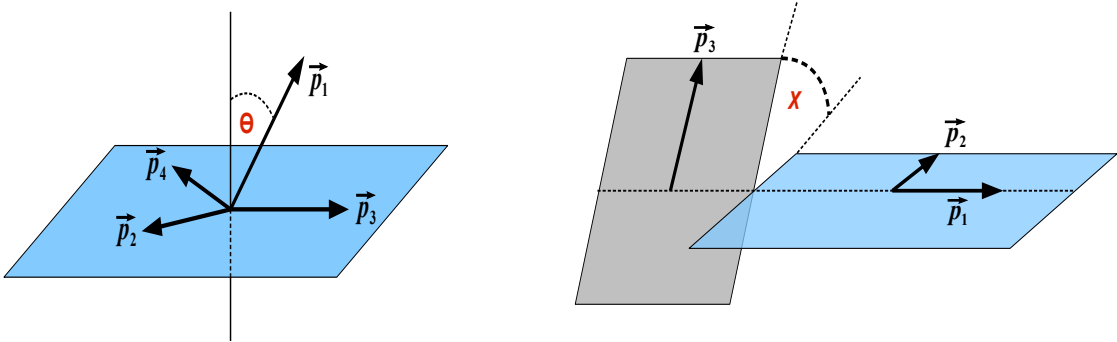
Figure 1.4: Illustration of the angles θ (left) and χ (right). Final state momenta measured in the $K^+\pi^+\pi^-$ rest frame are labeled as $\vec{p}_i$ where the index $i = (1, 2, 3, 4)$ corresponds to the $J/\psi, K^+, \pi^+$ and π^- meson, respectively.

1.4.2 Previous measurement

The first observation of the exclusive decay process $B^+ \to J/\psi\, K_1^+(1270)$ in $B^+ \to J/\psi\, K^+\pi^+\pi^-$ decays was reported by the Belle collaboration in 2001 [18]. The branching fraction was estimated to be

$$\mathcal{B}(B^+ \to J/\psi\, K_1^+(1270)) = (1.30 \pm 0.34\,(\text{stat}) \pm 0.31\,(\text{syst})) \cdot 10^{-3} \qquad (1.23)$$

by performing an one-dimensional fit to the invariant mass of the $K^+\pi^+\pi^-$ system based on approximately 50 signal events. No further evident structure was observed due to the limited statistics.

After collecting more data, the Belle collaboration realized the first (and up to know only) measurement of the resonance structure in $B^+ \to J/\psi\, K^+\pi^+\pi^-$ decays in 2011 [19]. The fractional contributions, *cf.* Eq. 1.9, listed in Table 1.2 were determined by performing an amplitude fit in the tree invariant mass combinations $m^2(K^+\pi^+\pi^-)$, $m^2(K^+\pi^-)$ and $m^2(\pi^+\pi^-)$ based on approximately $8\,000$ signal events. This simplified approach corresponds to a three-body Dalitz plot analysis of $m^2(K^+\pi^-)$ and $m^2(\pi^+\pi^-)$ in slices of $m^2(K^+\pi^+\pi^-)$ equivalent to integrate over degrees of freedom describing the J/ψ polarization and momentum relative to the $K^+\pi^+\pi^-$ system. In doing so, different orbital angular momentum couplings between the J/ψ meson and the $K^+\pi^+\pi^-$ system can not be considered. It is assumed that the decay proceeds exclusively in the lowest possible angular momentum state compatible with angular momentum conservation. Furthermore, contributions from exotic resonances, for example $B^+ \to K^+\,(X(3872) \to J/\psi\,\pi^+\pi^-)$ decays, cannot be studied and have to be neglected.

This analysis represents the first attempt to study $B^+ \to J/\psi\, K^+\pi^+\pi^-$ decays in full seven-dimensional phase space.

Table 1.2: Fractional contributions to $B^+ \to J/\psi\, K^+\pi^+\pi^-$ decays. The first uncertainty is statistical and the second systematic. Values taken from Ref. [19].

Decay mode	Fraction F_i [%]
$B \to J/\psi\, [K_1(1270) \to K^*(892)\,\pi]$	$23.2 \pm 1.7 \pm 5.8$
$B \to J/\psi\, [K_1(1270) \to K\,\rho(770)]$	$38.3 \pm 1.6 \pm 3.6$
$B \to J/\psi\, [K_1(1270) \to K\,\omega(782)]$	$0.45 \pm 0.17 \pm 0.14$
$B \to J/\psi\, [K_1(1270) \to K_0^*(1430)\,\pi]$	$1.57 \pm 0.52 \pm 0.49$
$B \to J/\psi\, [K_1(1400) \to K^*(892)\,\pi]$	$22.3 \pm 2.6 \pm 3.6$
$B \to J/\psi\, [K^*(1410) \to K^*(892)\,\pi]$	$4.7 \pm 1.6 \pm 1.5$
$B \to J/\psi\, [K_2^*(1430) \to K^*(892)\,\pi]$	$8.8 \pm 1.1 \pm 1.1$
$B \to J/\psi\, [K_2^*(1430) \to K\,\rho(770)]$	2.33 (fixed)
$B \to J/\psi\, [K_2^*(1430) \to K\,\omega(782)]$	0.036 (fixed)
$B \to J/\psi\, [K_2(1580) \to K^*(892)\,\pi]$	$1.87 \pm 0.58 \pm 0.50$
$B \to J/\psi\, [K_2(1580) \to K\,\rho(770)]$	$4.24 \pm 0.62 \pm 1.10$
$B \to J/\psi\, [K_2(1770) \to K^*(892)\,\pi]$	$1.64 \pm 0.55 \pm 0.61$
$B \to J/\psi\, [K_2(1770) \to K_2^*(1430)\,\pi]$	$1.00 \pm 0.28 \pm 0.20$
$B \to J/\psi\, [K_2(1770) \to K\,f_0(980)]$	$0.34 \pm 0.17 \pm 0.11$
$B \to J/\psi\, [K_2(1770) \to K\,f_2(1270)]$	$1.24 \pm 0.33 \pm 0.22$
$B \to J/\psi\, [K_2^*(1980) \to K^*(892)\,\pi]$	$7.39 \pm 0.73 \pm 0.95$
$B \to J/\psi\, [K_2^*(1980) \to K\,\rho(770)]$	$6.13 \pm 0.58 \pm 0.59$
$B \to J/\psi\, K\pi\pi$ (non resonant)	$15.2 \pm 1.3 \pm 2.8$

2 Amplitude formalism

The main challenge of an amplitude analysis is to construct a signal **p**robability **d**ensity **f**unction (PDF) which accurately describes both; the kinematic and dynamical properties of the decay. For this purpose, the signal PDF is defined, based on the differential decay rate in Eq. 1.21, in terms of the phase space variables X as

$$\mathcal{P}(X|a) = \frac{\left|\sum_i a_i \, \mathcal{A}_i(X)\right|^2 \phi_4(X)}{\int \left|\sum_i a_i \, \mathcal{A}_i(X)\right|^2 \phi_4(X) \, \mathrm{d}X} \tag{2.1}$$

where the set of coupling constants $a = (a_1, a_2, \dots)$ is to be measured from data as described in Chapter 4.

To construct the Lorentz invariant amplitudes $\mathcal{A}_i$, the isobar approach is used which assumes that the decay process can be factorized into subsequent two-body decays [20–22]. In the isobar model, the final state particles are grouped into a state of definite quantum numbers (called "isobar" state [21]) and a recoil system, which might be a single particle or a isobar state as well, at each node of the decay tree.[7] It is assumed that the subsequent decay of the isobar completely factorizes from the recoil system, *i.e.* there is no rescattering involved. This approximation reduces the four-body problem to a series of two-body problems.

For illustration purposes, assume, for the moment, that the decay $B^+ \to J/\psi \, K^+ \pi^+ \pi^-$ proceeds exclusively via the cascade decay $B^+ \to J/\psi \, R_1$, where subsequently $R_1 \to \pi^+ R_2$ followed by $R_2 \to K^+ \pi^-$ as depicted in Fig. 2.1 for the example of $R_1 = K_1(1270)$ and $R_2 = K^*(892)$. In that case, the decay amplitude[8] $\langle J/\psi \, K \pi \pi | \mathcal{M} | B \rangle$ can be expanded in terms of the quasi two-body decay amplitudes $\langle R_1 \, J/\psi | \mathcal{M} | B \rangle$, $\langle R_2 \, \pi | \mathcal{M} | R_1 \rangle$ and $\langle K \pi | \mathcal{M} | R_2 \rangle$ as

$$\begin{aligned}
\mathcal{A} &= \langle J/\psi \, K \pi \pi | \mathcal{M} | B \rangle \\
&= \sum_{m_1, m_2} \langle K \pi | \mathcal{M} | R_2(m_2) \rangle \, \Delta(R_2) \, \langle R_2(m_2) \, \pi | \mathcal{M} | R_1(m_1) \rangle \, \Delta(R_1) \, \langle R_1(m_1) \, J/\psi | \mathcal{M} | B \rangle \, F_{L_B}(B)
\end{aligned} \tag{2.2}$$

with $\Delta(R_i) = F_{L_i}(R_i) \, \mathcal{T}(R_i)$. Here, $F_{L_B}(B)$ and $F_{L_i}(R_i)$ are the Blatt-Weisskopf centrifugal barrier form factors for the B^+ and R_i decay vertex, where the subscript refers to the relative angular momentum L_i among the daughter particles, and $\mathcal{T}(R_i)$ is the resonance propagator. Section 2.1 discusses the parameterization of the barrier factors and several models for the resonance line shapes. The coherent sum over the intermediate state polarizations is applied since the spin projections m_i are unobservable.

From Equation 2.2 follows the general amplitude structure, valid for all decay topologies,

$$\mathcal{A} = F_{L_B}(B) \, [F_{L_1}(R_1) \, \mathcal{T}(R_1)] \, [F_{L_2}(R_2) \, \mathcal{T}(R_2)] \, \mathcal{S}_f \tag{2.3}$$

where the so-called spin factor S_f accounts for angular momentum conservation.

---

[7]The isobar states are usually interpreted as intermediate resonances but this is not mandatory, *cf.* Sec. 2.2.5.

[8]Here $\mathcal{M}$ denotes a general transition operator.
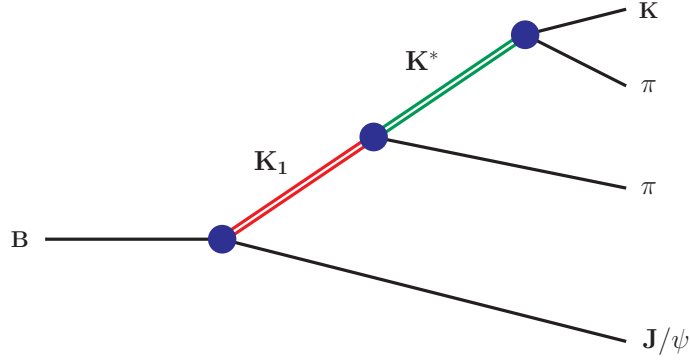
Figure 2.1: Schematic view of the decay $B^+ \to J/\psi \, K_1(1270)^+$ followed by $K_1(1270)^+ \to \pi^+ K^*(892)$ and $K^*(892) \to K^+\pi^-$.

In the context of this thesis, the spin factors for $B^+ \to J/\psi \, K^+\pi^+\pi^-$ decays are calculated in a covariant tensor formalism based on Refs. [23–27], which is discussed in detail in Sec. 2.2 and validated in Sec. 2.3.

2.1 Resonance line shapes and form factors

2.1.1 Blatt-Weisskopf form factors

The centrifugal barrier effect in a decay $R \to A\,B$ can be motivated by considering the Schrödinger equation for the radial wave function $\psi(r)$ in a central field:

$$\left[-\frac{1}{2\mu}(\partial_r^2 + \frac{2}{r}\partial_r) + \frac{L(L+1)}{2\mu r^2} + V(r) \right] \psi(r) = E\,\psi(r) \qquad (2.4)$$

where r is the particle separation, μ is the reduced mass of the system, L is the orbital angular momentum quantum number and $V(r)$ is the interaction potential. A higher angular momentum creates a higher centrifugal barrier $\frac{L(L+1)}{2\mu r^2}$ and decreases the transition probability. The Blatt-Weisskopf form factors F_L in Eq. 2.2 account for the influence of the centrifugal barrier on the transition amplitudes [28, 29]. In particular, the form factors ensure the correct behavior of the amplitudes at the threshold $q \to 0$, where the breakup momentum q is given by the magnitude of the three-momentum of particle A (or B) in the rest frame of the decaying particle R:

$$q^2 = \frac{[m^2(A\,B) - (m(A) + m(B))^2]\,[m^2(A\,B) - (m(A) - m(B))^2]}{4\,m^2(A\,B)} . \qquad (2.5)$$

The Blatt-Weisskopf functions have the asymptotic behavior $F_L(q) \propto q^L$ (for $q \to 0$) near threshold, physically motivated by the fact that it is difficult for slowly moving particles to generate enough angular momentum, L, to account for the resonance spin. Table 2.1 gives the explicit expressions of $F_L(q)$ for $L = 0, 1, 2$ which are derived in Ref. [29] by assuming a square well (interaction) potential with radius r_{BW}. The form factors are normalized to unity for $q = 1/r_{BW}$ whereby the effective interaction radius r_{BW} is set to $1.5\,\mathrm{GeV}^{-1}$ in line with the previous BELLE measurement [19].

Table 2.1: Blatt-Weisskopf barrier form factors with $z = q\, r_{BW}$ and $z_0 = q_0\, r_{BW}$. [29]

L	$F_L(q)$	$B_L(q, q_0)$
0	1	1
1	$\sqrt{\dfrac{2\,z^2}{1+z^2}}$	$\sqrt{\dfrac{1+z_0^2}{1+z^2}}$
2	$\sqrt{\dfrac{13\,z^4}{9+3\,z^2+z^4}}$	$\sqrt{\dfrac{9+3\,z_0^2+z_0^4}{9+3\,z^2+z^4}}$

2.1.2 Relativistic Breit-Wigner distribution

The relativistic Breit-Wigner distribution describes the line shape of a resonance decaying into two particles with relative angular momentum L [30]:

$$\mathcal{T}(m) = \frac{1}{m_0^2 - m^2 - i\,m_0\,\Gamma(m)}. \tag{2.6}$$

Here, m and m_0 denote the invariant mass and nominal mass of the resonance, respectively, and the mass dependent width is parameterized as

$$\Gamma(m) = \Gamma_0\,\frac{m_0}{m}\left(\frac{q}{q_0}\right)^{2L+1} B_L(q, q_0)^2\,, \tag{2.7}$$

where Γ_0 is the nominal decay width, q_0 is the value of the breakup momentum at the resonance pole $m = m_0$, and the normalized Blatt-Weisskopf centrifugal barrier factors are given by

$$B_L(q, q_0) = \frac{F_L(q)}{F_L(q_0)}\left(\frac{q_0}{q}\right)^L. \tag{2.8}$$

The Breit-Wigner distribution is the default line shape parameterization in this analysis used for all resonances unless otherwise stated.

2.1.3 Flatté distribution

The proximity to the threshold of an additional decay channel significantly distorts the resonance line shape from the Breit-Wigner distribution. This scenario occurs in $f_0(980) \to \pi^+\pi^-$ decays since the $f_0(980)$ resonance is near the KK threshold ($m_{f_0(980)} = 990\,\mathrm{MeV} \approx 2 \cdot m_K$ [31]). In this case, the Flatté distribution provides a better description, where the mass dependent width in Eq. 2.6 is replaced by the sum of the partial widths into the $\pi\pi$ and KK channels [32]:

$$\Gamma(m) = \Gamma_{\pi\pi}(m) + \Gamma_{KK}(m) \tag{2.9}$$

The partial widths are given by

$$\Gamma_{\pi\pi}(m) = g_\pi\left(\frac{1}{3}\sqrt{1 - 4\,m_{\pi^0}^2/m^2} + \frac{2}{3}\sqrt{1 - 4\,m_{\pi^\pm}^2/m^2}\right) \tag{2.10}$$

$$\Gamma_{KK}(m) = g_K\left(\frac{1}{2}\sqrt{1 - 4\,m_{K^0}^2/m^2} + \frac{1}{2}\sqrt{1 - 4\,m_{K^\pm}^2/m^2}\right), \tag{2.11}$$

where the coupling constants g_π and g_K for $f_0(980)$ resonances are fixed to the values measured by the BES experiment [33]:

$$g_\pi = 0.165 \pm 0.010 \,(\text{stat}) \pm 0.015 \,(\text{syst}) \,\text{GeV} \tag{2.12}$$

$$g_K = (4.21 \pm 0.25 \,(\text{stat}) \pm 0.21 \,(\text{syst})) \cdot g_\pi \,. \tag{2.13}$$

Figure 2.2 (left) compares the Breit-Wigner distribution with the Flatté distribution for the decay $f_0(980) \to \pi^+\pi^-$. The latter abruptly decreases above the KK threshold.

2.1.4 Gournaris-Sakurai distribution

The Gournaris-Sakurai distribution describes the "P-wave" ($L = 1$) decay of a broad resonance into two pions [34]. In that case, the Breit-Wigner propagator is modified to

$$\mathcal{T}(m) = \frac{1 + f(0)/m_0^2}{m_0^2 + f(m) - m^2 - i\,m_0\,\Gamma(m)}\,, \tag{2.14}$$

where $\Gamma(m)$ takes on the same form as in Eq. 2.7 and the function $f(m)$ is defined as

$$f(m) = \Gamma_0 \frac{m_0^2}{q_0^3} \left[q^2 \left(h(m) - h(m_0)\right) + \left(m^2 - m_0^2\right) q_0^2 \left.\frac{dh}{dm}\right|_{m_0} \right] \tag{2.15}$$

$$h(m) = \frac{2}{\pi} \frac{q}{m} \ln \left(\frac{m + 2\,q}{2\,m_\pi} \right)\,. \tag{2.16}$$

The Gournaris-Sakurai line shape is used for $\rho(770) \to \pi^+\pi^-$ decays. For this case, a comparison to the Breit-Wigner distribution is shown in Fig. 2.2 (right).
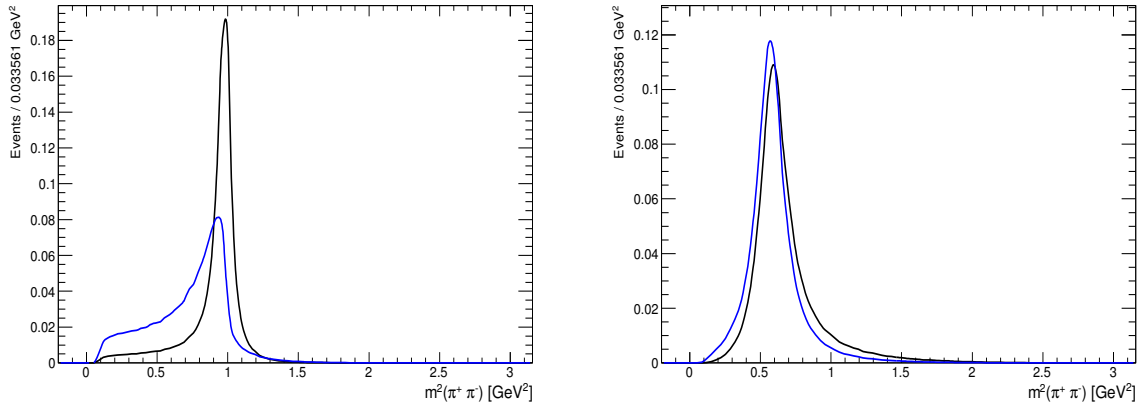
Figure 2.2: Invariant mass distribution of the $\pi^+\pi^-$ system. The left Figure shows $B^+ \to J/\psi\,K^+\,f_0(980)$ decays with $f_0(980) \to \pi^+\pi^-$ using the Breit-Wigner (black) or the Flatté (blue) line shape. The right Figure shows $B^+ \to J/\psi\,K^+\,\rho(770)$ decays with $\rho(770) \to \pi^+\pi^-$ using the Breit-Wigner (black) or the Gournaris-Sakurai (blue) line shape.

2.2 Spin factors

In this section, the spin factors for $B^+ \to J/\psi K^+ \pi^+ \pi^-$ decays are constructed in a covariant tensor formalism. The spin factors are phenomenological descriptions of decay processes and are required to be Lorentz invariant, compatible with angular momentum conservation and, where appropriate, parity conservation. First, the spin projection and angular momentum tensors are introduced which connect the only final state observables represented by the particle's four momenta to the spin dynamics of the reaction. After laying out the formalism, a general rule to construct the spin factors is derived based on an example decay chain.

2.2.1 Spin projection operator and orbital angular momentum tensor

Spin projection operators
A massive spin-1 particle with momentum p, mass M and spin projection $m = 0, \pm 1$ is represented in momentum space by the polarization vector $\varepsilon^\mu(p, m)$. The four components of $\varepsilon^\mu(p, m)$ are not independent, but reduced to three physical degrees of freedom, *i.e.* one longitudinal and two transverse polarizations, by the constraint [1]:

$$p_\mu \, \varepsilon^\mu(p, m) = 0 \,. \tag{2.17}$$

Equation 2.17 implies that the time component of $\varepsilon^\mu(p, m)$ must vanish in the particle's rest frame. The spatial components are then defined according to the spin component along the z-axis as

$$\varepsilon^\mu(m = \pm 1) = \mp \frac{1}{\sqrt{2}} \, (0, 1, \pm i, 0) \tag{2.18}$$

$$\varepsilon^\mu(m = 0) = (0, 0, 0, 1) \,. \tag{2.19}$$

Equations 2.18 and 2.19 are only valid in the rest frame of the particle. To obtain the polarization vectors in an arbitrary frame, a Lorentz transformation from the rest frame to the desired frame is performed resulting in the general expression [35]:

$$\varepsilon^\mu(p, m = \mp 1) = \frac{\pm 1}{M \sqrt{2}} \begin{pmatrix} p_x \mp i \, p_y \\ M + p_x(p_x \pm i \, p_y)/(E + M) \\ \mp i \, M + p_y(p_x \pm i \, p_y)/(E + M) \\ p_z(p_x \pm i \, p_y)/(E + M) \end{pmatrix} \tag{2.20}$$

$$\varepsilon^\mu(p, m = 0) = \frac{1}{M} \begin{pmatrix} p_z \\ p_z \, p_x/(E + M) \\ p_z \, p_y/(E + M) \\ M + p_z^2/(E + M) \end{pmatrix} \,. \tag{2.21}$$

The spin-1 projection operator, which is the fundamental object of the tensor formalism of decay amplitudes, is defined as [25]:

$$P_{(1)}^{\mu\nu}(p) = \sum_m \varepsilon^\mu(p, m) \, \varepsilon^{*\nu}(p, m) = - g^{\mu\nu} + \frac{p^\mu \, p^\nu}{M^2} \,, \tag{2.22}$$

where $g^{\mu\nu} = \text{diag}(+1, -1, -1, -, 1)$ is the Minkowski metric, and $P_{(1)}^{\mu\nu}(p)$ satisfies the relation[9]

$$P_{(1)\lambda}^{\mu}(p)\, P_{(1)}^{\lambda\nu}(p) = -P_{(1)}^{\mu\nu}(p)\,. \tag{2.23}$$

The spin-1 tensor projects any arbitrary four-vector a^{μ} into the spin-1 subspace spanned by the three polarization vectors $\varepsilon^{\mu}(p, m)$, in the sense that the contraction of $P_{(1)}^{\mu\nu}(p)$ with a^{μ} is orthogonal to p^{μ}, i.e. $a'^{\mu}p_{\mu} = 0$ with $a'^{\mu} = P_{(1)}^{\mu\nu}(p)a_{\nu}$.[10] Therefore, the spin projection operator selects that part of a^{μ} which satisfies Eq. 2.17, the necessary condition of a spin-1 state. The spin-2 polarization tensors are obtained by coupling two spin-1 states to a spin-2 state:

$$\varepsilon^{\mu\nu}(p, m) = \sum_{m_1, m_2} \langle 1\, m_1, 1\, m_2 | 2\, m \rangle\, \varepsilon^{\mu}(p, m_1)\, \varepsilon^{\nu}(p, m_2) \tag{2.24}$$

where $\langle 1\, m_1, 1\, m_2 | 2\, m \rangle$ are the Clebsch-Gordon coefficients. By construction, the spin-2 polarization tensors fulfill the so-called spin-2 Rarita-Schwinger conditions [36]:

$$p^{\mu}\, \varepsilon_{\mu\nu}(p, m) = 0 \tag{2.25}$$

$$\varepsilon_{\mu\nu}(p, m) = \varepsilon_{\nu\mu}(p, m) \tag{2.26}$$

$$g^{\mu\nu}\, \varepsilon_{\mu\nu}(p, m) = 0\,. \tag{2.27}$$

These supplementary conditions reduce the sixteen elements of the rank-2 tensor $\varepsilon^{\mu\nu}(p, m)$ to five independent elements. The spin-2 projection operator is given by

$$
\begin{aligned}
P_{(2)}^{\mu\nu\alpha\beta}(p) &= \sum_{m} \varepsilon^{\mu\nu}(p, m)\, \varepsilon^{*\alpha\beta}(p, m) \\
&= \frac{1}{2} \left(P_{(1)}^{\mu\alpha}(p)\, P_{(1)}^{\nu\beta}(p) + P_{(1)}^{\mu\beta}(p)\, P_{(1)}^{\nu\alpha}(p) \right) - \frac{1}{3} P_{(1)}^{\mu\nu}(p)\, P_{(1)}^{\alpha\beta}(p)
\end{aligned} \tag{2.28}
$$

which projects any second-rank tensor into the spin-2 subspace, i.e. it selects that part of the rank-2 tensor which satisfies the spin-2 Rarita-Schwinger conditions. This concept is generalized to arbitrary integer spins in Refs. [25, 27].

Orbital angular momentum tensors

The states of pure angular momentum L for a two particle system are constructed from their momenta p_1 and p_2. First, define the total momentum $p_{12} = p_1 + p_2$ and the relative momentum $q_{12} = p_1 - p_2$. The angular momentum tensor is obtained by projecting the rank-L tensor $q_R^{\nu_1}\, q_R^{\nu_2} \ldots q_R^{\nu_l}$ constructed from the relative momenta to the spin-L subspace:

$$L_{(L)\mu_1\mu_2\ldots\mu_L}(p_R, q_R) = (-1)^L\, P_{(L)\mu_1\mu_2\ldots\mu_L\nu_1\nu_2\ldots\nu_L}(p_R)\, q_R^{\nu_1}\, q_R^{\nu_2} \ldots q_R^{\nu_L} \tag{2.29}$$

where the spin projection operator ensures that the *a priori* 4^L elements of the rank-L tensor reduce to $2L + 1$ independent elements in accordance with the number of degrees of

---

[9]Equation 2.23 only holds, strictly speaking, if the particle is "on-shell", i.e. $p^2 = M^2$. Although intermediate resonances are not necessarily "on-shell", it is assumed that p^2 is reasonably close to the nominal mass such that Eq. 2.23 holds approximately.

[10]Note that Eq. 2.22 allows a small longitudinal component if the particle is "off-shell". Therefore, an "off-shell" particle is not in a pure spin state.

freedom of a state with angular momentum L [25,27]. The $L = 0, 1, 2$ tensors are explicitly given by

$$L_{(0)}(p_R, q_R) = 1 \tag{2.30}$$
$$L_{(1)}^{\mu}(p_R, q_R) = -P_{(1)\mu\nu}(p_R)\, q_R^{\nu} \tag{2.31}$$
$$L_{(2)}^{\mu\nu}(p_R, q_R) = L_{(1)}^{\mu}(p_R, q_R)\, L_{(1)}^{\nu}(p_R, q_R) + \frac{1}{3} L_{(1)}(p_R, q_R)^2\, P_{(1)}^{\mu\nu}(p_R)\,. \tag{2.32}$$

For the sake of brevity, the following shortcut notation is introduced for a decay process $R \to 1\,2$:

$$p_R \equiv p_{12} \tag{2.33}$$
$$q_R \equiv q_{12} \tag{2.34}$$
$$\varepsilon^{\mu}(R) \equiv \varepsilon^{\mu}(p_R, m_R) \tag{2.35}$$
$$P_{(1)}^{\mu\nu}(R) \equiv P_{(1)}^{\mu\nu}(p_R) \tag{2.36}$$
$$L_{(1)}^{\mu}(R) \equiv L_{(1)}^{\mu}(p_R, q_R) \tag{2.37}$$

and the same applies to spin-2 objects.

2.2.2 Conservation laws

The amplitude for a decay process $R \to A\,B$ is given in terms of the relative angular momentum between the daughter particles $\vec{L}_{AB}$ and total intrinsic spin $\vec{S}_{AB}$. The latter is given by the addition of the individual particle spins

$$\vec{S}_{AB} = \vec{S}_A + \vec{S}_B \tag{2.38}$$

so that the quantum number S_{AB} can take on the following range of values in integer steps:

$$|S_A - S_B| \leq S_{AB} \leq S_A + S_B \,. \tag{2.39}$$

Since the total angular momentum is conserved, the possible spin-orbit couplings (L_{AB}, S_{AB}) are restricted to those, which satisfy

$$\vec{J}_R = \vec{L}_{AB} + \vec{S}_{AB} \tag{2.40}$$

where the spin of the resonance R is denoted as J_R. Furthermore, electromagnetic and strong interactions conserve parity which imposes the condition

$$\eta_R = \eta_A\,\eta_B\,(-1)^{L_{AB}} \,, \tag{2.41}$$

where η_R, η_A and η_B are the intrinsic parities of the particles R, A, and B, respectively. If parity is conserved in the decay, Eq. 2.41 restricts L_{AB} to be either even or odd.

The parity transformation, defined as the mirroring of the physical system, acts on the spatial coordinates $\vec{x}$, energy E, and momentum $\vec{p}$ of a particle as

$$\mathbf{P}: \ \vec{x} \to -\vec{x}, \qquad E \to E, \qquad \vec{p} \to -\vec{p} \tag{2.42}$$

or equivalently in covariant notation:

$$\mathbf{P}: \ p^\mu \to \mathbf{P}^\mu_{\ \nu}\, p^\nu \tag{2.43}$$

where $\mathbf{P}^\mu_{\ \nu} = \mathrm{diag}(+1, -1, -1, -, 1)$ denotes the space-inversion operator. The polarization vector of a spin-1 particle with intrinsic parity η transforms under space-inversion as

$$\mathbf{P}: \ \varepsilon^\mu(\vec{p}, m) \to \eta\,\varepsilon^\mu(-\vec{p}, m) = -\eta\,\mathbf{P}^\mu_{\ \nu}\,\varepsilon^\nu(\vec{p}, m) \tag{2.44}$$

which in turn implies, in combination with Eq. 2.22, the transformation properties of the spin-projection and angular momentum tensors

$$\mathbf{P}: \ P^{\mu\nu}_{(1)}(p) \to \mathbf{P}^\mu_{\ \alpha}\,\mathbf{P}^\nu_{\ \beta}\,P^{\alpha\beta}_{(1)}(p) \tag{2.45}$$

$$\mathbf{P}: \ L^\mu_{(1)}(p, q) \to \mathbf{P}^\mu_{\ \nu}\,L^\nu_{(1)}(p, q) \,. \tag{2.46}$$

2.2.3 Decay amplitudes in tensor formalism

The construction of the spin factors proceeds in two steps: first, the two-body amplitudes for each node of the decay tree are calculated by appropriately combining polarization, spin and angular momentum tensors derived in the previous subsections into Lorentz scalars. For a decay process $R \to A\,B$, the two-body amplitude is denoted as $\langle A\,B, L_{AB}, S_{AB}|\mathcal{M}|R\rangle$ and the particles are henceforth labelled according to their meson type, *cf.* Table 1.1. In particular, the final state particles are labelled as $V_0 = J/\psi$ and P_i $(i = 1, 2, 3)$ for the pseudoscalar final states (K^+, π^+, π^-) in the order of their appearance in the decay tree starting at the mother particle. Thereafter, the two-body amplitudes are chained together and a sum over all (unobservable) spin states is applied. This procedure is elucidated on the basis of the example decay $B^+ \to J/\psi \left[K_1^+(1270) \to \pi^+ (K^*(892) \to K^+\pi^-)\right]$. In that case, the label P_i refers to $P_i = (\pi^+, K^+, \pi^-)$.

a) $B^+ \to J/\psi\ K_1^+(1270)$

The first step in the decay chain is the transition from the B^+ meson to a vector and an axialvector meson, $B^+ \to V_0\,A$. There are three different spin couplings $S_{AV_0} = 0, 1, 2$, *cf.* Eq. 2.39, giving rise to three spin-orbit configurations $(L_{AV_0} = S_{AV_0})$ consistent with angular momentum conservation, *i.e.* condition 2.40. Since parity is not conserved in weak interactions, even and odd values for the orbital angular momentum are allowed. The $L_{AV_0} = 0$ ("S-wave") amplitude is obtained by assigning a polarization vector to each spin-1 particle and contract them:

$$\langle A\,V_0, L = 0, S = 0|\mathcal{M}|B\rangle = \varepsilon_\alpha^*(V_0)\,\varepsilon^{*\alpha}(A) \tag{2.47}$$

where the complex conjugation of the polarization vector signifies the production rather than the decay of the particle.

The first ingredient to construct the $L_{AV_0} = 1$ ("P-wave") amplitude is the angular momentum tensor $L_{(1)}^\mu(B)$ which is then contracted with a spin-1 wave function $\Phi_{(1)}^\mu$:

$$\langle A\,V_0, L = 1, S = 1|\mathcal{M}|B\rangle = L_{(1)\mu}(B)\,\Phi_{(1)}^\mu\,. \tag{2.48}$$

The latter is obtained by coupling two spin-1 states to a state of pure spin-1. This is accomplished by projecting the polarization vectors $\varepsilon^{*\mu}(V_0)$ and $\varepsilon^{*\mu}(A)$ into the spin-1 subspace transverse to the momentum of the decaying particle. However, there is no way to contract $P_{(1)}^{\mu\nu}(B)$, $\varepsilon^{*\mu}(V_0)$ and $\varepsilon^{*\mu}(A)$ into a rank-1 tensor (vector) as required for a spin-1 state. Therefore, a combination with the rank-3 tensor $\varepsilon_{\alpha\beta\gamma\delta}\,p_B^\delta$ is needed [23, 26]:

$$\Phi_{(1)}^\mu = P_{(1)}^{\mu\alpha}(B)\,\varepsilon_{\alpha\beta\gamma\delta}\,\varepsilon^{*\beta}(V_0)\,\varepsilon^{*\gamma}(A)\,p_B^\delta\,, \tag{2.49}$$

whereby $\varepsilon_{\alpha\beta\gamma\delta}$ is the total antisymmetric Levi-Civita tensor. In fact, this ensures the correct parity transformation behavior of the amplitude.[11] For this purpose, consider how

---

[11]Although parity is not conserved in the weak decay, a state of definite angular momentum and well defined parity is produced. Therefore, the amplitude should reflect the parity of this state which is conserved in the subsequent strong decays.

the explicit expression of the amplitude given by

$$\langle A\,V_0, L=1, S=1|\mathcal{M}|B\rangle = L_{(1)\varepsilon}(B)\,P_{(1)}^{\epsilon\alpha}(B)\,\varepsilon_{\alpha\beta\gamma\delta}\,\varepsilon^{*\beta}(V_0)\,\varepsilon^{*\gamma}(A)\,p_B^{\delta} \tag{2.50}$$

$$= \varepsilon_{\alpha\beta\gamma\delta}\,L_{(1)}^{\alpha}(B)\,\varepsilon^{*\beta}(V_0)\,\varepsilon^{*\gamma}(A)\,p_B^{\delta}\,, \tag{2.51}$$

where the relation $L_{(1)\varepsilon}(B)\,P_{(1)}^{\epsilon\alpha}(B)=L_{(1)}^{\alpha}(B)$ is used in the second step, transforms under space inversion:

$$\mathbf{P}:\ \langle A\,V_0, 1, 1|\mathcal{M}|B\rangle \to (\eta_A\,\eta_{V_0})\varepsilon_{\alpha\beta\gamma\delta}\,\mathbf{P}^{\alpha}_{\kappa}\,\mathbf{P}^{\beta}_{\lambda}\,\mathbf{P}^{\gamma}_{\mu}\,\mathbf{P}^{\delta}_{\nu}\,L_{(1)}^{\kappa}(B)\,\varepsilon^{*\lambda}(V_0)\,\varepsilon^{*\mu}(A)\,p_B^{\nu} \tag{2.52}$$

$$\to -(\eta_A\,\eta_{V_0})\,\langle A\,V_0, 1, 1|\mathcal{M}|B\rangle \tag{2.53}$$

$$\to \langle A\,V_0, 1, 1|\mathcal{M}|B\rangle\,. \tag{2.54}$$

In the first step, the transformation properties given in Eq. 2.43 up to Eq. 2.46 are inserted while the second step follows directly from the definition of the space inversion operator, *cf.* Sec. 2.2.2, and the antisymmetry of $\varepsilon_{\alpha\beta\gamma\delta}$. In the last step, the intrinsic parities $\eta_A=1$ and $\eta_{V_0}=-1$ are inserted to conclude that the amplitude is parity even as expected for a P-wave coupling of a vector and an axialvector meson ($\eta_A\,\eta_{V_0}\,(-1)^{L_{AV_0}}=1$). In contrast, the $L_{AV_0}=0$ amplitude is parity odd:

$$\mathbf{P}:\ \langle A\,V_0, 0, 0|\mathcal{M}|B\rangle \to (\eta_A\,\eta_{V_0})\,\mathbf{P}^{\mu}_{\alpha}\,\mathbf{P}^{\beta}_{\mu}\,\varepsilon^{*\alpha}(V_0)\,\varepsilon^{*}_{\beta}(A) \tag{2.55}$$

$$\to (\eta_A\,\eta_{V_0})\,\varepsilon^{*\alpha}(V_0)\,\varepsilon^{*}_{\alpha}(A) \tag{2.56}$$

$$\to -\langle A\,V_0, 0, 0|\mathcal{M}|B\rangle\,, \tag{2.57}$$

where the relation $\mathbf{P}^{\mu}_{\alpha}\,\mathbf{P}^{\beta}_{\mu}=\delta^{\beta}_{\alpha}$ is used, in accordance with a S-wave coupling ($\eta_A\,\eta_{V_0}\,(-1)^{L_{AV_0}}=-1$).

Similarly, the $L_{AV_0}=2$ ("D-wave") amplitude is built out of the angular momentum tensor $L_{(2)}^{\mu\nu}(B)$ and the spin-2 wave function $\Phi_{(2)}^{\mu\nu}=P_{(2)}^{\mu\nu\alpha\beta}(B)\,\varepsilon^{*}_{\beta}(V_0)\,\varepsilon^{*}_{\gamma}(A)$ what yields:

$$\langle A\,V_0, L=2, S=2|\mathcal{M}|B\rangle = L_{(2)\alpha\beta}(B)\,\varepsilon^{*\alpha}(V_0)\,\varepsilon^{*\beta}(A) \tag{2.58}$$

where the spin-2 projection operator $P_{(2)}^{\mu\nu\alpha\beta}(B)$ is redundant since $L_{(2)\alpha\beta}(B)$ is already orthogonal to p_B, *i.e.* $L_{(2)\alpha\beta}(B)P_{(2)}^{\mu\nu\alpha\beta}(B)=L_{(2)}^{\mu\nu}(B)$.

b) $K_1^+(1270) \to \pi^+ K^*(892)$

At the second node of the decay tree, the previously produced axial vector meson decays into a vector and a pseudoscalar particle. This is a strong decay such that Eq. 2.41 restricts the angular momentum to even values. Furthermore, the total spin is given by the intrinsic spin of the vector meson leading to two distinct amplitudes. In both cases the spin-1 wave function is given by $\Phi_{(1)}^{\mu}=P_{(1)}^{\mu\nu}(A)\,\varepsilon^{*}_{\nu}(V)$ resulting in the S and D-wave amplitudes:

$$\langle V\,P_1, L=0, S=1|\mathcal{M}|A\rangle = \varepsilon_{\mu}(A)\,P_{(1)}^{\mu\nu}(A)\,\varepsilon^{*}_{\nu}(V) \tag{2.59}$$

$$\langle V\,P_1, L=2, S=1|\mathcal{M}|A\rangle = \varepsilon_{\mu}(A)\,L_{(2)}^{\mu\lambda}(A)\,P_{(1)\lambda\nu}(A)\,\varepsilon^{*\nu}(V) \tag{2.60}$$

$$= \varepsilon_{\mu}(A)\,L_{(2)}^{\mu\nu}(A)\,\varepsilon^{*}_{\nu}(V)\,. \tag{2.61}$$

23

c) $K^*(892) \to K^+\pi^-$

The pseudoscalars in the decay $V \to P_2 P_3$ have to be in a relative P-wave. Hence there is only one amplitude:

$$\langle P_2 P_3, L=1, S=0|\mathcal{M}|V\rangle = \varepsilon_\rho(V)\, L^\rho_{(1)}(V)\,. \tag{2.62}$$

d) $B^+ \to J/\psi \left[K_1^+(1270) \to \pi^+ \left(K^*(892) \to K^+\pi^-\right)\right]$

Finally, the previously calculated two-body amplitudes are combined into the total spin factor. There are three possible spin-orbit couplings at the first node of the decay tree, followed by two couplings at the second node and only one at the last node amounting to six distinct spin factors. To start with, the lowest possible angular momentum is chosen at each node equivalent to the decay chain $B^+[S] \to J/\psi \left[K_1^+(1270)[S] \to \pi^+ (K^*(892)[P] \to K^+\pi^-)\right]$.[12] In that case, the spin factor is calculated as

$$S_f = \sum_{m_A, m_V, m_{V0}} \langle P_2 P_1, 1, 0|\mathcal{M}|V\rangle \langle V P_1, 0, 1|\mathcal{M}|A\rangle \langle A V_0, 0, 0|\mathcal{M}|B\rangle \tag{2.63}$$

$$= \sum_{m_A, m_V, m_{V0}} \varepsilon^{*\alpha}(V_0) \left[\varepsilon^*_\alpha(A)\,\varepsilon_\mu(A)\right] P^{\mu\nu}_{(1)}(A) \left[\varepsilon^*_\nu(V)\varepsilon_\rho(V)\right] L^\rho_{(1)}(V) \tag{2.64}$$

$$= \sum_{m_{V0}} \varepsilon^{*\alpha}(V_0) \left[P_{(1)\alpha\mu}(A)\right] P^{\mu\nu}_{(1)}(A) \left[P_{(1)\nu\rho}(V)\right] L^\rho_{(1)}(V) \tag{2.65}$$

$$= \sum_{m_{V0}} \varepsilon^*_\alpha(V_0)\, P^{\alpha\beta}_{(1)}(A)\, L_{(1)\beta}(V)\,. \tag{2.66}$$

Thereby, Equation (2.63) gives the definition of the spin factor in which the two-body amplitudes are subsequently included. The third equality follows from the relation $P^{\mu\nu}_{(1)}(p) = \sum_m \varepsilon^\mu(p, m)\,\varepsilon^{*\nu}(p, m)$ which allows to evaluate the sum over the spin projections m_A and m_V. In the last step, redundant spin projection operators are contracted. Although the J/ψ meson is considered as final state particle, a coherent sum over its spin projections m_{V_0} is applied since the decoherence time is much longer than the J/ψ lifetime ($\mathcal{O}(10^{-21}\,\text{s})$ [31]). Therefore, different J/ψ polarization states interfere.

The spin factors for the other decay chains, obtained in the same way, are given in Table 2.2, except for the decay chains

$$B^+[P, D] \to J/\psi \left[K_1^+(1270)[D] \to \pi^+ \left(K^*(892) \to K^+\pi^-\right)\right]$$

which are not considered in this analysis since they are expected to be strongly suppressed.

Note that the spin factors of e.g. $B \to J/\psi \left[K_1^+(1270) \to K^+ \left(\rho(770) \to \pi^+\pi^-\right)\right]$ may be obtained by a simple permutation of $P_i = (\pi^+, K^+, \pi^-)$ to $P_i = (K^+, \pi^+, \pi^-)$.

---

[12] The relative angular momentum between the two daughter particles is labeled in square brackets as S, P, D for $L = 0, 1, 2$.

Table 2.2: Spin factors for various decay chains contributing to $B \to V_0 \, P_1 \, P_2 \, P_3$ decays. Letters in square brackets refer to the relative orbital angular momentum of the decay products. If no angular momentum is specified, the lowest angular momentum state consistent with angular momentum conservation and, where appropriate, parity conservation is used. The sum over the V_0 polarization states is implicit.

	Decay chain	Spin factor
1	$B \to (AV_0),\ A \to (VP_1),\ V \to (P_2P_3)$	$\varepsilon^*_\alpha(V_0)\, P^{\alpha\beta}_{(1)}(A)\, L_{(1)\beta}(V)$
2	$B \to (AV_0),\ A[D] \to (VP_1),\ V \to (P_2P_3)$	$\varepsilon^*_\alpha(V_0)\, L^{\alpha\beta}_{(2)}(A)\, L_{(1)\beta}(V)$
3	$B[P] \to (AV_0),\ A \to (VP_1),\ V \to (P_2P_3)$	$\varepsilon_{\alpha\beta\gamma\delta}\, \varepsilon^{*\alpha}(V_0)\, L^\beta_{(1)}(B)\, p^\gamma_B\, P^{\delta\mu}_{(1)}(A) L_{(1)\mu}(V)$
4	$B[D] \to (AV_0),\ A \to (VP_1),\ V \to (P_2P_3)$	$\varepsilon^*_\alpha(V_0)\, L^{\alpha\beta}_{(2)}(B)\, P_{(1)\beta\mu}(A)\, L^\mu_{(1)}(V)$
5	$B \to (AV_0),\ A \to (SP_1),\ S \to (P_2P_3)$	$\varepsilon^{*\alpha}(V_0)\, L_{(1)\alpha}(A)$
6	$B \to (V_1V_0),\ V_1 \to (V_2P_1),\ V_2 \to (P_2P_3)$	$\varepsilon^*_\alpha(V_0)\, P^{\alpha\kappa}_{(1)}(V_1)\, \varepsilon_{\kappa\lambda\mu\nu}\, L^\lambda_{(1)}(V_1)\, p^\mu_{V_1}\, P^{\nu\xi}_{(1)}(V_1)\, L_{(1)\xi}(V_2)$
7	$B \to (T_-V_0),\ T_- \to (T_+P_1),\ T_+ \to (P_2P_3)$	$L_{(1)\alpha}(B)\, \varepsilon^*_\beta(V_0)\, P^{\alpha\beta\mu\nu}_{(2)}(T_-)\, L_{(2)\mu\nu}(T_+)$
8	$B \to (T_-V_0),\ T_- \to (VP_1),\ V \to (P_2P_3)$	$L_{(1)\alpha}(B)\, \varepsilon^*_\beta(V_0)\, P^{\alpha\beta\lambda\mu}_{(2)}(T_-)\, L_{(1)\lambda}(T_-)\, P_{(1)\mu\nu}(T_-)\, L^\nu_{(1)}(V)$
9	$B \to (T_-V_0),\ T_- \to (SP_1),\ S \to (P_2P_3)$	$L_{(1)\alpha}(B)\, \varepsilon^*_\beta(V_0)\, L^{\alpha\beta}_{(2)}(T_-)$
10	$B \to (T_+V_0),\ T_+ \to (VP_1),\ V \to (P_2P_3)$	$\varepsilon_{\kappa\lambda\mu\nu}\, p^\kappa_{T_+}\, L_{(1)\alpha}(B)\, \varepsilon^*_\beta(V_0)\, P^{\alpha\beta\lambda\xi}_{(2)}\, L^\mu_{(2)\xi}(T_+)\, P^{\nu\rho}_{(1)}(T_+)\, L_{(1)\rho}(V)$
11	$B \to (VP_1),\ V \to (AP_2),\ A \to (V_0P_3)$	$L_{(1)\alpha}(B)\, P^{\alpha\beta}_{(1)}(V)\, P_{(1)\beta\rho}(V)\, \varepsilon^{*\rho}(V_0)$
12	$B \to (VP_1),\ V \to (V_0S),\ S \to (P_2P_3)$	$L_{(1)\alpha}(B)\, P^{\alpha\beta}_{(1)}(V)\, \varepsilon^*_\beta(V_0)$
13	$B \to (AP_1),\ A \to (VV_0),\ V \to (P_2P_3)$	$L_{(1)\alpha}(B)\, P^{\alpha\kappa}_{(1)}(A)\, \varepsilon_{\kappa\lambda\mu\nu}\, p^\lambda_A\, \varepsilon^{*\mu}(V_0)\, L^\nu_{(1)}(V)$
14	$B \to (AV),\ A \to (P_1V_0),\ V \to (P_2P_3)$	$L_{(1)\alpha}(V)\, P^{\alpha\beta}_{(1)}(A)\, \varepsilon^*_\beta(V_0)$
15	$B \to (PV),\ P \to (P_1V_0),\ V \to (P_2P_3)$	$L_{(1)\alpha}(B)\, L^\alpha_{(1)}(V)\, L^\mu_{(1)}(P)\, \varepsilon^*_\mu(V_0)$

2.2.4 General recipe to construct spin factors

Based upon the results of the previous subsection, the amplitude for a decay process $R \to AB$ can be written in the general form:

$$\langle AB, L_{AB}, S_{AB} | \mathcal{M} | R \rangle = \varepsilon_{(S_R)}(R) \, X(S_R, L_{AB}, S_{AB}) \, L_{(L_{AB})}(R) \, \Phi_{(S_{AB})} \tag{2.67}$$

$$\Phi_{(S_{AB})} = P_{(S_{AB})}(R) \, X(S_{AB}, S_A, S_B) \, \varepsilon^*_{(S_A)}(A) \, \varepsilon^*_{(S_B)}(B) \,. \tag{2.68}$$

Here, a polarization vector is assigned to the decaying particle and complex conjugated polarization vectors for each decay product. The spin and orbital angular momentum couplings are described by the tensors $P_{(S_{AB})}(R)$ and $L_{(L_{AB})}(R)$, respectively. All tensors are properly contracted to give a scalar. This requires in some cases to include the tensor $\varepsilon_{\alpha\beta\gamma\delta} \, p_R^\delta$:

$$X(j_a, j_b, j_c) = \begin{cases} 1 & \text{, for } j_a + j_b + j_c = even \\ \varepsilon_{\alpha\beta\gamma\delta} \, p_R^\delta & \text{, for } j_a + j_b + j_c = odd \end{cases} . \tag{2.69}$$

To obtain the spin factor for a given decay chain, the two-body processes are combined as described in the previous subsection. The spin factors for the decay chains considered in this analysis are listed in Table 2.2 whereby their explicit calculation is given in Appendix A.

2.2.5 Non resonant amplitudes

Not all contributions to $B^+ \to J/\psi \, K^+ \pi^+ \pi^-$ decays are necessarily associated to intermediate resonances. These so-called non resonant contributions were modeled in the BELLE analysis, *cf.* 1.4.2, as a simple constant over phase space ($\mathcal{A}_{NR}(X) = 1$ [19]). However, a constant amplitude violates angular momentum conservation since the J/ψ meson is a spin-1 particle. Consequently there must be relative angular momentum among the daughter particles.

In the isobar model, it is straightforward to construct non-resonant amplitudes consistent with angular momentum conservation. For example, the amplitude for the decay chain

$$B[S] \to V_0 \, [A[S] \to (P_1 \, V[P] \to (P_2 \, P_3))]$$

can be transformed to the non resonant amplitude for the decay

$$B[S] \to V_0 \, [P_1 \, (P_2 \, P_3)_P]_S \,,$$

where the subscript denotes the angular momentum state, by setting the line shapes to unity leading to the spin factor alone altering the phase space distribution [37]. The state $(P_2 \, P_3)_P$ may then be interpreted as an "effective" or non resonant vector particle with a mass given by its four-momentum squared (and an infinite decay width). Similar, the state $[P_1 \, (P_2 \, P_3)_P)]_S$ represents an effective axial-vector particle.

Each of the 15 spin factors in Table 2.2 gives rise to distinct angular momentum coupling schemes among the daughter particles. Furthermore, there are, in general, three

distinct configurations of the pseudoscalar final states for each spin factor summing up to 45 non resonant amplitudes in total.

The same concept can be applied to construct single resonance amplitudes. As an example, the decay $B^+ \to J/\psi \, K_1(1270)$ where the axialvector meson $K_1(1270)$ decays directly to $K^+\pi^+\pi^-$ can be modeled as:

$$B[S] \to V_0 \, [A[S] \to P_1 \, (P_2 \, P_3)_P] \ ,$$

with the "effective" vector particle $(P_2 \, P_3)_P$.

2.3   Validation of amplitude formalism

The amplitude fit is performed by using the amplitude analysis tool MINT (**M**inuit **Int**erface) previously applied to analyze $D^0 \to K^+K^-\pi^+\pi^-$ decays [37, 38]. MINT was developed by the LHCb group Bristol and then further extended to deal with one spin-1 particle in the final state by the author. In particular, the spin factors in Table 2.2 are newly implemented. Besides performing the actual amplitude fit described in Chapter 8, MINT allows generating "toy" MC events according to a given amplitude model. Since this is the first time that the amplitudes of the general decay type $B \to V_0 \, P_1 \, P_2 \, P_3$ are calculated, it is important to validate them. For this purpose, MC events are generated using MINT according to the amplitude model presented in the previous subsections. Moreover, the same decay chains are simulated using the (independent) MC event generator EVTGEN [39]. The phase space distribution of the simulated events obtained from MINT and EVTGEN are then compared. This is an important crosscheck due to the fact that not only the implementation of EVTGEN is completely independent from MINT but also the amplitudes are calculated in a completely different formalism, the so-called helicity formalism [39–42]. Only the following decay chains are considered:

$$B^+[S] \to J/\psi \, \left[K_1^+(1270) \to (K^*(892) \to K^+\pi^-) \, \pi^+\right]$$
$$B^+[P] \to J/\psi \, \left[K_1^+(1270) \to (K^*(892) \to K^+\pi^-) \, \pi^+\right] \ .$$

since others are not implemented in EVTGEN. The projections of the phase space distribution are compared in Figs. 2.3 and 2.4 for the two decay chains. In both cases, the MINT and EVTGEN distributions are in a very good agreement.

Note that there is, indeed, no way to distinguish the S and P-wave decay based on the three invariant mass combinations $m^2(K^+\pi^+\pi^-), m^2(K^+\pi^-)$ and $m^2(\pi^+\pi^-)$ alone, as can be seen from Fig. 2.3. However, the invariant mass projection $m^2(J/\psi\pi^+\pi^-)$ and in particular the angles χ and $\cos\theta$ contribute a significant discrimination power between the angular momentum states. This is clearly a major improvement of the developed amplitude formalism describing the full seven-dimensional phase space with respect to the three dimensional approach used in the BELLE analysis, *cf.* Sec. 1.4.2.
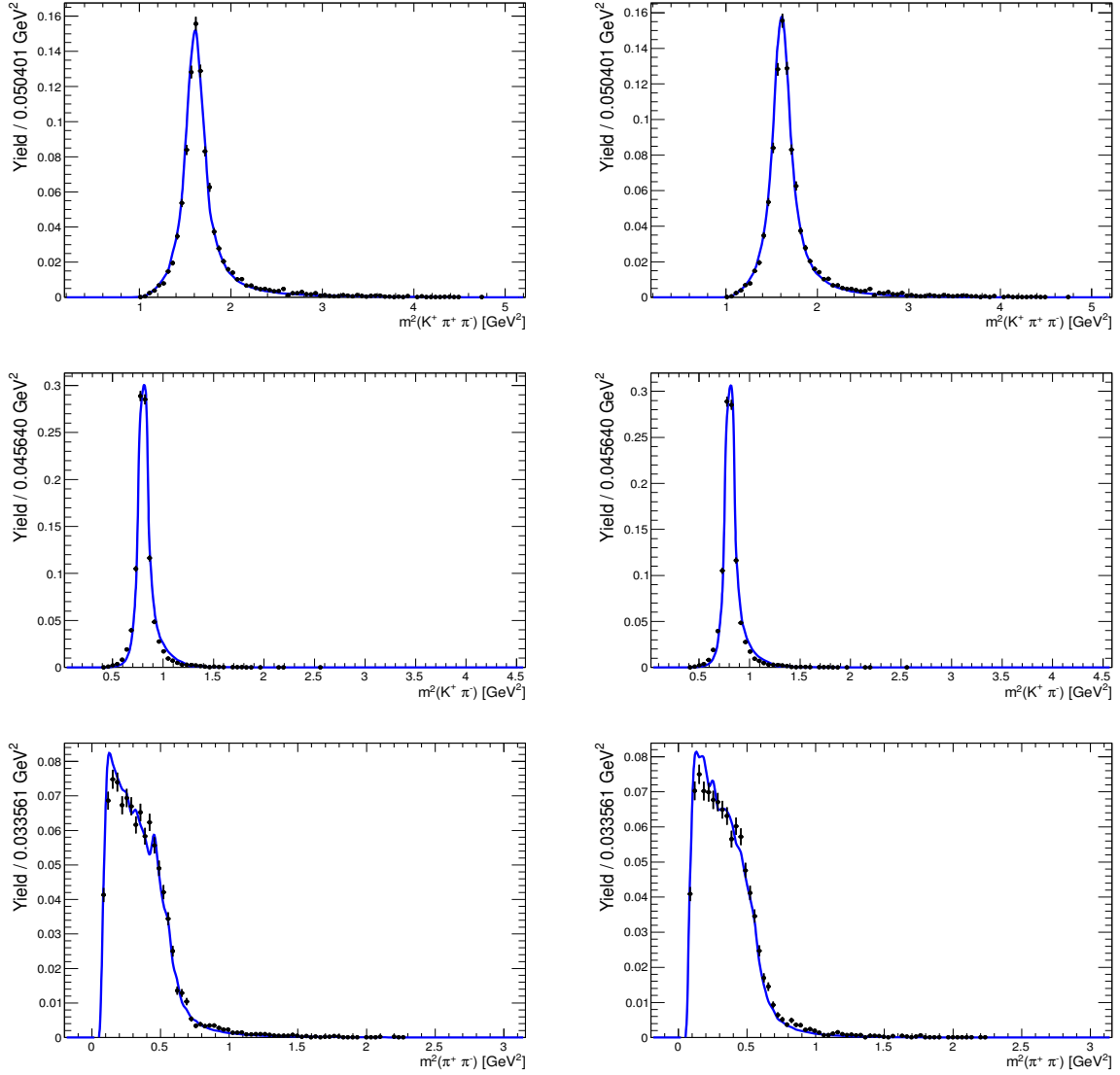
Figure 2.3: Phase space projections of $B^+[S] \to J/\psi \, [K_1^+(1270) \to K^*(892) \, \pi^+]$ (left) and $B^+[P] \to J/\psi \, [K_1^+(1270) \to K^*(892) \, \pi^+]$ (right) decays generated with MINT (blue) and EVTGEN (black).
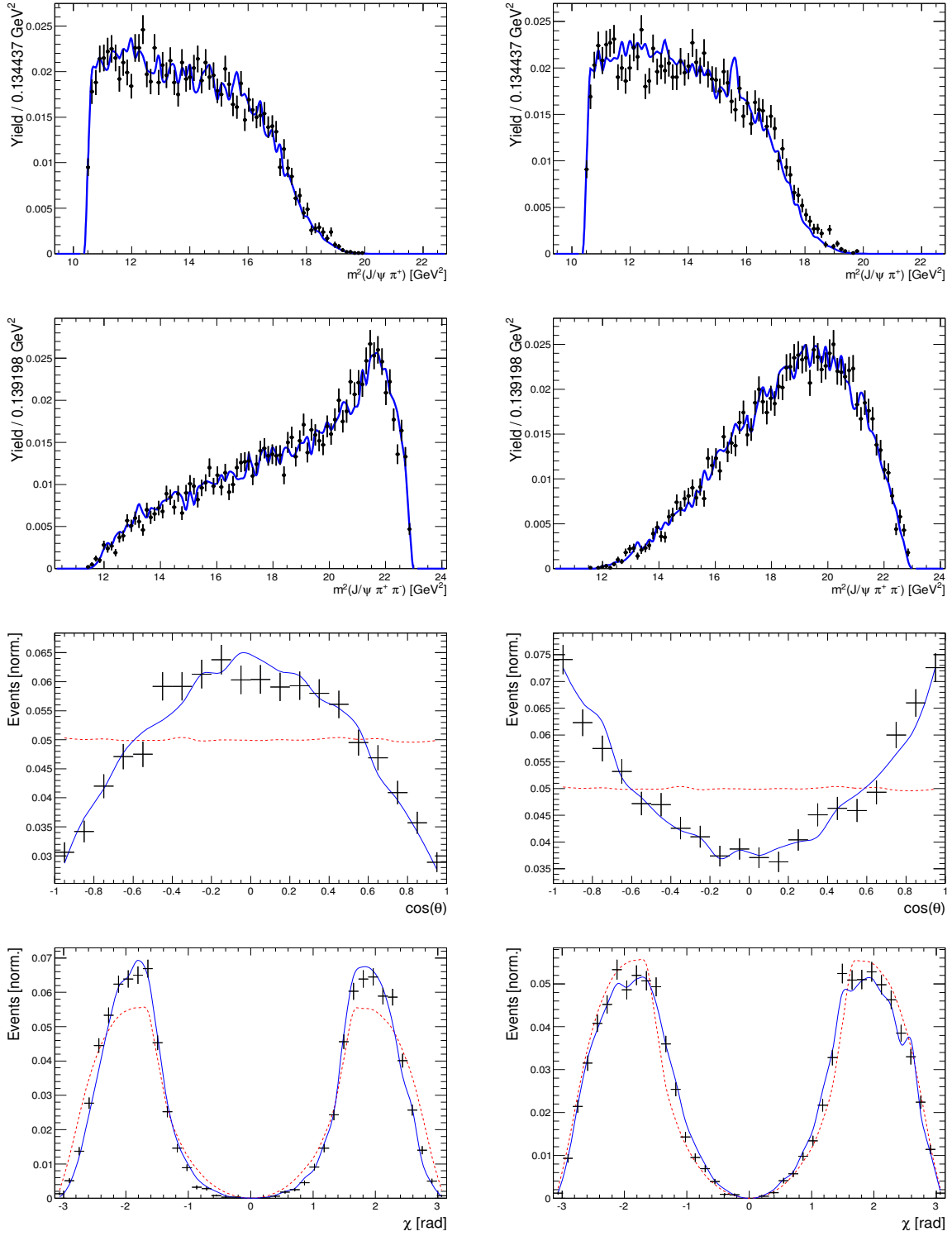
Figure 2.4: Phase space projections of $B^+[S] \to J/\psi \, [K_1^+(1270) \to K^*(892)\,\pi^+]$ (left) and $B^+[P] \to J/\psi \, [K_1^+(1270) \to K^*(892)\,\pi^+]$ (right) decays generated with MINT (blue) and EvtGen (black). The pure phase distribution of the angular observables is shown in red.

3 The LHCb experiment

The LHC [43] is a proton-proton collider with a circumference of 27 km located at the European Organization of Nuclear Research (CERN) close to Geneva. It has been designed to collide two proton beams at a center-of-mass energy of 14 TeV and a frequency of 40 MHz. At nominal configuration each beam consists of 2808 bunches, with $1.1 \cdot 10^{11}$ protons each, leading to a luminosity of $\mathcal{L} = 1 \cdot 10^{34}\,\mathrm{cm}^{-2}\,\mathrm{s}^{-1}$. The general purpose detectors ATLAS and CMS as well as the ALICE detector specialized in studying heavy ion collisions and the LHCb detector are located at the four interaction points of the LHC. A brief description of the LHCb detecor designed for the study of B- and D-meson decays is given in the following chapter.

3.1 The LHCb detector

B-hadrons at the LHC predominantly emerge from $b\bar{b}$ production via gluon-gluon fusion and subsequent hadronization. Since the two gluons carry, in general, very different momentum fractions of the proton, the B-hadrons are boosted along the beam axis. Therefore, approximately 25% of the produced $b\bar{b}$ pairs lie within the acceptance of the
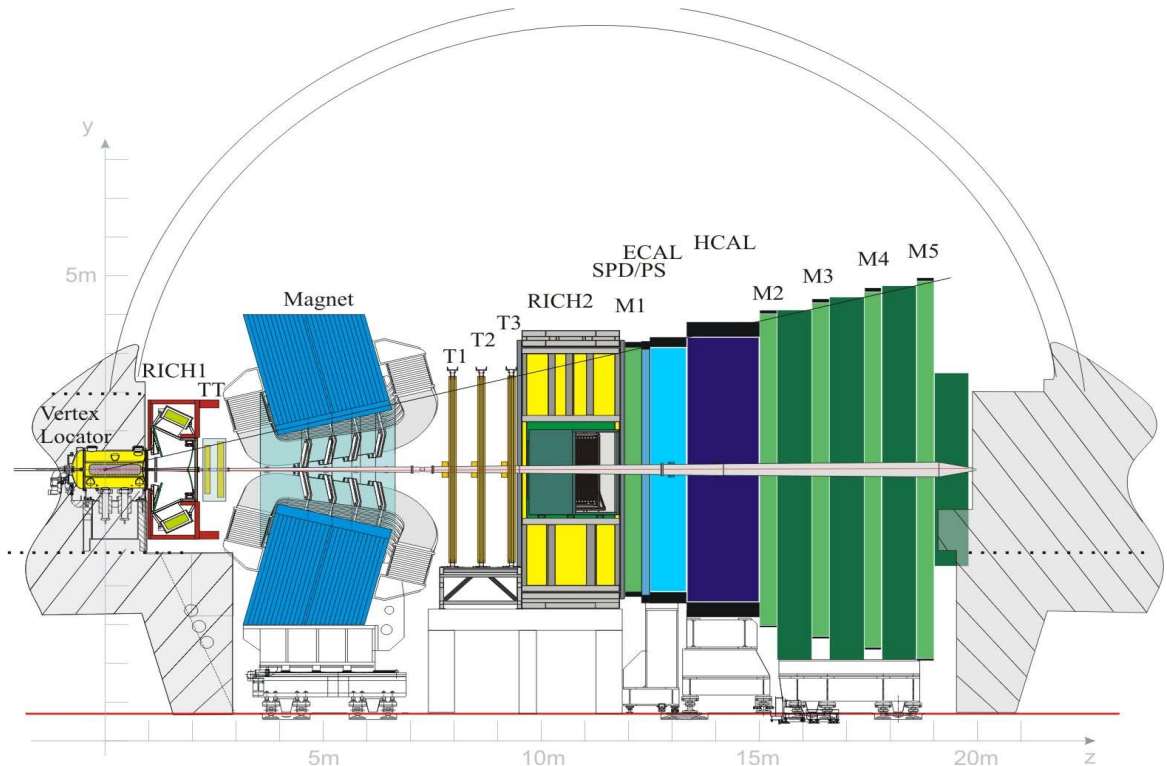
Figure 3.1: Schematic view of the LHCb detector in the y-z plane. Figure taken from Ref. [44].

LHCb detector [45] although it is conceptualized as a single-arm forward spectrometer covering only 4% of the solid angle around the interaction point. Furthermore, the large flight distance (approximately 1 cm on average) of the boosted B-hadrons ensures the excellent time resolution of the LHCb detector. Figure 3.1 shows a schematic view of the LHCb detector. The subdetectors can be categorized according to their main purpose: the **Ve**rtex **Lo**cator (VELO), the **T**rigger **T**racker (TT) and the **t**racking stations (T1-T3) reconstruct the trajectories of charged particles while the two **r**ing-**i**maging **Ch**erenkov detectors (RICH1, RICH2), the **e**lectromagnetic and **h**adronic **cal**orimeters (ECAL and HCAL) as well as the **m**uon chambers (M1-M5) are used to identify the particle species.

3.1.1   Track reconstruction

The reconstruction of the trajectories of charged particles (tracks) allows measuring their charge and momentum. This is accomplished by exploiting the fact that charged particle are bent by magnetic fields. For this purpose, the LHCb dipole magnet provides an integrated magnetic field of 4 Tm which points (predominantly) along the y-axis so that the tracks are bent in the x-z plane. By comparing the track before the magnet reconstructed by the VELO and the TT with the track after the magnet reconstructed by the tracking stations, the momentum of the particle can be inferred. The relative uncertainty of the momentum measurement varies from 0.4% at 5 GeV to 0.6% at 100 GeV.

Vertex Locator
The VELO surrounds the proton-proton interaction region. Its main purpose is to precisely reconstruct the position of the proton-proton interaction, the so-called **p**rimary **v**ertex (PV), and those of possible **s**econdary **v**ertices (SV) originating from the decays of long-lived hadrons. The VELO is composed of 21 modules placed along the beam axis. Each of them is equipped with two different types of half-disc shaped silicon microstrip sensors which measure the distance of a track from the beam axis in polar coordinates. Where the r-sensor, with circular-shaped strips, measures the radial distance, the ϕ-sensor, with strips in radial direction, measures the azimuthal angle.

Trigger Tracker
The TT is located just before the magnet. It consists of four silicon microstrip layers which are tilted relative to each other to allow for a three dimensional track measurement with a single hit resolution of approximately 50 μm. The information provided by the TT enables the reconstruction of both low-momentum particles which are bend out of the spectrometer by the magnetic field and long-lived particles that decay after the passing the VELO.

Tracking stations
The tree tracking stations located behind the magnet complete the tracking system. Each station consists of four layers in a tilted arrangement such as the TT. However, only the so-called **I**nner **T**racker (IT) covering the region close to the beam axis uses silicon

microstrip sensors. The **O**uter **T**racker (OT) is a straw-tube detector providing a spatial resolution of approximately 200 μm and covers the large outer area of the T-stations where the particle flux is lower.

3.1.2 Particle identification

To reconstruct the decays of B-mesons correctly, it is essential to identify the particle type associated to a measured track. The particle identification system of the LHCb detector is composed of two RICH detectors, the calorimeter system and the muon chambers.

RICH detector
The RICH detectors enable to distinguish pions, kaons and protons. This is achieved by using the fact that charged particles emit photons in a cone around their trajectory when transversing a dielectric medium with a velocity that is higher than the speed of of light in that medium, a phenomenon called Cherenkov effect. The opening angle of the light cone is given by

$$\cos\theta_C = \frac{1}{\beta\,n} \tag{3.1}$$

where β is the particle's velocity and n the refractive index of the medium. The RICH detector measures the opening angle so that the particle's velocity can be determined. In combination with the momentum measurement provided by the tracking system, the mass of the particle can be inferred. Two RICH detectors (RICH1, RICH2) with different radiators are implemented in the LHCb detector in order to provide particle identification in a large momentum range ($2\,\mathrm{GeV} < p < 100\,\mathrm{GeV}$).

The calorimeter system
The calorimeter system separates electrons, photons and hadrons and measures their energies. The first component of the calorimeter system is the **S**cintillator **P**ad **D**etector (SPD) which consists of scintillating layers and is used to distinguish between electrons and photons. Only the former release a signal in the SPD. The lead plate installed behind the SPD induces triggered by the incoming particles electromagnetic showers, *i.e.* cascades of photons and electron-positron pairs. The **P**reshower (PS) detector measures the energy deposition in the lead plate in order to discriminate electrons from charged pions. The following electromagnetic and hadronic calorimeters are composed of alternating layers of scintillating pads and absorbers. Where the ECAL uses lead absorbers and measures the energy of electrons and photons, the HCAL uses iron absorbers and measures the energy of hadrons by inducing hadronic showers.

Muon chambers

The muon identification is performed by a system of five muon stations, one of them (M1) is placed in front of the calorimeter system while the others (M2-M4) are placed behind it. The muon stations M2-M5 separated by iron plates are the last part of the detector so that only muons as long-lived and minimum ionising particles can reach them. The muon stations mainly consist of multiwire proportional chambers. Due to the high particle flux, in the inner part of the station M1 a gas electron multiplier detector is used.

3.1.3 Trigger system

It is not possible to record data at the (nominal) bunch crossing rate of 40 MHz. The LHCb trigger system resides with the task to decide, in real-time, whether an event is of interest for the LHCb physics program or can be discarded. It consists of three levels which subsequently reduce the event rate. The first trigger level called **L**evel-**0** (L0) trigger is completely implemented in hardware. It uses information provided by the calorimeters and the muon chambers to filter the events and reduces the rate to approximately 1 MHz. This decision has to be confirmed by the **H**igh **L**evel **T**rigger (HLT) which is implemented in software and runs on a large computing cluster. The HLT is further divided into two levels, HLT1 and HLT2. HLT1 performs a partial event reconstruction and reduces the event rate to approximately 30 kHz which is sufficiently low to allow for a more advanced event reconstruction at HLT2. Finally, the event rate is reduced to 5 kHz with which the data is recorded. More details on the selection criteria required by the trigger levels are provided in Sec. 5.1.

3.2 Data samples

The analysis is based on proton-proton collision data, corresponding to an integrated luminosity of $3\,\mathrm{fb}^{-1}$, collected with the LHCb detector at a center-of-mass energy of $7\,\mathrm{TeV}$ in 2011 and $8\,\mathrm{TeV}$ in 2012.

Besides real data, simulated events are necessary in order to determine the acceptance variation over the Dalitz plane caused by the detector geometry as well as the reconstruction and selection process. For this purpose, eight million $B^+ \to (J/\psi \to \mu^+\mu^-)K^+\pi^+\pi^-$ Monte Carlo (MC) events are generated uniformly in phase space, *i.e.* no intermediate resonances are included. Furthermore, inclusive $B^0 \to J/\psi X$ and $B_s^0 \to J/\psi X$ MC events with $J/\psi \to \mu^+\mu^-$ are used to investigate possible background sources. These samples include the most prominent b-hadron decay channels involving a J/ψ, where the corresponding branching fractions are taken from the PDG [31]. Table 3.1 lists the simulated samples used in this analysis.

The MC event generator Pythia [46] simulates proton-proton collisions including hard scattering processes and hadronization. The hadronization process is repeated until a $B^\pm$ meson is produced, which is then forced to decay into the desired signal channel using the EvtGen [39] generator, in which final-state radiation is simulated using Photos [47]. Electromagnetic and hadronic interactions of the particles with the detector material as well as the consequent detector response are evaluated with the Geant4 [48,49] package. Finally, the reconstruction and selection of the MC events is performed exactly in the same way as for real data. In doing so, wrongly reconstructed events can occur. However, it is possible to reproduce in the simulation if a reconstructed particle is indeed associated with a true signal decay. This procedure, called MC truth-matching enables access to true signal events including the true momenta of the final-state particles, which are, in general, different to the reconstructed momenta due to the limited detector resolution.

Table 3.1: List of simulated MC samples used in the analysis.

MC sample	Generated events	Purpose
$B^+ \to J/\psi K^+\pi^+\pi^-$	8 000 000	Phase space acceptance
$B^0 \to J/\psi X$	2 000 000	Background study
$B_s^0 \to J/\psi X$	2 000 000	Background study

4 Analysis tools

This Chapter introduces important concepts extensively used in this analysis. First, the method of maximum likelihood fitting is discussed in Sec. 4.1 which allows to extract physics parameter from a measured data set. This technique is not only used to determine the signal and background yields, *cf.* Sec. 5.2.3, but also to find the coupling strengths to the multiple intermediate states appearing in $B^+ \to J/\psi\, K^+\pi^+\pi^-$ decays as described in Sec. 8. Another important tool is the the *sPlot* method, presented in Sec. 4.2, which provides access to pure signal distributions by statistically subtracting background.

4.1 Maximum likelihood estimation

The method of maximum likelihood estimates a set of unknown parameters $\vec{\lambda} = \{\lambda_1, \lambda_2, ...\}$ of a theoretical distribution $f(\vec{X}|\vec{\lambda})$ from a set of measured observables $\vec{X} = \{X_1, X_2, ...\}$. From the theoretical prediction of the distribution of the measured data set, the so-called **p**robability **d**ensity **f**unction (PDF) is deduced:

$$\mathcal{P}(\vec{X}|\vec{\lambda}) = \frac{f(\vec{X}|\vec{\lambda})}{\int f(\vec{X'}|\vec{\lambda})\, d\vec{X'}} \,, \tag{4.1}$$

such that $\mathcal{P}(\vec{X}|\vec{\lambda})\, d\vec{X}$ yields the probability to measure the observables within the interval $[\vec{X}, \vec{X} + d\vec{X}]$ assuming a certain parameter set $\vec{\lambda}$. Given N independent measurements $\{\vec{X}_1, \vec{X}_2, ..., \vec{X}_N\}$, the likelihood function is the joint probability density function of all observations considered as a function of $\vec{\lambda}$:

$$\mathcal{L}(\vec{\lambda}) = \prod_{i=1}^{N} \mathcal{P}(\vec{X}_i|\vec{\lambda}) \,. \tag{4.2}$$

The maximum likelihood procedure estimates the true value of $\vec{\lambda}$ by maximizing $\mathcal{L}(\vec{\lambda})$. In doing so, the parameter set $\vec{\lambda}_0$, for which the probability to obtain the observed data is maximal, is found. It is numerically more stable to maximize the logarithm of the likelihood or equivalently minimize the so-called negative log-likelihood function

$$-\ln \mathcal{L}(\vec{\lambda}) = -\sum_{i=1}^{N} \ln \mathcal{P}(\vec{X}_i|\vec{\lambda}) \,. \tag{4.3}$$

Information about the accuracy of the estimated parameters and their correlation are provided by the covariance matrix

$$\text{cov}(\lambda_i, \lambda_j) = -\left(\frac{\partial^2}{\partial \lambda_i\, \partial \lambda_j} \ln \mathcal{L} \bigg|_{\vec{\lambda}=\vec{\lambda}_0} \right)^{-1} \,, \tag{4.4}$$

from which the error of a parameter λ_i can be calculated by:

$$\sigma_{\lambda_i} = \sqrt{\text{cov}(\lambda_i, \lambda_i)}\,. \tag{4.5}$$

To include background in a maximum likelihood fit, the total PDF can be written as

$$\mathcal{P}(\vec{X}|\vec{\lambda}) = f_S \cdot \mathcal{P}_S(\vec{X}|\vec{\lambda}_S) + (1 - f_S) \cdot \mathcal{P}_B(\vec{X}|\vec{\lambda}_B) \tag{4.6}$$

where P_S and P_B are the signal and background PDF and f_S is the fraction of signal events. After performing a likelihood fit to a data sample of N events, the signal (background) yield may be calculated as $N_S = f_S \cdot N$ ($N_B = (1 - f_S) \cdot N$). However, the error on the yield, calculated by $\sigma_{N_S} = \sigma_{f_S} \cdot N$, would be underestimated considering the sample size N as fixed quantity. A so-called extended likelihood fit ensures a proper error evaluation by taking into account that the sample size is a poisson distributed random number. The extended PDF

$$\mathcal{P}_E(\vec{X}|\vec{\lambda}) = N_S \cdot \mathcal{P}_S(\vec{X}|\vec{\lambda}_S) + N_B \cdot \mathcal{P}_B(\vec{X}|\vec{\lambda}_B)\,, \tag{4.7}$$

which is not normalized to unity but to the number of observed events enters the definition of the extended likelihood function

$$\ln \mathcal{L}(\vec{\lambda}, N_S, N_B) = \sum_{i=1}^{N} \ln \mathcal{P}_E(\vec{X}_i|\vec{\lambda}) - N_S - N_B\,, \tag{4.8}$$

which contains the signal and background yield as additional fit parameter under the constrain that $N = N_S + N_B$. After maximizing the extended likelihood function, the yields are directly accessible with consistent errors obtained from Eq. 4.5.

4.2 The *sPlot* technique

The *sPlot* technique [50] is a statistical method to disentangle the contributions of signal and background events to the distribution of a control variable x, without requiring any *a priori* knowledge on this variable. Instead, the *sPlot* technique makes use of a discriminating variable y which needs to be statistically independent of the control variable and for which the signal and background distributions, denoted as $P_S(y)$ and $P_B(y)$, respectively, are known or easy to parameterize. An unbinned extended maximum likelihood fit to the distribution of the discriminating variable is performed in oder to determine the signal (background) yield N_S (N_B) in addition to implicit free parameters which are necessary to tune the PDFs on the data sample. The joint probability density to observe an event $\vec{X} = \{x, y\}$ is given by:

$$\mathcal{P}_E(x, y) = N_S \cdot \mathcal{P}_S(x)\, P_S(y) + N_B \cdot \mathcal{P}_B(x)\, P_B(y) \tag{4.9}$$

providing that the discriminating variable is uncorrelated with the control variable. The principle behind the *sPlot* technique is to find a weight function $w_S(y)$, based on the PDF of the discriminating variable as well as the signal and background yields, which projects the signal distribution of the control variable, $\mathcal{P}_S(x)$, out:

$$\int \mathcal{P}_E(x, y)\, w_S(y)\, dy = N_S\, \mathcal{P}_S(x)\,. \tag{4.10}$$

As shown in Ref. [50], the so-called *sWeight* function:

$$w_S(y) = \frac{V_{SS}\, \mathcal{P}_S(y) + V_{SB}\, \mathcal{P}_B(y)}{N_S\, \mathcal{P}_S(y) + N_B\, \mathcal{P}_B(y)} \tag{4.11}$$

fulfills this requirement, where the matrix V_{ij} is obtained by inverting the matrix

$$V_{ij}^{-1} = \sum_{e=1}^{N} \frac{\mathcal{P}_i(y_e)\, \mathcal{P}_j(y_e)}{(N_S\, \mathcal{P}_S(y_e) + N_B\, \mathcal{P}_B(y_e))^2}\,. \tag{4.12}$$

By construction, the histogram of the control variable, where each event $\vec{X} = \{x, y\}$ is weighted with its *sWeight* $w_S(y)$, reproduces, on average, the true signal distribution.

A further powerful application of the *sWeights* is the background subtraction in maximum likelihood fits [51]. This is accomplished by constructing the weighted likelihood function

$$\ln \mathcal{L}(\vec{\lambda}) = \alpha \sum_{e=1}^{N} w_S(y_e) \cdot \ln \mathcal{P}_S(x_e | \vec{\lambda}_S)\,, \tag{4.13}$$

such that the background contribution to the likelihood function cancels out on a statistical basis. Since Eq.4.13 contains only the signal PDF, this procedure allows parameter estimation from the distribution of the control variable without explicitly modeling the background. Note that the *sWeights* are scaled with the constant

$$\alpha = \frac{\sum_{e=1}^{N} w_S(y_e)}{\sum_{e=1}^{N} w_S(y_e)^2} \tag{4.14}$$

in order to ensure a proper error evaluation [50].

5 Reconstruction and selection of the decay $B^+ \to J/\psi\,K^+\pi^+\pi^-$

To analyze the decay $B^+ \to J/\psi\,K^+\pi^+\pi^-$, it is mandatory to reconstruct and select potential signal candidates. After being produced directly in the proton-proton interaction at the primary vertex, the B^+ meson flights an average distance of approximately 1 cm before it decays at the secondary vertex. The selection exploits this event topology and particle identification information in order to separate true $B^+ \to J/\psi\,K^+\pi^+\pi^-$ events from several processes which could mimic the same signature. Among them are randomly combined tracks, which, by chance, fulfill all required selection criteria. Besides combinatorial background, real b-hadron decays in which one or several daughter particles are misidentified could wrongly be taken as signal candidates. An additional background source arises from partially reconstructed decays, where *e.g.* a neutral daughter particle is not reconstructed and the remaining decay fragment, which may also involves a misidentified particle, is interpreted as a signal candidate.

The selection is performed sequentially: during data taking, the events are filtered using the trigger strategy discussed in Sec. 5.1. Offline, a loose cut-based preselection is applied in order to obtain a signal enhanced data sample. Section 5.2 introduces the selection variables and motivates the corresponding cut criteria. The main suppression of combinatorial background is performed by using a multivariate classifier presented in Sec. 5.3. Section 5.4 summarizes the final selection.

5.1 Trigger strategy

Due to their large lifetime and low interaction rate with matter, muons leave very clean signatures in the detector which is the reason why they are excellent to trigger on. Events have to pass at least one of the trigger lines shown in Table 5.1 per trigger stage (L0, Hlt1, Hlt2). Thereby, it is required that the trigger decisions are caused by the final state particles associated with a $B^+ \to (J/\psi \to \mu^+\mu^-)K^+\pi^+\pi^-$ signal candidate, *i.e.* the events are **t**riggered **o**n **s**ignal (TOS).

On the hardware stage (L0), events are recorded if there is at least one muon candidate with a transverse momentum of $p_T(\mu) > 1.76\,\text{GeV}$ (`L0Muon`) or two muon candidates with $p_T(\mu_1) \cdot p_T(\mu_2) > (1.6\,\text{GeV})^2$ (`L0DiMuon`).

In the subsequent software trigger (Hlt1), muon (hadron) candidates are selected based on their transverse momentum and their displacement from the PV by the `Hlt1TrackMuon` (`Hlt1TrackAllL0`) line. In addition, dimuon candidates are triggered if their invariant mass is larger than $2.5\,\text{GeV}$ by the `Hlt1DiMuonHighMass` line.

The second software stage (Hlt2) needs to confirm the previous trigger decisions and can be grouped into three categories. The `Hlt2SingleMuon` line searches for a high quality track which is significantly displaced from the PV and identified as muon. Several trigger lines select events with two identified muons. If the invariant mass of the dimuon system is consistent with the nominal J/ψ mass, the event is triggered by the `Hlt2DiMuonJPsi` line or by the `Hlt2DiMuonJPsiHighPT` line with an additional constrain on the transverse

momentum of the J/ψ candidate ($p_T(J/\psi) > 2\,\mathrm{GeV}$) whereas the `Hlt2DiMuonDetached` line selects dimuon candidates without a mass requirement if the dimuon vertex is well separated from the primary vertex. The `Hlt2DiMuonDetachedHeavy` line is a combination of both. Moreover, the topological trigger lines `Hlt2Topo[2,3,4]BodyBBDT` dedicated to search for decays of B mesons into N particles are used. The `Hlt2TopoMu[2,3,4]BodyBBDT` triggers additionally require that at least one of the decay particles is identified as muon. More details on the various trigger lines can be found in Refs. [52,53].

Table 5.1: Trigger requirements for the analysis of $B^+ \to J/\psi\, K^+\pi^+\pi^-$ decays.

Trigger level	Trigger decision
L0	LOMuon
	LODiMuon
HLT1	Hlt1TrackAllL0
	Hlt1TrackMuon
	Hlt1DiMuonHighMass
HLT2	Hlt2SingleMuon
	Hlt2DiMuonDetached
	Hlt2DiMuonDetachedHeavy
	Hlt2DiMuonJPsi
	Hlt2DiMuonJPsiHighPT
	Hlt2Topo[2,3,4]BodyBBDT
	Hlt2TopoMu[2,3,4]BodyBBDT

5.2 Preselection

The applied selection criteria, given in Sec. 5.2.1, are guided by the LHCb analysis of the rare decay $B^+ \to K^+\pi^+\pi^-\mu^+\mu^-$ [54], where the same final states particles as in the signal mode are involved and the amplitude analysis of $B^0 \to \psi(2S)K^+\pi^-$ [13]. In Section 5.2.2 potential background sources surviving the preselection are studied. The signal yield after the preselection is extracted from data using an unbinned maximum likelihood fit to the reconstructed B^+ mass as described in Sec. 5.2.3.

5.2.1 Selection criteria

The decay $B^+ \to (J/\psi \to \mu^+\mu^-)K^+\pi^+\pi^-$ involves five stable[13] and charged particles in the final state which leave signatures (hits) in the tracking detectors. Their trajectories are reconstructed by fitting a track to the detector hits. High quality tracks are selected by requiring the track fit χ^2_{track} divided by the degrees of freedom to be smaller than four.

To distinguish between particles originating from long lived B mesons and particles produced directly at the primary interaction point the impact parameter (IP), defined as the minimum distance of a track to the primary vertex, is used. As the daughter particles of the B^+ meson come from a detached secondary vertex they are expected to have, on average, a high impact parameter or equivalently, a high impact parameter significance χ^2_{IP}, which is given by the increase of the vertex fit χ^2 when adding the respective particle track to the fit of the primary vertex. Consequently, all tracks have to satisfy the condition $\chi^2_{IP} > 9$.

The mass of the B^+ meson is much higher than the rest mass of the decay products leading to high momentum daughters which is why the hadron candidates have to pass the threshold $p_T > 200\,\mathrm{MeV}$. This requirement on the transverse momentum is kept loose in order to avoid introducing a bias on the decay kinematics.

Informations from the sub-detectors dedicated for particle identification (as described in Sec. 3.1.2) are combined to assign a likelihood value $\mathcal{L}(X)$ to each particle which describes how likely the respective particle belongs to the species X. The particle hypothesis is compared to the pion hypothesis being the most abundant particle species within the detector:

$$\Delta ln\mathcal{L}_{X\pi} = ln\mathcal{L}(X) - ln\mathcal{L}(\pi)\,, \tag{5.1}$$

such that $\Delta ln\mathcal{L}_{X\pi} > 0$ indicates that the particle is more likely of type X than a pion. Therefore, muon candidates with $\Delta ln\mathcal{L}_{\mu\pi} > 0$ are selected. Moreover, the `IsMuon` tag must be assigned to the muon candidates which is a requirement on the number of passed muon stations depending on the momentum [55]. Kaons and pions are harder to distinguish such that tighter requirements are necessary to ensure correct particle identification. To separate the hadrons, kaon candidates with $\Delta ln\mathcal{L}_{K\pi} > 3.5$ are selected whereas pion candidates need to have a $\Delta ln\mathcal{L}_{K\pi}$ value smaller than 14.5. It is additionally required that $\Delta ln\mathcal{L}_{K\pi}(K^+) - \Delta ln\mathcal{L}_{K\pi}(\pi^+) > 10$ in order to reject $B^+ \to J/\psi K^+\pi^+\pi^-$ signal candidates where the K^+ is misidentified as π^+ and vice-versa.

---

[13]In this context, all particles which do not decay within the detector are considered as stable.

Two oppositely charged muon candidates are combined to form a J/ψ candidate, where the invariant mass of the dimuon system has to be consistent with the nominal J/ψ mass (within ± 60 MeV). The muon tracks are fitted to a common vertex which is required to be of a certain quality ($\chi^2_{vtx}/ndf(J/\psi) < 12$).

The reconstructed J/ψ meson is combined with the three hadron candidates (K^+, π^+, π^-) to build a B^+ meson candidate, where the fit of the B^+ decay vertex needs to fulfill $\chi^2_{vtx}/ndf(B) < 5$. As the B^+ meson is supposed to originate from the primary vertex, the impact parameter significance has to be smaller than 16. The transverse momentum of the B^+ candidate has to be above the threshold $p_T > 2$ GeV.

The decay time of the B^+ candidate can be calculated by measuring the flight distance $\vec{d}$ after which the B^+ decays given by the vector pointing from the primary vertex to the decay vertex, via:

$$ t = \frac{|\vec{d}|}{|\vec{p}_B|} m_B \,, \tag{5.2} $$

where $\vec{p}_B$ and m_B denote the reconstructed momentum and mass of the B^+ candidate, respectively. Combinatoric background events from tracks originating from the primary vertex are largely suppressed by imposing the conditions $t > 0.3\,ps$ and $\chi^2_{FD} > 121$, where χ^2_{FD} is given by the square of the flight distance divided by its uncertainty. Furthermore, the flight direction $\vec{d}$ should be consistent with the direction of the reconstructed B^+ momentum $\vec{p_B}$. Hence, the cosine of the direction angle defined as

$$ DIRA = cos(\theta) = \frac{\vec{d} \cdot \vec{p}_B}{|\vec{d}||\vec{p}_B|} \tag{5.3} $$

needs to be very close to one ($DIRA > 0.9999$). Table 5.2 summarizes all selection requirements.

Table 5.2: Selection requirements for the decay $B^+ \to J/\psi\, K^+\pi^+\pi^-$.

	Variable	Cut
Tracks	χ^2_{track}/ndf	< 4
	$\chi^2_{IP}(tracks)$	> 9
	$p_T(hadrons)$	$> 200\,\text{MeV}$
	$\Delta ln\mathcal{L}_{K\pi}(K)$	> 3.5
	$\Delta ln\mathcal{L}_{K\pi}(\pi)$	< 14.5
	$\Delta ln\mathcal{L}_{K\pi}(K^+) - \Delta ln\mathcal{L}_{K\pi}(\pi^+)$	> 10
	$\Delta ln\mathcal{L}_{\mu\pi}(\mu)$	> 0
	$\texttt{IsMuon}(\mu)$	True
$J/\psi \to \mu^+\mu^-$	$m(J/\psi)$	$\in [3037, 3157]\,\text{MeV}$
	$\chi^2_{vtx}/ndf(J/\psi)$	< 12
	$\chi^2_{FD}(J/\psi)$	> 9
$B^+ \to J/\psi\, K^+\pi^+\pi^-$	$m(B)$	$\in [5200, 5600]\,\text{MeV}$
	$\chi^2_{vtx}/ndf(B)$	< 5
	$\chi^2_{IP}(B)$	< 16
	$p_T(B)$	$> 2\,\text{GeV}$
	$t(B)$	$> 0,3\,\text{ps}$
	$\chi^2_{FD}(B)$	> 121
	$DIRA(B)$	> 0.9999
$B^0 \to J/\psi\, K^+\pi^-$ veto	$m(J/\psi\, K^+\pi^-)$	$\neq m(B^0)_{PDG} \pm 50\,\text{MeV}$

5.2.2 Background composition

A potential background source is arising from true $B^0 \to J/\psi\, K^+\pi^-$ decays combined with an additional random pion. The invariant mass distribution of the $J/\psi\, K^+\pi^-$ system in Fig. 5.1 (left) shows indeed an enhancement around the nominal B^0 mass $m_{B^0} = 5279.55\,\mathrm{MeV}$ [31]. Since the B^+ mass is approximately equal to the B^0 mass, the combination of a true B^0 meson with a random pion pushes the reconstructed invariant mass of the $J/\psi\, K^+\pi^+\pi^-$ system outside of the signal region defined as $m_{B^+} \pm 60\,\mathrm{MeV} = (5279.25 \pm 60)\,\mathrm{MeV}$ [31]. This is verified in Fig. 5.1 (right) which shows the reconstructed B^+ mass for events consistent with a $B^0 \to J/\psi\, K^+\pi^-$ decay. There is clearly no background contribution observed in the signal region. Nevertheless, it is important to veto these background events in order to obtain a clean combinatorial background sample which can be reliably interpolated into the signal region. Therefore, events with $m(J/\psi\, K^+\pi^-) = m_{B^0} \pm 50\,\mathrm{MeV}$ are rejected.

Inclusive $B^0 \to J/\psi\, X$ and $B^0_s \to J/\psi\, X$ MC events provide access to potential peaking background sources due to partially reconstructed decays and particle misidentification. Figure 5.2 (left) shows no evident structure in the distribution of the reconstructed B^+ mass for $B^0_s \to J/\psi\, X$ events whereas a background contribution from partially reconstructed $B^0 \to J/\psi\, X$ decays can be seen at low invariant masses in Fig. 5.2 (right). These background events include, for example, $B^0 \to J/\psi\, K^+\pi^-\pi^+\pi^-$ decays where one of the hadrons is missed out in the reconstruction or $B^0 \to J/\psi\, K^+\pi^-\pi^0$ decays where the neutral particle is not reconstructed and replaced by a random low momentum track. Due to the missing momentum, the reconstructed B^+ mass is systematically below the signal region. This low mass background is rejected by requiring the reconstructed B^+ mass to be larger than $5200\,\mathrm{MeV}$. The remaining combinatorial background is described in the next subsection.
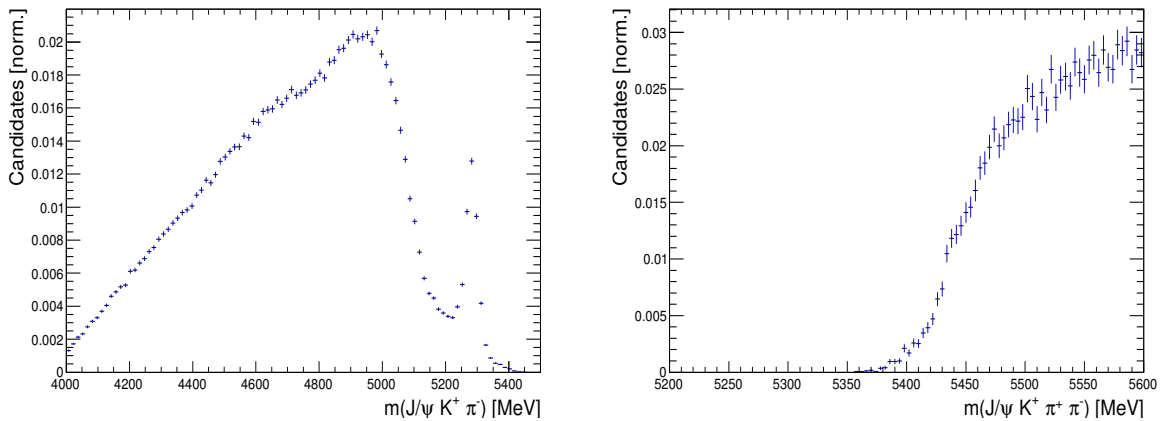
Figure 5.1: Invariant mass distribution of the $J/\psi\, K^+\pi^-$ system (left) and reconstructed B^+ mass for events with $m(J/\psi\, K^+\pi^-) = m_{B^0} \pm 50\,\mathrm{MeV}$ (right).
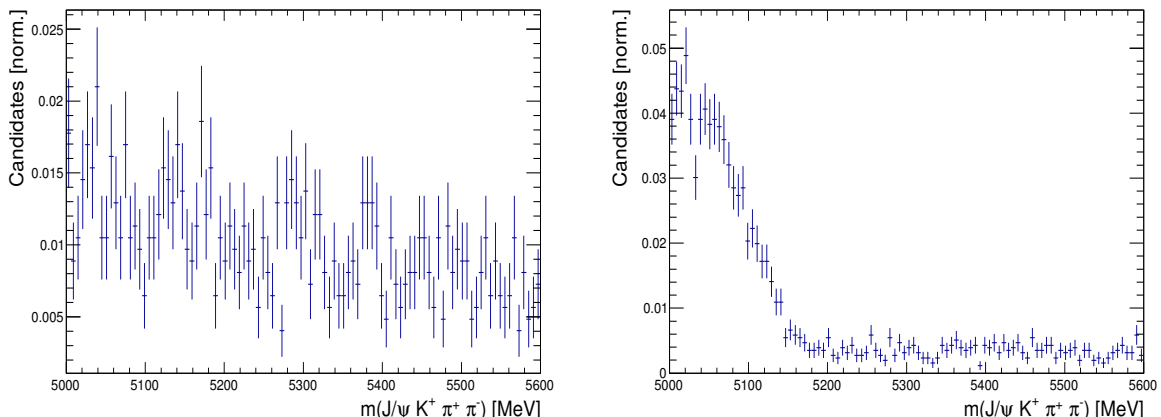
Figure 5.2: Reconstructed B^+ mass for inclusive $B_s^0 \to J/\psi X$ (left) and $B^0 \to J/\psi X$ (right) MC events.

5.2.3 Signal and background yields

An extended unbinned maximum likelihood fit to the reconstructed B^+ mass of the selected events is performed in order to determine the signal yield. Figure 5.3 shows the invariant mass spectrum which can be described by a probability density function composed of a signal and a background part:

$$\mathcal{P}(m) = N_{sig} \cdot \mathcal{S}(m) + N_{bkg} \cdot \mathcal{B}(m), \tag{5.4}$$

with $m := m(J/\psi K^+ \pi^+ \pi^-)$. The mass resolution being much larger than the natural decay width necessitates an empirical description of the signal shape. For this purpose a so-called Crystal Ball function [56] is used, which consists of a Gaussian core and a radiative tail towards low masses described by a polynomial. It is defined as:

$$CB(m; \mu, \sigma, \alpha, n) = N \cdot \begin{cases} \exp\left(-\frac{(m-\mu)^2}{2\sigma^2}\right) & \text{, for } \frac{m-\mu}{\sigma} > -\alpha \\ \left(\frac{n}{|\alpha|}\right)^n \cdot \exp\left(-\frac{|\alpha|^2}{2}\right) \cdot \left(\frac{n}{|\alpha|} - |\alpha| - \frac{m-\mu}{\sigma}\right)^{-n} & \text{, for } \frac{m-\mu}{\sigma} \leqslant -\alpha \end{cases} \tag{5.5}$$

where μ and σ are the mean and the width of the gaussian core, α and n are the starting point and the order of the polynomial function and N accounts for a proper normalization. The signal PDF consists of the sum of two Crystal Ball functions which differ only by their widths σ_i:

$$\mathcal{S}(m) = f \cdot CB(m; \mu, \sigma_1, \alpha, n) + (1 - f) \cdot CB(m; \mu, \sigma_2, \alpha, n) \tag{5.6}$$

where f is the fraction of the first Crystal Ball function. The combinatorial background shape is parameterized as a linear function with slope c:

$$\mathcal{B}(m) = \frac{1 + c \cdot m}{(m_{max} - m_{min}) + \frac{c}{2}(m_{max} - m_{min})^2}. \tag{5.7}$$

44

The fit result is shown in Fig. 5.3 and the fit parameter values are listed in Table 5.3. The number of signal events after the preselection extracted from the fit is $N_{sig} = 163\,671 \pm 674$ with a background level of 24% within the signal region.
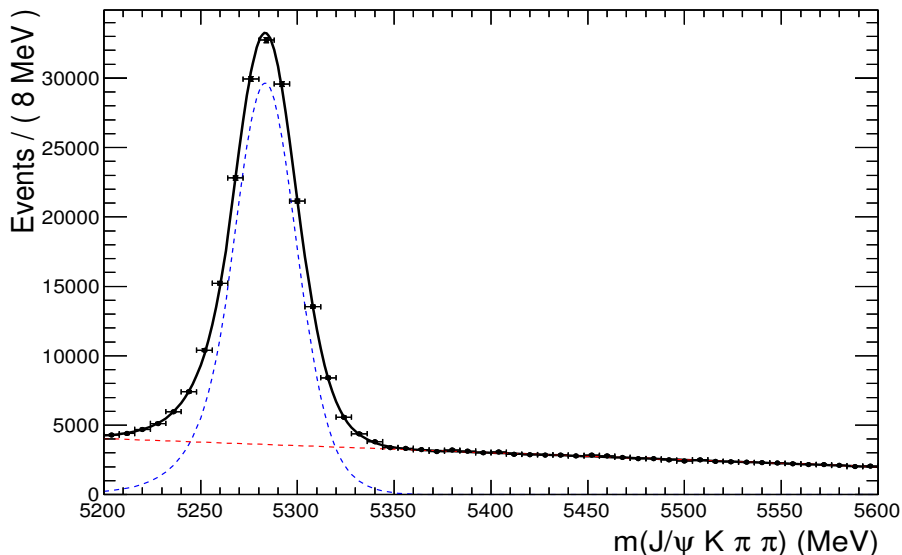
Figure 5.3: Reconstructed B^+ mass for events that pass the preselection. The complete PDF is shown in black, the signal component in blue and the background component in red. The goodness of fit is given by $\frac{\chi^2}{ndof} = 0.98$.

Table 5.3: Fitted parameters with their statistical uncertainty.

Fit parameter	Estimate
μ	$5\,283.37 \pm 0.07\,\text{MeV}$
σ_1	$14.97 \pm 0.34\,\text{MeV}$
σ_2	$23.46 \pm 0.55\,\text{MeV}$
f	0.663 ± 0.064
α	1.327 ± 0.023
n	11.3 ± 3.2
c	$-0.3387 \pm 0.0066\,\text{MeV}^{-1}$
N_S	$163\,671 \pm 674$
N_B	$150\,704 \pm 665$

5.3 Multivariate classification

Instead of a simple cut-based selection, multivariate analysis tools can be used to discriminate signal from background. A multivariate classifier maps the n-dimensional space of the observable variables $\vec{x} = \{x_1, x_2, ..., x_n\}$ to an one dimensional output called the classifier response :

$$t(\vec{x}) : \ \mathbb{R}^n \to \mathbb{R} \tag{5.8}$$

The classifier response combines the information of the input variables, including their correlation, into one powerful discriminator.

Multivariate analysis techniques are based on supervised machine learning algorithms, which make use of clean signal and background samples in order to find the mapping function $t(\vec{x})$. These samples may be taken from MC simulation. Due to the limited statistics of the training samples the classifier could be overtrained, which means that the machine learning does not pick up actual signal or background properties, but statistical fluctuations. The performance of an overtrained classifier is better on the training sample than on any statistical independent data sample. Therefore, overtraining can be detected by comparing the performance between the training and an independent test sample.[14] Finally, the trained classifier can be applied to a data sample with unknown composition.

Section 5.3.1 introduces **b**oosted **d**ecision **t**rees (BDT [57]), the multivariate analysis technique used in this analysis. The training phase of the BDT is discussed in Sec. 5.3.2. The **T**oolkit for **M**ulti**v**ariate Data **A**nalysis (TMVA [58]) is used to train and evaluate the multivariate classifier.

5.3.1 Boosted decision trees

Decision **t**rees (DT) are a natural extension of simple cuts, but instead of discarding all events that fail a certain cut, wrongly classified events get a second chance to be classified correctly. Therefore, a much higher signal efficiency can be achieved.

A decision tree categorizes the events of a data sample based on a successive application of binary splits, as sketched in Fig. 5.4. Starting from the root node, a sequence of cuts divide the data into signal- and background-like subsamples. At each node of the DT the discrimination variable which provides the best separation power [15] is used to determine the optimal cut criterion. The division is repeated until a node has reached a certain minimum number of events (3 % of the total events in this analysis) or the maximum tree depth (equal to three in this analysis) is reached. These final "leaf" nodes are classified to be either signal or background-like according to the majority of the events inside the respective leaf. Consequently the discrete valued response function of the DT returns $DT(\vec{x}) = +1$ ($DT(\vec{x}) = -1$) if an event $\vec{x}$ ends up in a signal (background) leaf.

A shortcoming of decision trees is their instability with respect to statistical fluctuation in the training sample (e.g. the decision of the optimal cut criterion at a certain node may

---

[14]Half of the events are used for training, the other half for testing.

[15]The quality of separation is defined by the so-called Gini index: $p \cdot (1 - p)$, where $p = \frac{S}{S+B}$ and S (B) is the number of signal (background) events.

be influenced by a statistical fluctuation in the training sample), i.e. they are sensitive to overtraining. To stabilize the DT response and significantly improve the performance, a so called boosting is applied. The principle behind boosting is that misclassified events from the training sample are given a larger weight than events which are in the correct leaf node. The **ada**ptive **boost** algorithm (AdaBoost [59]) re-weights misclassified events with the common boost weight:

$$\alpha = \frac{1 - err}{err},$$
(5.9)

where err is the fraction of misclassified events. The resulting reweighed training sample is then used to train a new decision tree. Repeating the boosting procedure several times (500 times in this analysis) leads to a set of decision trees (called a "decision forest"), where each tree learns from the errors of the previous ones. In the end, the boosted classifier response is given by the weighted average of the individual ones :

$$BDT(\vec{x}) = \frac{1}{N_{trees}} \sum_{i}^{N_{trees}} ln(\alpha_i) \cdot DT_i(\vec{x}).$$
(5.10)
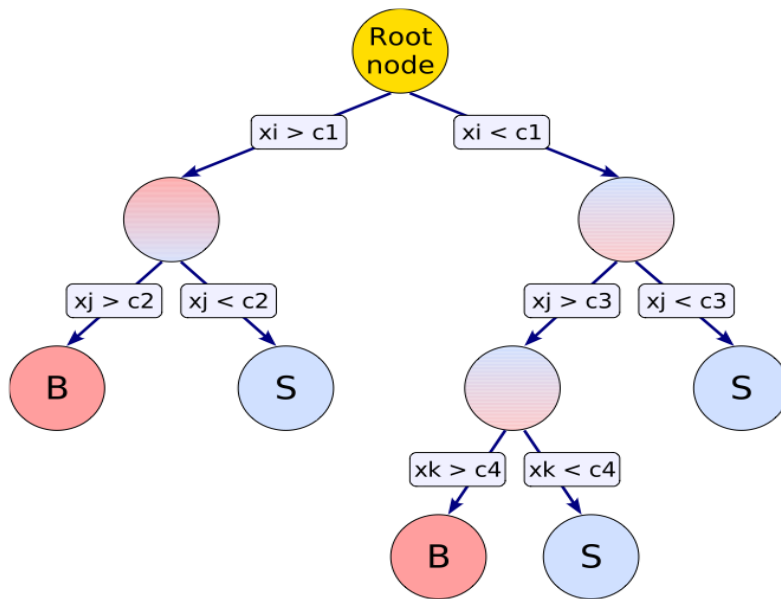
Figure 5.4: Schematic view of a decision tree. Starting from the root node, a sequence of binary splits using the discriminating variables $\vec{x}$ is applied to the data. [58]

5.3.2 Training of the multivariate classifier

The BDT training samples are taken from LHCb data that passes the preselection presented in Sec. 5.2. The background is statistically subtracted by applying $sWeights$ based on the fit to the reconstructed B^+ mass, described in Sec. 5.2.3, in oder to obtain the signal training sample whereas background events are sampled from the right hand sideband $(m(B) > 5350\,\text{GeV})$.

A disadvantage of using data to train the multivariate classifier is the fact that the issue of overtraining becomes more crucial if the training sample is reused in the final analysis. In doing so, the training and analysis sample obviously share the same statistical fluctuations and therefore a multivariate classifier being sensitive to statistical fluctuations in the training samples introduces a bias on the efficiency. As overtraining can not be completely avoided, a so-called cross training is applied. For this purpose, the data set is randomly split into two subsamples and with each of them an independent BDT is trained (and tested), which is then applied to the other subsample. This procedure ensures having statistically independent training and analysis samples with the cost of having only half of the statistics to train each of the BDTs. However, the statistics is high enough such that this becomes no issue.

The BDT training uses only variables which are fairly insensitive to the decay kinematics. Among them are the following variables associated with the B^+ candidate: p_T, $log(\chi^2_{FD})$, χ^2_{IP}, χ^2_{vtx} and $log(1 - DIRA)$.[16] In addition, the smallest impact parameter significance among the tracks and the $\Delta ln\mathcal{L}_{K\pi}$ value of the kaon candidate are included. A further input variable is the cosine of the largest opening angle $\theta_{J/\psi h}$ between the J/ψ and the hadron candidates in the plane transverse to the beam. This variable peaks at positive values for the signal since the B^+ meson has a high transverse momentum while combinatorial background is uniformly distributed and background events that combine particles from two different b hadrons peak at negative values. The signal and background distributions of the training variables are shown in Fig. 5.5. In Table 5.4 (left) the input variables are ranked according to their separation $\langle S^2 \rangle$ calculated by [58]:

$$\langle S^2 \rangle = \frac{1}{2} \int \frac{(\mathcal{P}_S(x) - \mathcal{P}_B(x))^2}{\mathcal{P}_S(x) + \mathcal{P}_B(x)} dx\,, \tag{5.11}$$

where $\mathcal{P}_S(x)$ and $\mathcal{P}_B(x)$ are the signal and background probability functions of the classifier x. For identical signal and background shapes the separation is zero and one in case of no overlap at all. The BDT response, which has a much better separation power of $\langle S^2 \rangle = 64\%$ than the individual training variables, is plotted in Fig. 5.6 for both random subsamples. For the purpose of an overtraining check, the classifier response evaluated with the training sample and an independent test sample are plotted superimposed. The BDT shows similar performance in both cases. Hence, there is clearly no indication of overtraining. Furthermore, the performance of the two cross-trained BDTs is consistent. After training the BDT, a measure of the variable importance can be derived by counting

---

[16]Due to Lorentz invariance, the decay kinematics does not depend on the momentum of the mother particle.
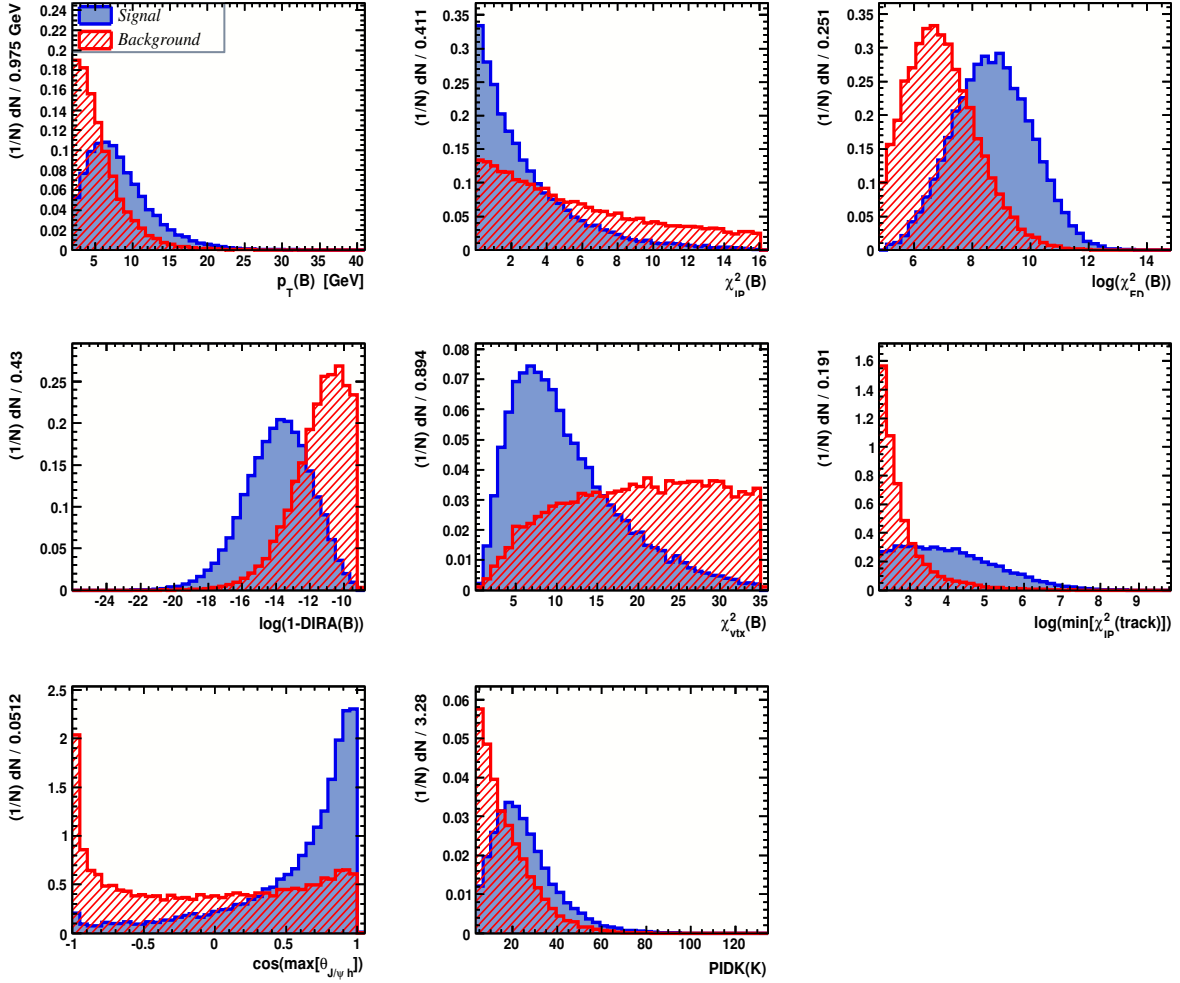
Figure 5.5: Input variables used to train the BDT. Histograms in blue show *sWeighted* data and histograms in red show combinatorial background.

Table 5.4: BDT input variables ranked according to their separation (left) and importance (right).

Variable	Separation [%]	Variable	Importance [%]
$log(1 - DIRA(B))$	34	$log(min[\chi^2_{IP}(tracks)])$	17.2
$log(min[\chi^2_{IP}(tracks)])$	33	$\Delta ln\mathcal{L}_{K\pi}(K)$	15.3
$log(\chi^2_{FD}(B))$	33	$log(\chi^2_{FD}(B))$	12.6
$\chi^2_{vtx}(B)$	25	$cos(max[\theta_{J/\psi h}])$	12.6
$cos(max[\theta_{J/\psi h}])$	23	$\chi^2_{vtx}(B)$	12.0
$p_T(B)$	13	$\chi^2_{IP}(B)$	10.5
$\chi^2_{IP}(B)$	13	$log(1 - DIRA(B))$	10.5
$\Delta ln\mathcal{L}_{K\pi}(K)$	12	$p_T(B)$	9.3

Figure 5.6: Signal and background distributions for the BDT response. Training and test samples are superimposed to probe overtraining. The left and right plot show the BDT response for the two random subsamples. Each BDT is then applied to the subsample which was not used to train it (cross training).

how often the variable is used to split DT nodes whereby each split occurrence is weighted by the achieved separation gain-squared and also by the number of events in the node [58].[17] Note that this does not fully reflect the variable importance since removing one variable could be compensated by correlated variables and sometimes, only certain combinations of variables make sense. Table 5.4 (right) shows the importance ranking. The BDT is explicitly designed not to introduce any bias on the decay kinematics or the reconstructed B^+ mass. In order to verify this assumption, Fig. 5.7 (left) and Fig. 5.7 (right) show the average BDT response for signal and background as a function of the reconstructed B^+ mass and the invariant mass of the $K^+\pi^+\pi^-$ system, respectively. There is clearly no correlation visible such that the acceptance of the BDT can be considered as reasonably flat.
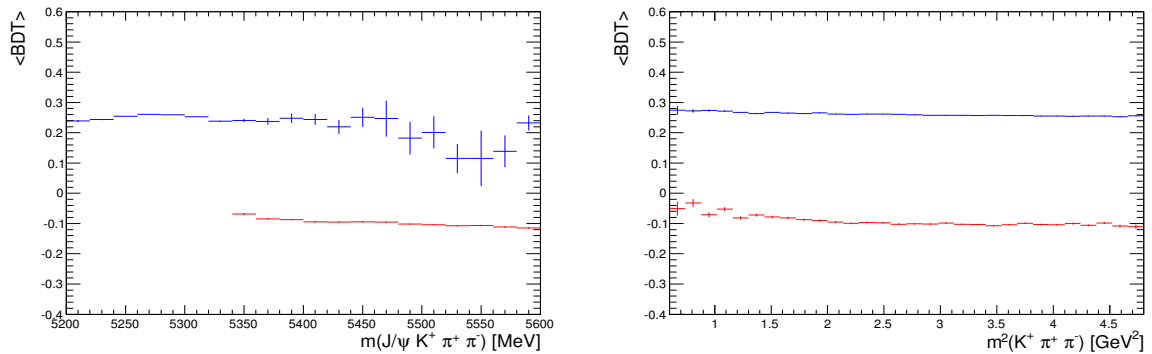
Figure 5.7: Average BDT response for $sWeighted$ data (blue) and sideband data (red) as a function of $m(J/\psi\,K^+\pi^+\pi^-)$ (left) and $m^2(K^+\pi^+\pi^-)$ (right).

---

[17]The separation gain is defined as : $g(\text{parent node}) - g(\text{daughter node 1}) - g(\text{daughter node 2})$, where $g = p(1-p)$ is the Gini index and p is the purity.

5.4 Final selection

Figure 5.8 shows the signal efficiency, background efficiency, signal significance and purity as a function of the applied BDT cut. In general, it is desirable to maximize the signal significance $S/\sqrt{S+B}$, which is a measure of the statistical significance of the measurement. The corresponding cut on the classifier response is $BDT > -0.07$ achieving a signal significance of $S/\sqrt{S+B} = 377$ at a signal efficiency of $\epsilon_S = 97\%$ and a background rejection of $1 - \epsilon_B = 68\%$. This corresponds to an improvement of 8% with respect to the signal significance after the preselection ($S/\sqrt{S+B} = 350$) while keeping almost all signal events. Nonetheless, the signal significance is not the optimal figure of merit for this analysis since it reflects only the statistical error. A poorly understood background can lead, however, to a large systematic error making a low statistical error irrelevant. Therefore, the BDT cut is chosen to be $BDT > 0.1$ corresponding to a signal efficiency of $\epsilon_S = 80\%$ and a background rejection of 92% in order to reduce the background level as much as possible while maintaining a high signal yield.

After applying the BDT cut, multiple candidates occur in fewer than 1.2% of events. The requirement of a single candidate per event is enforced by selecting randomly one of them.

The number of signal events that pass the final selection composed of trigger, preselection, BDT cut and candidate selection is estimated to be $N_S = 129\,511 \pm 459$ by performing a fit to the reconstructed B^+ mass, as shown in Figure 5.9. The same PDF as in Sec. 5.2.3 is used and the corresponding fit parameter values are listed in Table 5.9. After the final selection, the background level within the signal region is reduced to 3.9%.
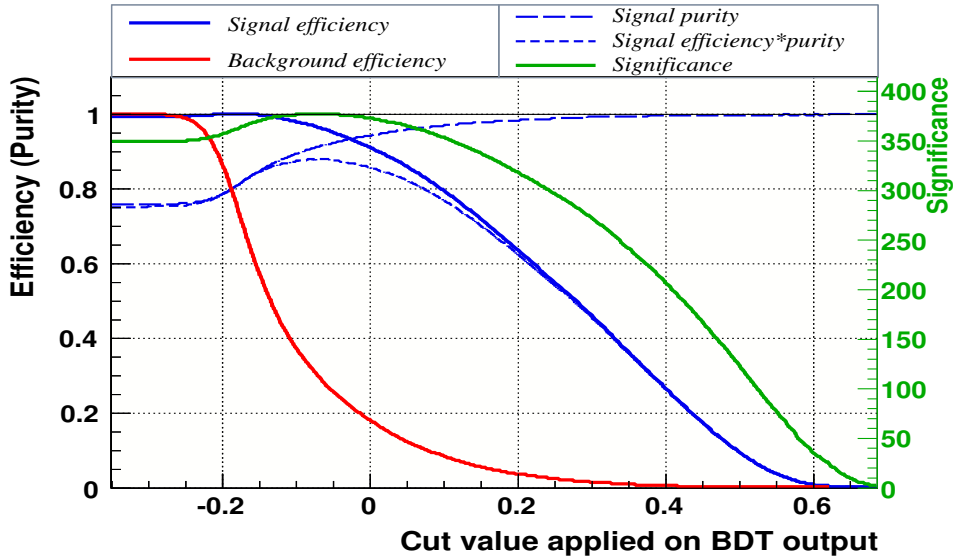
Figure 5.8: Signal efficiency, background efficiency, signal significance and purity of the BDT. The chosen working point ($\epsilon_S = 80\%$, $\epsilon_B = 8\%$) corresponds to the cut: $BDT > 0.1$.
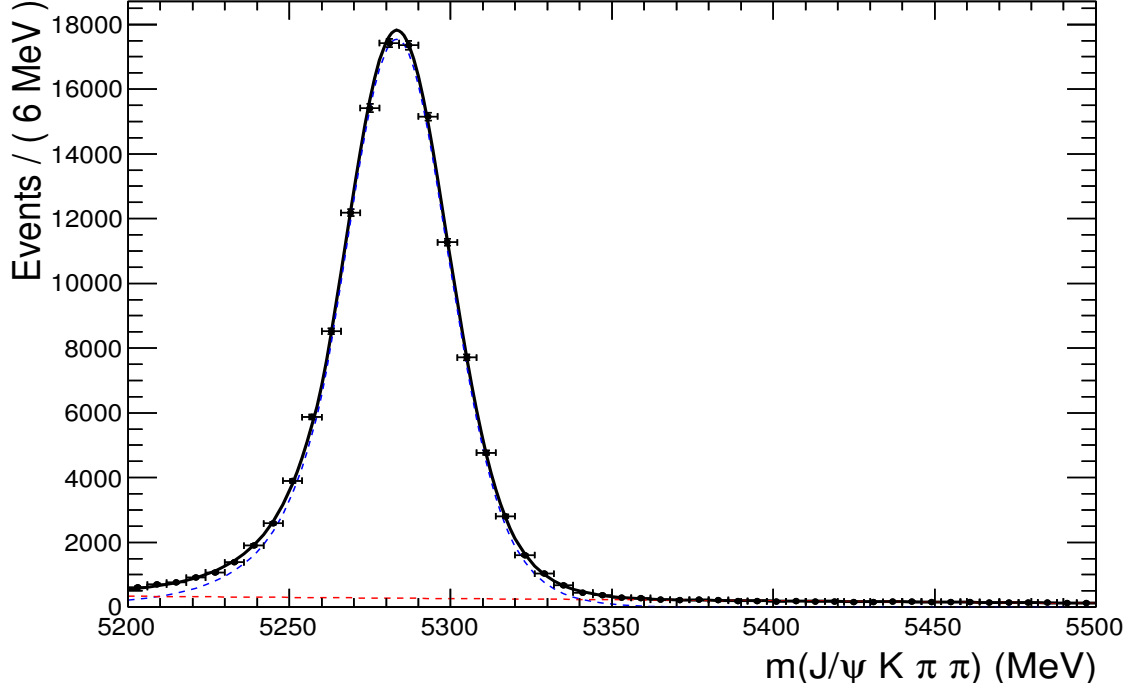
Figure 5.9: Reconstructed B^+ mass for events that pass the final selection. The complete PDF is shown in black, the signal component in blue and the background component in red. The goodness of fit is given by $\frac{\chi^2}{ndof} = 1.28$.

Table 5.5: Fitted parameters with their statistical uncertainty.

Fit parameter	Estimate
μ	$5\,283.32 \pm 0.07\,\text{MeV}$
σ_1	$25.21 \pm 0.85\,\text{MeV}$
σ_2	$15.29 \pm 0.51\,\text{MeV}$
f	0.255 ± 0.033
α	1.38 ± 0.03
n	7.0 ± 1.1
c	$-0.47 \pm 0.03\,\text{MeV}^{-1}$
N_S	$129\,511 \pm 459$
N_B	$11\,417 \pm 306$

6 Detection efficiency

In this Chapter, the influence of the detector acceptance in combination with the reconstruction and selection process on the phase space distribution is investigated. Since the different phase space regions are populated by events with different kinematic properties, the selection efficiency is not uniform over the phase space. As a consequence, the phase space distribution is distorted which needs to be taken into account when extracting parameters from measured data, *i.e.* the efficiency has to be included in the PDF

$$\mathcal{P}(X) \to \varepsilon(X)\,\mathcal{P}(X)\,. \tag{6.1}$$

The acceptance function $\epsilon(X)$, defined as the fraction of events that have been selected at a given phase space position X, is obtained from simulation by comparing the phase space distribution after the selection with the generated one

$$\varepsilon(X) = \frac{N_{sel}(X)}{N_{gen}(X)}\,, \tag{6.2}$$

where $N_{sel}(X)$ denotes the number of events that passed the selection and $N_{gen}(X)$ the number of generated events. Since the description of the phase space acceptance relies completely on simulated events, it is mandatory that the simulation accurately reproduces the measured data. This is verified in Sec. 6.1, where simulated MC events are compared to background subtracted data. The acceptance function is determined in Sec. 6.2.

6.1 Comparison of data and simulation

In the following, kinematic and topological distributions of truth matched MC events are compared to signal data distributions. The latter are obtained by making use of the *sPlot* technique as described in Sec. 4.2. To account for differences between simulation and data, several data-driven correction methods are applied to simulated events. In particular, the track reconstruction efficiency for simulated events is corrected in Sec. 6.1.1. The performance of the particle identification is, in general, better for simulated events than for real data. Section 6.1.2 presents a method to ensure a realistic particle identification for simulated events. The final agreement between data and simulation is discussed in Sec. 6.1.3.

6.1.1 Tracking efficiency

The probability to reconstruct a track ("tracking efficiency") depends mainly on the particle kinematics and the track multiplicity, *i.e.* the number of charged particles in the event. The relative tracking efficiency between data and MC simulation has been measured in Ref. [60] using $J/\psi \to \mu^+\mu^-$ decays in a tag and probe approach. Figure 6.1 (left) shows the resulting efficiency ratio

$$R_{track} = \frac{\epsilon_{track}(data)}{\epsilon_{track}(MC)} \tag{6.3}$$
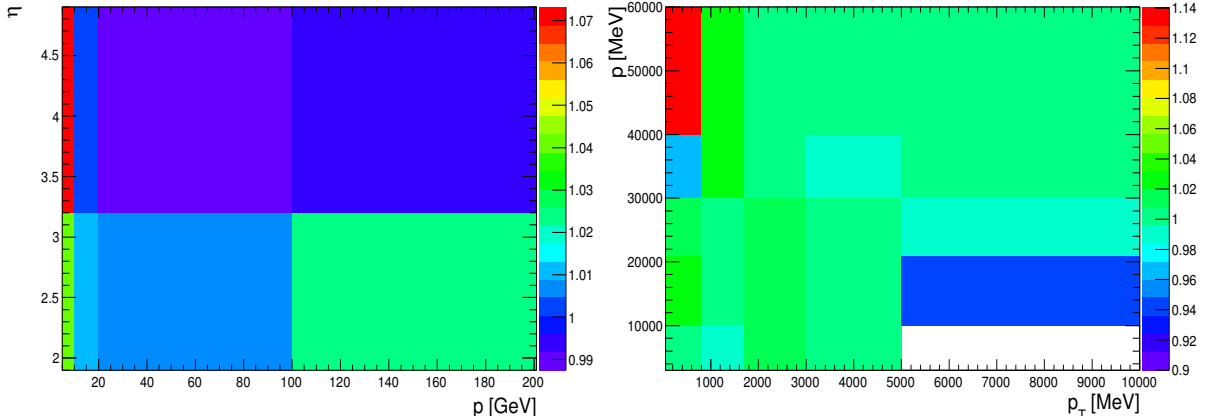
Figure 6.1: Tracking efficiency ratio (left) and `IsMuon` efficiency ratio (right) for data and MC simulated events.

in bins of momentum p and pseudorapidity η.[18] To correct the tracking efficiency in simulated MC events, for each track a weight is assigned corresponding to the efficiency ratio in the respective bin. The MC sample is subsequently re-weighted with the total event weight given by the product of all track weights.

6.1.2 Particle identification

To account for the different performance of the `IsMuon` requirement for data and simulated MC events, the efficiency ratio

$$R_{\texttt{IsMuon}} = \frac{\epsilon_{\texttt{IsMuon}}(data)}{\epsilon_{\texttt{IsMuon}}(MC)} \,, \tag{6.4}$$

shown in Fig. 6.1 (right), is assigned as weight to the simulated muon candidates depending on their momentum and transverse momentum.

The performance of the muon identification is in a good agreement between data and MC simulation as shown in Fig. 6.2. In contrast, the simulation does not accurately reproduce the particle identification of hadrons. Therefore, the particle identification variable $\Delta\mathcal{L}_{K\pi}$ is resampled for kaon and pion candidates by making use of a clean calibration data sample [61]. In this procedure, the decay mode $D^{*+}(2010) \rightarrow (D^0 \rightarrow K^-\pi^+)\pi_s^+$ is reconstructed and selected based on the decay kinematics alone, without using particle identification information. The expected $\Delta\mathcal{L}_{K\pi}$ distribution for kaons and pions is then extracted from the calibration sample in bins of particle momentum, pseudorapidity and track multiplicity in order to account for the different kinematics of the calibration and signal decay mode. These distributions are used as PDFs to generate new values for $\Delta\mathcal{L}_{K\pi}$

---

[18]The pseudorapidity is defined as $\eta = -\ln\left[\tan\left(\frac{\theta}{2}\right)\right]$ where θ is the angle between the particle momentum and the beam axis.
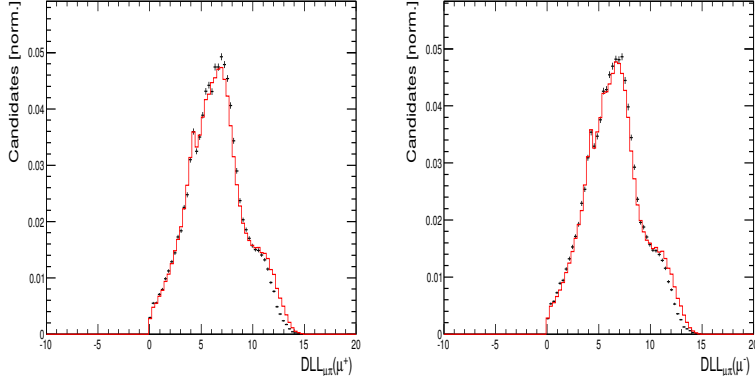
Figure 6.2: Comparison of muon identification variables for data (black) and MC events (red).
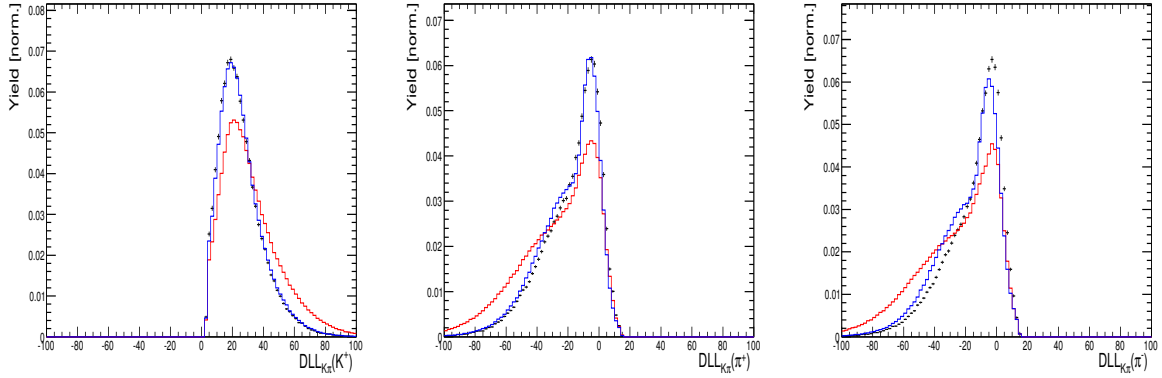
Figure 6.3: Comparison of particle identification variables for data (black) and MC simulated events before (red) and after resampling (blue) for each hadron.

for each simulated hadron candidate according to its momentum, pseudorapidity and the number of tracks in the event. In doing so, the agreement between data and simulation improves significantly as can be seen in Fig. 6.3 where the particle identification variables before and after resampling are compared.

6.1.3 Agreement between data and simulation after corrections

As shown in Fig. 6.4, the simulated p_T and χ^2_{vtx} distributions for B^+ meson candidates as well as the distribution of the track multiplicity differ from data. Since the selection efficiency depends especially on the B^+ meson kinematics and the detector occupancy, simulated events are re-weighted to match the $p_T(B)$ and track multiplicity data distributions. For this purpose, the corresponding weights are obtained by dividing the data distribution of the respective variable by the simulated distribution, where both are normalized to the same number of events. The re-weighting does not influence the distribution of statistically independent variables as the weights average to unity. The same procedure is applied to the $\chi^2_{vtx}(B)$ distribution since the B^+ vertex quality is used in the BDT training.

The p, p_T and χ^2_{IP} distributions of all final state particles are compared for data and MC simulation in Appendix B. After re-weighting in $p_T(B)$, the agreement in the kinematic distributions of the final state particles has improved, too. There is a remaining discrepancy in the decay kinematics, especially at low π^- momenta, which is, however, expected due to the fact that the simulation includes only (phase space) decays which are distributed uniformly in phase space whereas the real physics decay proceeds mainly via intermediate resonances. Additionally, there are small variations in the χ^2_{IP} distributions of the final state particles. Although these are important input variables for the multivariate classifier, no further corrections are applied since the BDT performance on simulated events is, nevertheless, consistent with the performance observed on real data as shown in Fig. 6.5.
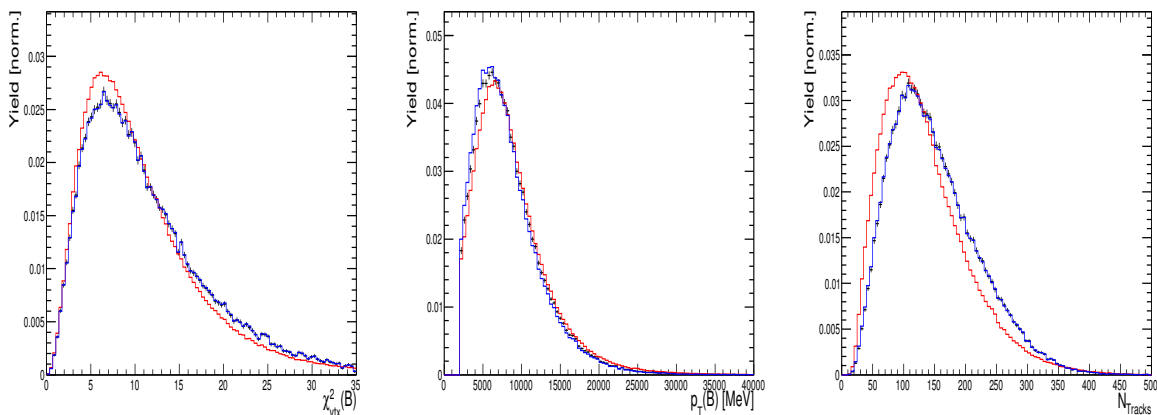
Figure 6.4: Comparison of data (black) and MC simulated events before (red) and after applying all corrections (blue). The histograms are normalized to unity.
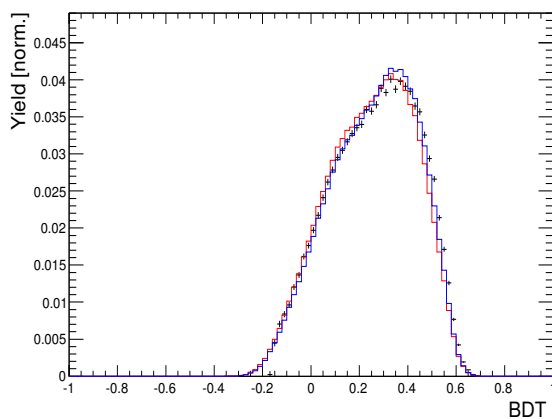
Figure 6.5: Comparison of the BDT response between data (black) and MC simulated events before (red) and after applying all corrections (blue). The histograms are normalized to unity.

6.2 Determination of the phase space acceptance

In principle, the phase space acceptance can be obtained by dividing the phase space into seven-dimensional hyper cubes ("bins"). The local selection efficiency is then given by the ratio of selected to generated events in the respective bin. In the limit of infinitesimal bin hyper volumes, such that the efficiency can be considered as flat within each bin, the phase space acceptance function is reproduced exactly. However, the finite MC statistics limits the accuracy of this method. Due to the non uniformity of the phase space, an uniform binning is not appropriate. For example, an uniform binning with ten bins per dimension would lead to total bin number of 10^7, where most of them are empty or sparsely populated. In that case, the efficiency would not be reliable. To ensure enough statistics in each bin, an adaptive binning scheme, introduced in Sec. 6.2.1, is applied. Section 6.2.2 explains how the efficiency can be naturally included in the normalization of the likelihood function, without explicitly modeling it.

6.2.1 Adaptive binning

The adaptive binning strategy, previously used in Ref. [62], ensures a minimum number of events per bin, henceforth denoted as N_{min}. The algorithm starts with a single bin containing the whole phase space. As a next step, this bin is split into two approximately equally populated bins in a randomly chosen dimension. Each of the resulting bins is repeatedly split until the event count within the bin falls below $2\,N_{min}$. Finally, each bin contains, by construction, between N_{min} and $2\,N_{min}$ events. This procedure is illustrated in Fig. 6.6 for the 2D case and Fig. 6.7 compares the adaptive binning to an uniform binning. The adaptive binning results in fine binning in regions of high event density and
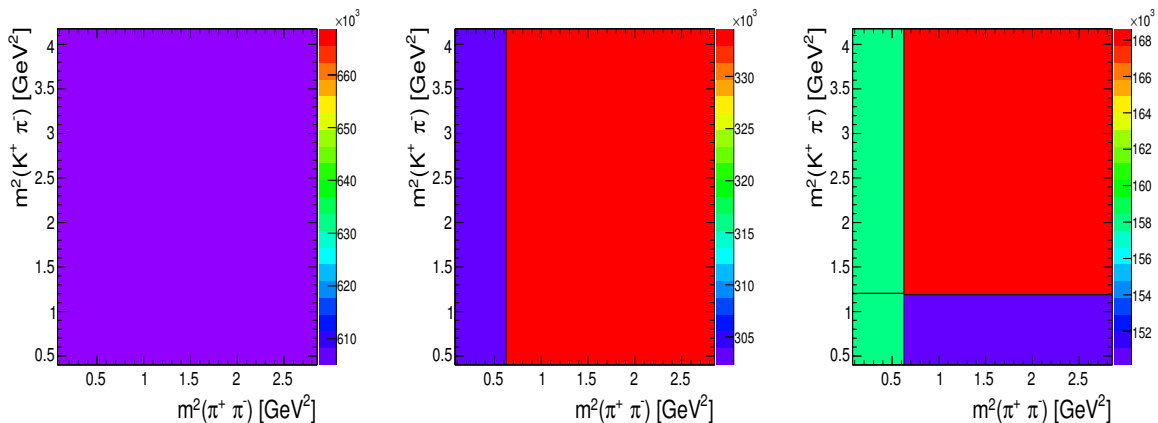
Figure 6.6: Illustration of the adaptive binning applied in the two dimensions drawn. The initial phase space bin (left plot) is split in two bins in a random dimension such that each bin contains an equal number of events (middle plot). Each bin is split again resulting in four bins (right plot). This procedure continues until each bin contains less than twice the minimum required events.
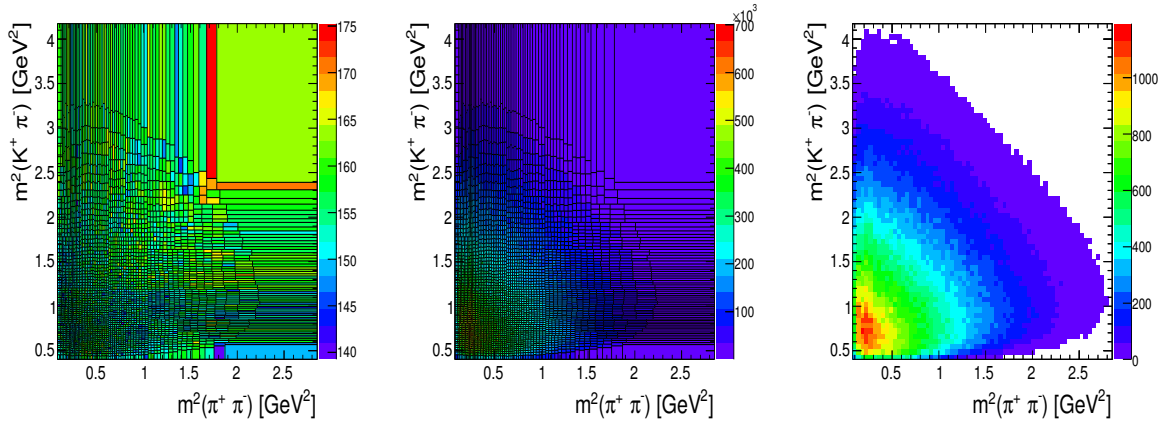
Figure 6.7: Final adaptive binning applied in the two dimensions drawn (left). Each bin contains between N_{min} and $2N_{min}$ events. The bin density, *i.e.* the bin content divided by the bin area, is shown in the middle plot in comparison to an uniform binning on the right plot.

coarse binning in sparsely populated areas. To reduce the dimensionality, it is assumed that the efficiency approximately factorizes as:

$$\epsilon(X) = \epsilon(D) \cdot \epsilon(\Omega) \tag{6.5}$$

where $D = (m^2(K^+\pi^+\pi^-), m^2(K^+\pi^-), m^2(\pi^+\pi^-), m^2(J/\psi\,\pi^+\pi^-), m^2(J/\psi\,\pi^+))$ and $\Omega = (\cos\theta, \chi)$. The efficiency variation over the Dalitz plane, $\epsilon(D)$, is obtained by applying an adaptive binning, in terms of the five invariant mass squared combinations D, based on $584\,796$ $B^+ \to J/\psi\,K^+\pi^+\pi^-$ phase space MC events that pass the final selection. Thereby, at least $N_{min} = 50$ events are required per bin resulting in $9\,096$ bins in total. The same binning scheme is then applied to two million $B^+ \to J/\psi\,K^+\pi^+\pi^-$ phase space MC events at generator level such that the ratio of the bin counts, *cf.* Eq. 6.2, yields the efficiency with an arbitrary scale. Similarly, the angular part of the efficiency, $\epsilon(\Omega)$, is obtained from an uniform 20×40 binning in $\cos\theta$ and χ.

The one-dimensional efficiencies as function of the phase space variables are shown in Fig. 6.8 superimposed by the projections of the efficiency obtained from the multi-dimensional binning. The latter are obtained by dividing the efficiency weighted generator level phase space distribution by the unweighted one. A rather flat efficiency is observed in the central region of the Dalitz plane whereas the efficiency drops down close to the corners. Since the corners of the Dalitz plane are populated with events in which at least one of the final particles has very low momentum, the efficiency is necessarily lower as a consequence of the minimum p_T requirements. Due to the limited statistics, the adaptive binning is not able to resolve the rapid change in efficiency at the boundaries of phase space. One solution would be to exclude the regions near the Dalitz plot boundaries which is, however, a non-trivial task given the complexity of the five-dimensional boundary. Furthermore, the small discrepancy in the $\cos\theta$ projection indicates that there is, contrary to the assumption, a correlation between $\epsilon(D)$ and $\epsilon(\Omega)$. Appendix C presents an alternative,

unbinned approach, in which the Dalitz plot acceptance is expanded in terms of chebyshev polynomials.
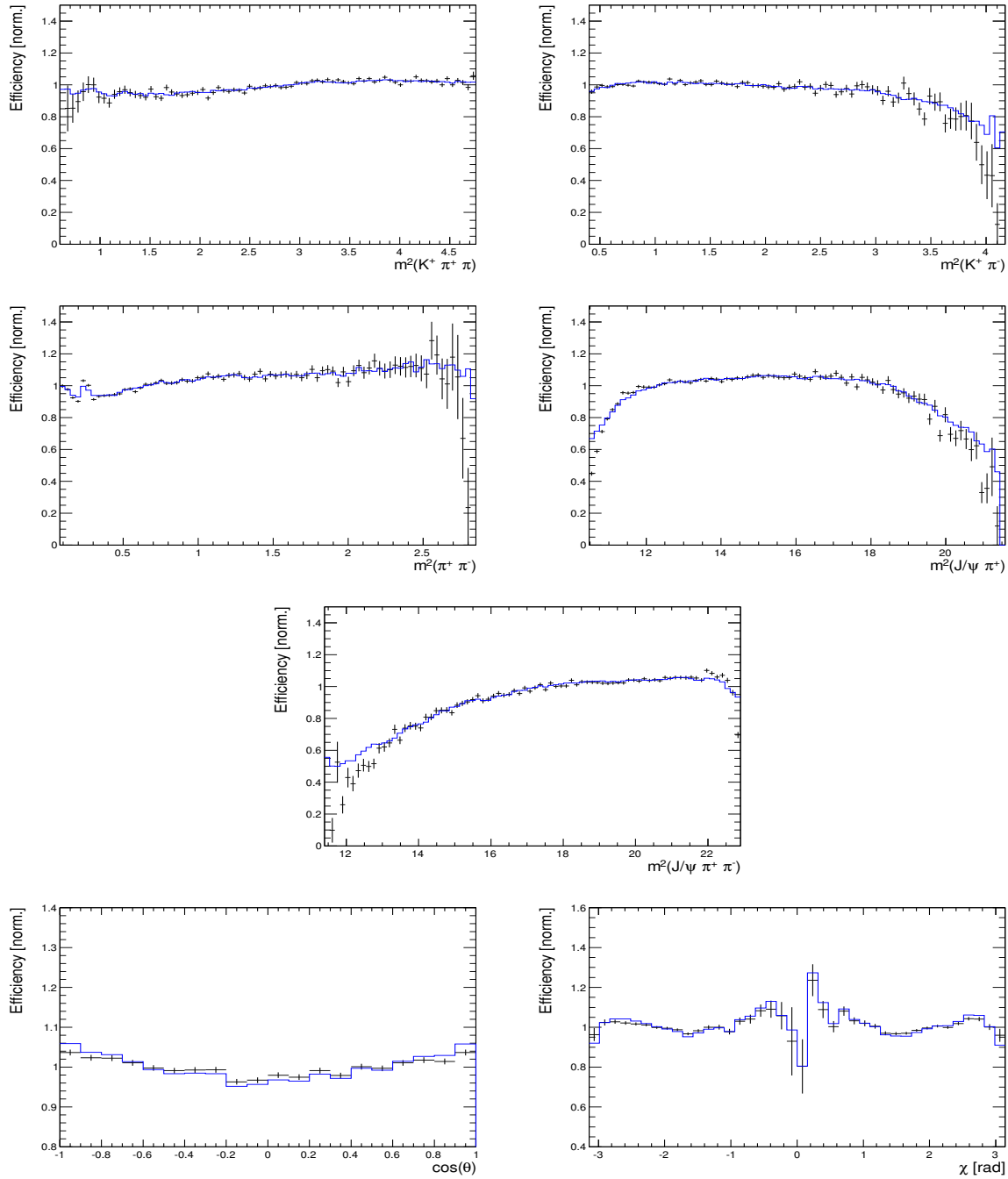
Figure 6.8: One-dimensional efficiencies (black) and projections of the efficiency obtained from the multi-dimensional binning (blue) as a function of the phase space variables. The normalization corresponds to an average efficiency of unity.

6.2.2 MC integration

As the previous subsection has shown, it is not desirable to require a binning nor is it desirable to parameterize the acceptance function, *cf.* Appendix C. For this reason, a different method is applied. Consider the logarithmic likelihood function constructed from the efficiency corrected PDF in Eq. 2.1:

$$\ln L(a) = \ln\left(\frac{\epsilon(X)\,|M(X|a)|^2\,\phi_4(X)}{\int \epsilon(X)\,|M(X|a)|^2\,\phi_4(X)\,\mathrm{d}X}\right) \tag{6.6}$$

$$= \ln \epsilon(X) + \ln|M(X|a)|^2 + \ln \phi_4(X) - \ln \int \epsilon(X)\,|M(X|a)|^2\,\phi_4(X)\,\mathrm{d}X\,. \tag{6.7}$$

The first and third term in Eq. 6.7 are independent on the amplitude model parameters, a, and therefore do not affect the minimum of $\ln L(a)$. They rather add a mere constant to the logarithmic likelihood function such that they can be dropped. However, the acceptance function still enters via the normalization integral, *i.e.* the last term in Eq. 6.7. This normalization term is determined numerically by making use of the MC integration technique. First, pure phase space MC events are generated according to the flat distribution

$$\mathcal{P}_{gen}(X) = \frac{\phi_4(X)}{\int \phi_4(X)\,\mathrm{d}X}\,. \tag{6.8}$$

Using this MC sample, the normalization integral can be approximated by

$$\int \epsilon(X)\,|M(X|a)|^2\,\phi_4(X)\,\mathrm{d}X \approx \frac{V}{N_{gen}}\sum_k^{N_{gen}} \epsilon(X_k)\,|M(X_k|a)|^2 \tag{6.9}$$

where $V = \int \mathrm{d}X$ is the phase space volume, X_k is the k-th event of the MC sample and N_{gen} is the number of generated events. However, this still requires an analytic form of $\epsilon(X)$. The acceptance can be incorporated in the normalization by passing phase space MC events through the full LHCb detector simulation and applying all selection requirements as described in Sec. 5. In doing so, the efficiency is inherently included in these events, *i.e.* the event-to-event efficiency is $\epsilon(X_k) = 1$ for selected events and $\epsilon(X_k) = 0$ for events that have not passed the selection, so that they can be interpreted as being generated according to the PDF

$$\mathcal{P}_{sel}(X) = \frac{\epsilon(X)\,\phi_4(X)}{\int \epsilon(X)\,\phi_4(X)\,\mathrm{d}X}\,. \tag{6.10}$$

The normalization integral can thus be determined, without explicitly modeling of $\epsilon(X)$, by summing over the selected events:

$$\int \epsilon(X)\,|M(X|a)|^2\,\phi_4(X)\,\mathrm{d}X \approx \frac{V}{N_{sel}}\sum_k^{N_{sel}} |M(X_k|a)|^2 \tag{6.11}$$

where N_{sel} is the number of selected events [37]. In fact, this is the only exact efficiency correction method in seven dimensions (in the limit of $N_{sel} \to \infty$) and is therefore used in the following.

7 Momentum resolution

Due to the finite momentum resolution of the detector, the reconstructed Dalitz plot location of an event is, in general, displaced from the true location. This affects the Dalitz plot in two ways: first, events close to the boundaries might be reconstructed in kinematically forbidden phase space regions so that the Dalitz plot boundaries are smeared out. Furthermore, resonance widths are widened which leads to line shapes deviating from their theoretical expectation, *cf.* Sec. 2.1. To quantify the impact on the invariant mass distributions, the residuals

$$\Delta m = m_{true} - m_{reco} \tag{7.1}$$

are studied by making use of simulated MC events, where m_{true} is the true invariant mass and m_{reco} the reconstructed one. It is expected that the residual distribution is approximately Gaussian with mean zero whereby the width of the distribution gives a measure of the resolution.

To improve the mass resolution, a global kinematic fit of the decay tree is performed which recomputes the final state momenta by taking into account four-momentum conservation at each vertex and constraining the B^+ and J/ψ masses to their PDG masses [31]. The **d**ecay **t**ree **f**it (DTF [63]) additionally constrains the B^+ candidate to originate from the primary vertex. As can be seen from the residual distribution of $m(K^+\pi^+\pi^-)$ in Fig. 7.1 (left) and $m(J/\psi \, \pi^+\pi^-)$ in Fig. 7.1 (right), the DTF significantly improves the mass resolution. This applies in particular to invariant mass combinations involving the J/ψ momentum due to the J/ψ mass constraint. Table 7.1 lists the RMS values of the residual distributions before and after applying the DTF.[19]
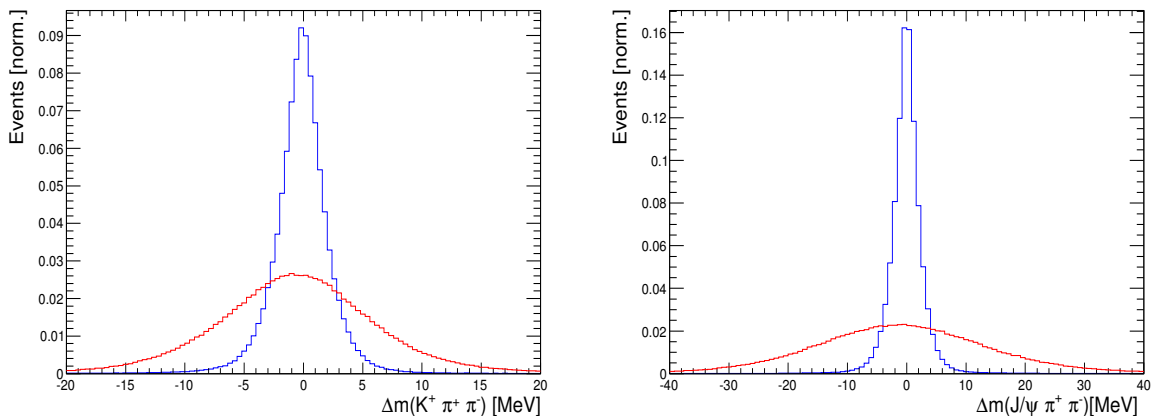
Figure 7.1: Residual distribution of $m(K^+\pi^+\pi^-)$ (left) and $m(J/\psi \, \pi^+\pi^-)$ (right) obtained from reconstructed momenta (red) and refitted momenta (blue). Note the different x-axis limits.

---

[19]The root mean square of a histogram with N bins is defined as $RMS = \sqrt{\frac{1}{N}\sum_i^N (n_i - \overline{n})^2}$ where n_i are the bin counts and $\overline{n}$ is the mean value.

Table 7.1: RMS values of the residual distributions obtained from reconstructed momenta and refitted momenta.

	RMS (no DTF)	RMS (with DTF)
$m(K^+\pi^+\pi^-)$	6.6 MeV	2.6 MeV
$m(K^+\pi^-)$	4.6 MeV	2.4 MeV
$m(\pi^+\pi^-)$	5.1 MeV	2.5 MeV
$m(J/\psi\,\pi^+\pi^-)$	14.4 MeV	3.4 MeV
$m(J/\psi\,\pi^+)$	13.7 MeV	3.3 MeV

The $m^2(J/\psi\,\pi\pi)$ MC distribution is shown in Fig. 7.2 (left) using true, reconstructed and refitted momenta. In general, the impact of the resolution is very small, except for the boundaries, where the smearing can clearly be seen when using reconstructed momenta while the DTF forces the Dalitz plot boundaries to be strictly respected. Furthermore, the mass resolution is negligible in comparison to the widths of the expected resonant structures, for example the decay width of the $K^*(892)$ meson is much larger than the corresponding invariant mass resolution [31]:

$$\Gamma_{K^*(892)} \approx 50\,\text{MeV} \gg \text{RMS}\left(m(K^+\pi^-)\right) = 2.4\,\text{MeV}. \tag{7.2}$$

There is one exception, namely the $\psi(2S)$ meson whose decay width is much smaller than the mass resolution [31]:

$$\Gamma_{\psi(2S)} \approx 0.3\,\text{MeV} \ll \text{RMS}\left(m(J/\psi\,\pi\pi)\right) = 3.4\,\text{MeV}. \tag{7.3}$$

Figure 7.2 (right) illustrates the impact of the resolution on the $\psi(2S)$ line shape by comparing the $m^2(J/\psi\,\pi\pi)$ distribution in data before and after applying the DTF. One approach to model the resolution effect on the $\psi(2S)$ line shape is to convolute the signal PDF with a resolution function which converts the true invariant masses to their reconstructed values. However, it would be difficult to parameterize the multi-dimensional resolution function and the numerical evaluation of the convolution would be prohibitively CPU intensive. Another option is to use an effective width of the $\psi(2S)$ meson which is in the order of the mass resolution as input for the corresponding line shape when performing the amplitude fit. As the main interest of this analysis resides in the study of the $K^+\pi^+\pi^-$ resonance structure and the $\psi(2S)$ resonance is well isolated from other resonant structures, it is, however, decided to veto events consistent with $B^+ \to (\psi(2S) \to J/\psi\,\pi^+\pi^-)K^+$ decays by requiring $m^2(J/\psi\,\pi\pi) > 14\,\text{GeV}^2$. In doing so, resolution can be safely neglected in the amplitude fit since the remaining resonant structures are sufficiently broad and a cleaner environment for the $K^+\pi^+\pi^-$ system is provided. This, additionally, ensures comparability to the BELLE analysis of $B^+ \to J/\psi\,K^+\pi^+\pi^-$ decays, in which $B^+ \to \psi(2S)K^+$ decays were also vetoed. As a consequence, the data sample size is reduced from 129 511 to 109 995 signal events.
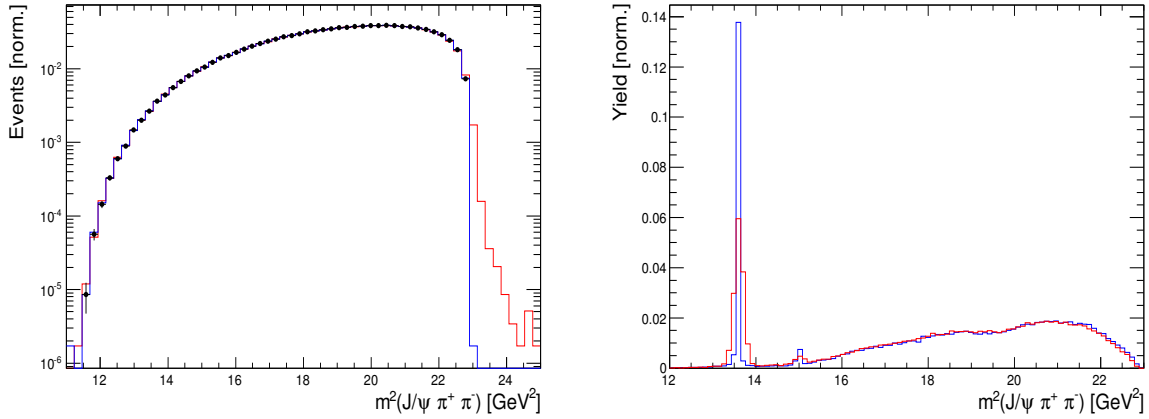
Figure 7.2: Invariant mass distribution of the $J/\psi\ \pi^+\ \pi^-$ system for phase space MC events (left) and *sWeighted* data (right). Histograms obtained using reconstructed (refitted) momenta are shown in red (blue). In addition, the left plot contains the true distribution (black).

Besides improving the mass resolution, the DTF resolves an additional problem which becomes evident when looking at Fig. 7.3. The kinematic limit of *e.g.* $m^2(K^+\pi^+\pi^-)$ depends on the reconstructed B^+ mass or rather the available phase space scales with $m(J/\psi K^+\pi^+\pi^-)$. This introduces a correlation between the invariant mass combinations and the reconstructed B^+ mass. Since the kinematically allowed region is different for signal and sideband region events as demonstrated in Fig. 7.4 (left), the sideband events cannot safely be used to interpolate the expected phase space distribution of the background events inside the signal region. After constraining the momenta to the nominal B^+ mass, the correlation is removed and the limits of signal and sideband distributions match as shown in Fig. 7.4 (right). Consequently, the refitted momenta are passed to the amplitude fit described in Chapter 8.
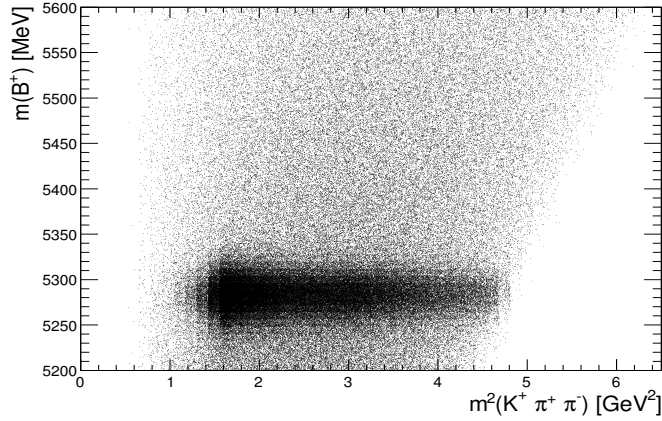
Figure 7.3: Scatter plot of $m(J/\psi K^+\pi^+\pi^-)$ versus $m^2(K^+\pi^+\pi^-)$. The kinematic limit of $m^2(K^+\pi^+\pi^-)$ depends on the reconstructed B^+ mass.
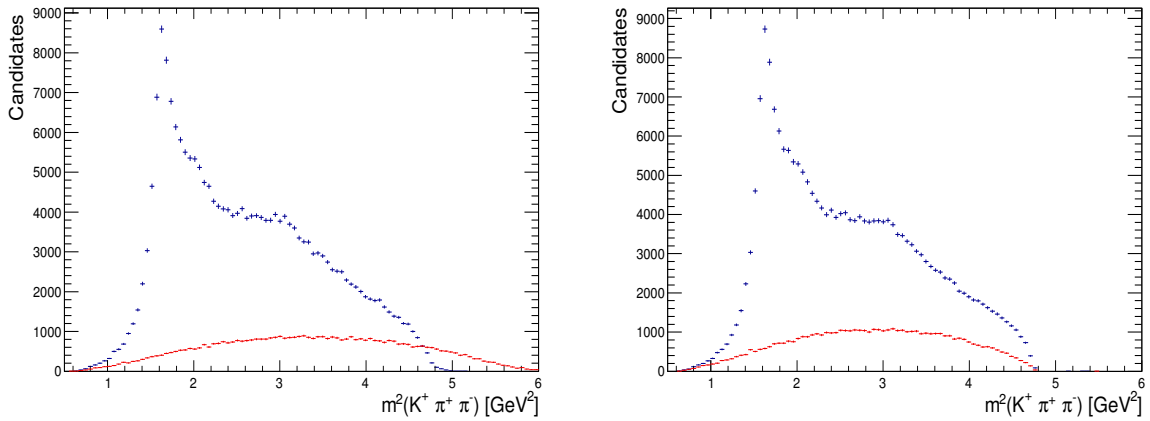
Figure 7.4: Invariant mass distribution of the $K^+\pi^+\pi^-$ system for signal region (blue) and sideband region (red) data events that pass the preselection. The sideband distribution is normalized to the expected number of background events inside the signal region. Signal and sideband distributions have different maxima in $m^2(K^+\pi^+\pi^-)$ when using reconstructed momenta (left) while the endpoints coincide when using refitted momenta (right).

64

8 Amplitude Fit

The results of the amplitude analysis of $B^+ \to J/\psi\, K^+\pi^+\pi^-$ decays are presented in this Chapter. In order to determine the amplitude couplings a_i, an unbinned maximum likelihood fit to the data events, that have passed the final selection, described in Chap. 5, and the $\psi(2S)$ veto, is performed using MINT, *cf.* Sec. 2.3, based on the signal PDF

$$\mathcal{P}(X|a) = \frac{\varepsilon(X)\,\left|\sum_i a_i\, \mathcal{A}_i(X)\right|^2\, \phi_4(X)}{\int \varepsilon(X)\,\left|\sum_i a_i\, \mathcal{A}_i(X)\right|^2\, \phi_4(X)\, \mathrm{d}X}\ . \tag{8.1}$$

The background is statistically subtracted by applying *sWeights* as described in Sec. 4.2.[20] To account for the variation in efficiency, the MC (likelihood) normalization method presented in Sec. 6.2.2 is used. The mass and width of resonances are fixed to their world average values, see Appendix D. However, it is *a priori* unknown which decay channels (or amplitudes $\mathcal{A}_i(X)$) actually contribute to the decay $B^+ \to J/\psi\, K^+\pi^+\pi^-$. Therefore, multiple configurations are tested. The resonance contributions included in the Belle analysis, *cf.* Table 1.2, are used as starting point.

8.1 Belle model

The data provides first indication for the most evident resonances present. Inspection of the invariant mass projections in Figs. 8.1 and 8.2 reveals clear evidence for $K_1(1270)^+ \to K^+\pi^+\pi^-$, $K_1(1400)^+ \to K^+\pi^+\pi^-$, $K^*(892) \to K^+\pi^-$ and $\rho(770) \to \pi^+\pi^-$ contributions. Furthermore, there is indication of smaller contributions from intermediate $K_2(1770)^+ \to K^+\pi^+\pi^-$, $K_2^*(1430) \to K^+\pi^-$, $f_0(980) \to \pi^+\pi^-$ and $f_2(1270) \to \pi^+\pi^-$. The Belle model includes these resonances in several decay modes in addition to $K^*(1410)^+, K_2^*(1430)^+, K_2(1580)^+, K_2^*(1980)^+ \to K^+\pi^+\pi^-$ and $\omega \to \pi^+\pi^-$ contributions. Moreover, the Belle model includes a constant non resonant amplitude with coupling constant a_{NR} added incoherently to the resonant intermediate state amplitudes:

$$|\mathcal{M}_{Belle}(X)|^2 = |a_{NR}|^2 + \left|\sum_i a_i\, \mathcal{A}_i(X)\right|^2\ . \tag{8.2}$$

One of the couplings a_i can be fixed to unity due to the overall normalization and the fact that only phase differences contain physical information.

Table 8.1 lists the magnitudes and phases of the complex couplings a obtained by fitting the Belle model to the data, along with the corresponding decay fractions. The latter are calculated from Eq. 1.9 using the fitted PDF. For this purpose, the occurring phase space integrals are evaluated by utilizing the MC integration technique just as in the likelihood normalization. Note that the decay fraction of an intermediate state amplitude $\mathcal{A}_i$ does not only depend on its respective coupling a_i, but on the whole set of couplings a through the normalization.

---

[20]The *sWeights* are calculated based on the fit to reconstructed B^+ mass after the final selection, *cf.* Sec. 5.4.

Table 8.1: Magnitudes and phases of the complex couplings and fractional contributions for each component of the Belle model. Only the statistical uncertainties are given.

Decay mode	$|a_i|$	ϕ_i [degrees]	Fraction F_i [%]
$B \to J/\psi\, [K_1(1270) \to K^*(892)\,\pi]$	1 (fixed)	0 (fixed)	8.18 ± 0.18
$B \to J/\psi\, [K_1(1270) \to K\,\rho(770)]$	1.89 ± 0.03	93.1 ± 1.2	29.08 ± 0.42
$B \to J/\psi\, [K_1(1270) \to K\,\omega(782)]$	0.0753 ± 0.0042	88.1 ± 1.6	0.27 ± 0.03
$B \to J/\psi\, [K_1(1270) \to K_0^*(1430)\,\pi]$	4.69 ± 0.12	92.1 ± 1.3	3.89 ± 0.23
$B \to J/\psi\, [K_1(1400) \to K^*(892)\,\pi]$	0.656 ± 0.035	91.0 ± 1.4	1.70 ± 0.20
$B \to J/\psi\, [K^*(1410) \to K^*(892)\,\pi]$	0.561 ± 0.009	192.1 ± 1.0	10.14 ± 0.21
$B \to J/\psi\, [K_2^*(1430) \to K^*(892)\,\pi]$	0.177 ± 0.032	263.9 ± 1.7	0.109 ± 0.039
$B \to J/\psi\, [K_2^*(1430) \to K\,\rho(770)]$	0.108 ± 0.026	80.0 ± 1.2	0.053 ± 0.026
$B \to J/\psi\, [K_2(1580) \to K^*(892)\,\pi]$	0.265 ± 0.015	296.8 ± 1.5	0.740 ± 0.081
$B \to J/\psi\, [K_2(1580) \to K\,\rho(770)]$	0.286 ± 0.010	275.9 ± 1.4	1.438 ± 0.097
$B \to J/\psi\, [K_2(1770) \to K^*(892)\,\pi]$	0.619 ± 0.024	271.2 ± 1.4	1.82 ± 0.14
$B \to J/\psi\, [K_2(1770) \to K_2^*(1430)\,\pi]$	0.0141 ± 0.0158	86.7 ± 2.1	0.001 ± 0.003
$B \to J/\psi\, [K_2(1770) \to K\,f_0(980)]$	0.0338 ± 0.0186	66.4 ± 1.6	0.005 ± 0.006
$B \to J/\psi\, [K_2(1770) \to K\,f_2(1270)]$	0.448 ± 0.031	30.3 ± 0.9	0.265 ± 0.039
$B \to J/\psi\, [K_2^*(1980) \to K^*(892)\,\pi]$	0.0857 ± 0.0224	90.3 ± 1.2	0.047 ± 0.025
$B \to J/\psi\, [K_2^*(1980) \to K\,\rho(770)]$	0.0966 ± 0.0218	256.0 ± 1.3	0.132 ± 0.056
$B \to J/\psi\,K\pi\pi$ (non resonant)	19.3 ± 0.3	0 (fixed)	39.31 ± 0.43

In order to quantify the quality of the fit including the correlation of the phase space variables, a χ^2 value is determined by binning the data in phase space as

$$\chi_{7D}^2 = \sum_{b=1}^{N_{bins}} \frac{[N_b - N_b^{exp}(a)]^2}{N_b^{exp}(a)} \tag{8.3}$$

where N_b is the number of signal (data) events in a given bin,[21] $N_b^{exp}(a)$ is the event count predicted by the fitted PDF and N_{bins} is the number of bins [37]. The adaptive binning, introduced in Sec. 6.2.1, is used to ensure sufficient statistics in each bin for a robust χ^2 calculation. At least 30 events per bin are required. The expected event count is obtained by weighting the selected phase space MC events by the fitted amplitude, $|\sum_i a_i \mathcal{A}_i(X)|^2$. The sum of these weights is then normalized to yield the number of observed signal events. To access the fit quality in the Dalitz plot variables alone, an additional χ^2 value in five-dimensional Dalitz plot bins is calculated, χ_{5D}^2. The reduced dimensionality allows to resolve finer structures.

Ideally, the χ^2 value divided by the number of degrees of freedom, given by $\nu = (N_{bins} - 1) - N_{par}$, where N_{par} is the number of free fit parameters, should be close to unity.[22] The reduced phase space and Dalitz plot χ^2 values are $\chi_{7D}^2/\nu_{7D} = 4.2$

---

[21]The signal count in a given bin is equal to the sum of $sWeights$ for all events in that bin.

[22] The number of bins is reduced by one due to the overall normalization.

and $\chi^2_{5D}/\nu_{5D} = 4.8$, respectively, indicating a poor fit quality as obvious from the fit projections superimposed on the data in Figs. 8.1 and 8.2.

However, it is not too surprising that a model working fine in three dimensions can not easily be translated to the seven-dimensional case. Consider, for example, the decay chains $K_1(1400) \to K^*(892)\,\pi^+$ and $K^*(1410) \to K^*(892)\,\pi^+$. The masses of the $K_1(1400)$ and $K^*(1410)$ mesons are consistent within their errors and also the widths are very similar (agreement within three standard deviations), see Appendix D. Now, the Breit-Wigner terms in both amplitudes constrain the phase space to a (narrow) slice in $m^2(K^+\pi^+\pi^-)$, $m^2(K^+\pi^-)$ and apparently also in $m^2(\pi^+\pi^-)$ due to the correlation. Therefore, replacing one of the amplitudes by the other has a minor impact on these three invariant mass projections, while the reflections in the remaining four dimensions differ significantly due to the opposite parity of the $K_1(1400)$ and $K^*(1410)$ mesons. The same applies to different angular momentum couplings, as already noticed in Sec. 2.3. Consequently, the increased sensitivity in full phase space dramatically complicates the model finding.

Nonetheless, important conclusions for further iterations can be drawn from the fit result. First of all, the non resonant contribution with a fit fraction of almost 40% is far too high judging from the fit projections. Its omnipresence in phase space leads to very small fit fractions for the high-mass "kaon" (*i.e.* exited $u\bar{s}$ states) resonances. As discussed in Sec. 2.2.5, a constant non resonant amplitude violates angular momentum conservation and is therefore, indeed, unphysical. It should hence be replaced by at least one non resonant amplitude with angular momentum among the final state particles. Furthermore, non resonant decays should interfere with other decay channels as well. Therefore, non resonant amplitudes are added coherently rather than incoherently to the resonant contributions in the following. The largest discrepancies between data and fit are visible at the $m^2(J/\psi\,\pi^+)$ and $\cos\theta$ projections. Although the fit predicts clearly less $\rho(770) \to \pi^+\pi^-$ contributions than actually observed, the decay fraction for $K_1(1270) \to K^+\,\rho(770)$ seems too high since this contribution accumulates at low $m^2(J/\psi\,\pi^+)$ values as can be seen from Fig. 8.2. This suggests to include additional decay modes involving the $\rho(770)$ meson, such as $K^*(1400) \to K^+\,\rho(770)$, or higher angular momentum couplings, such as P- or D-wave decays of $B^+ \to J/\psi\,K_1(1270)$. The latter is confirmed by comparing the $\cos\theta$ distribution in Fig. 8.2 to the S- and P-wave MC distribution in Fig. 2.4. Finally, a small contribution from $X(3872) \to J/\psi\,\pi^+\pi^-$ decays can be identified in Fig. 2.3. Further resonances decaying to $J/\psi\,\pi^+\pi^-$ or $J/\psi\,\pi^+$ are conceivable but not immediately obvious given the complicated phase space structure.
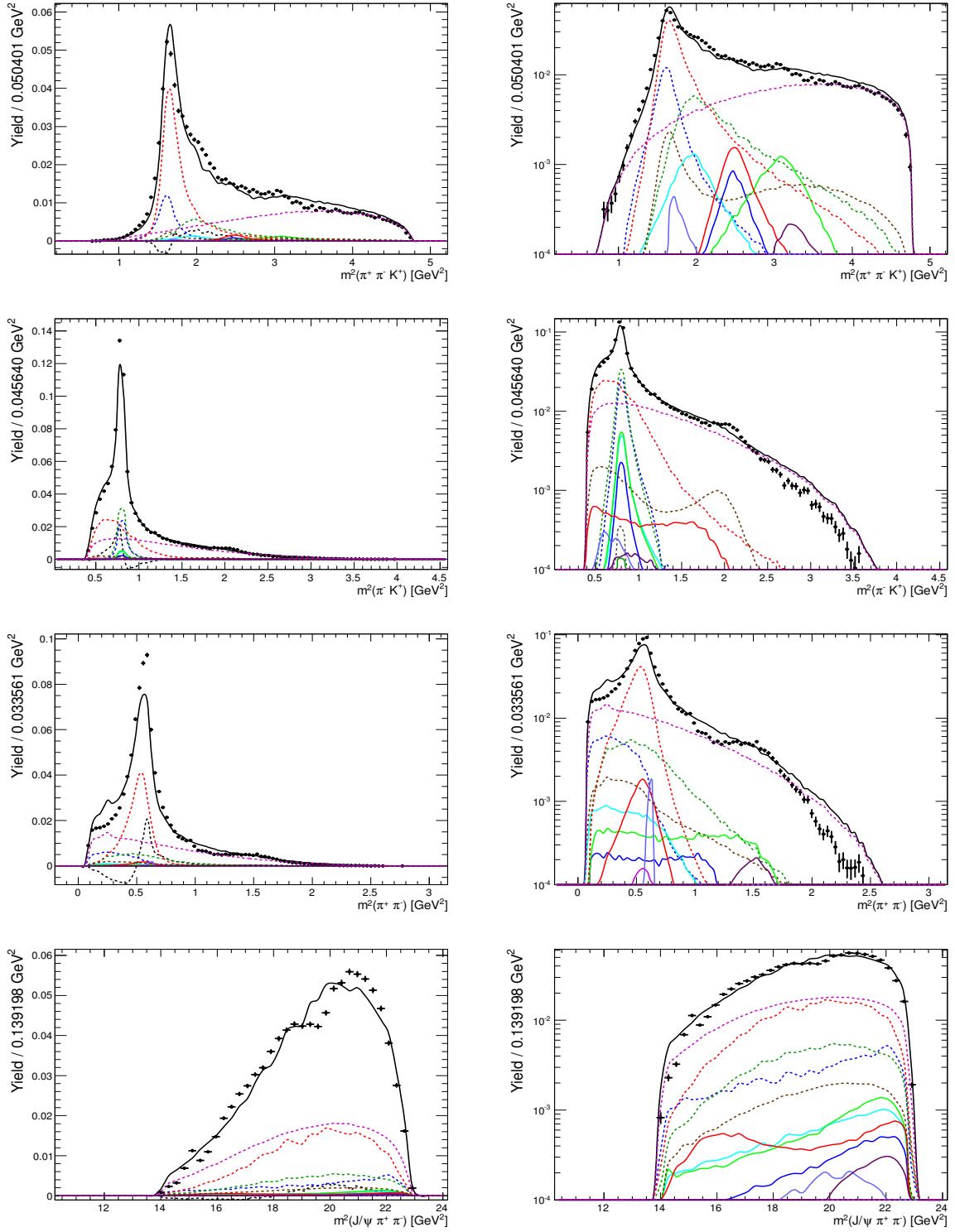
Figure 8.1: Distributions of the phase space observables for data (points with error bars) and fit projections based on the Belle model (black solid line). The individual amplitude contributions are color-coded as in the legend in Fig. 8.2.
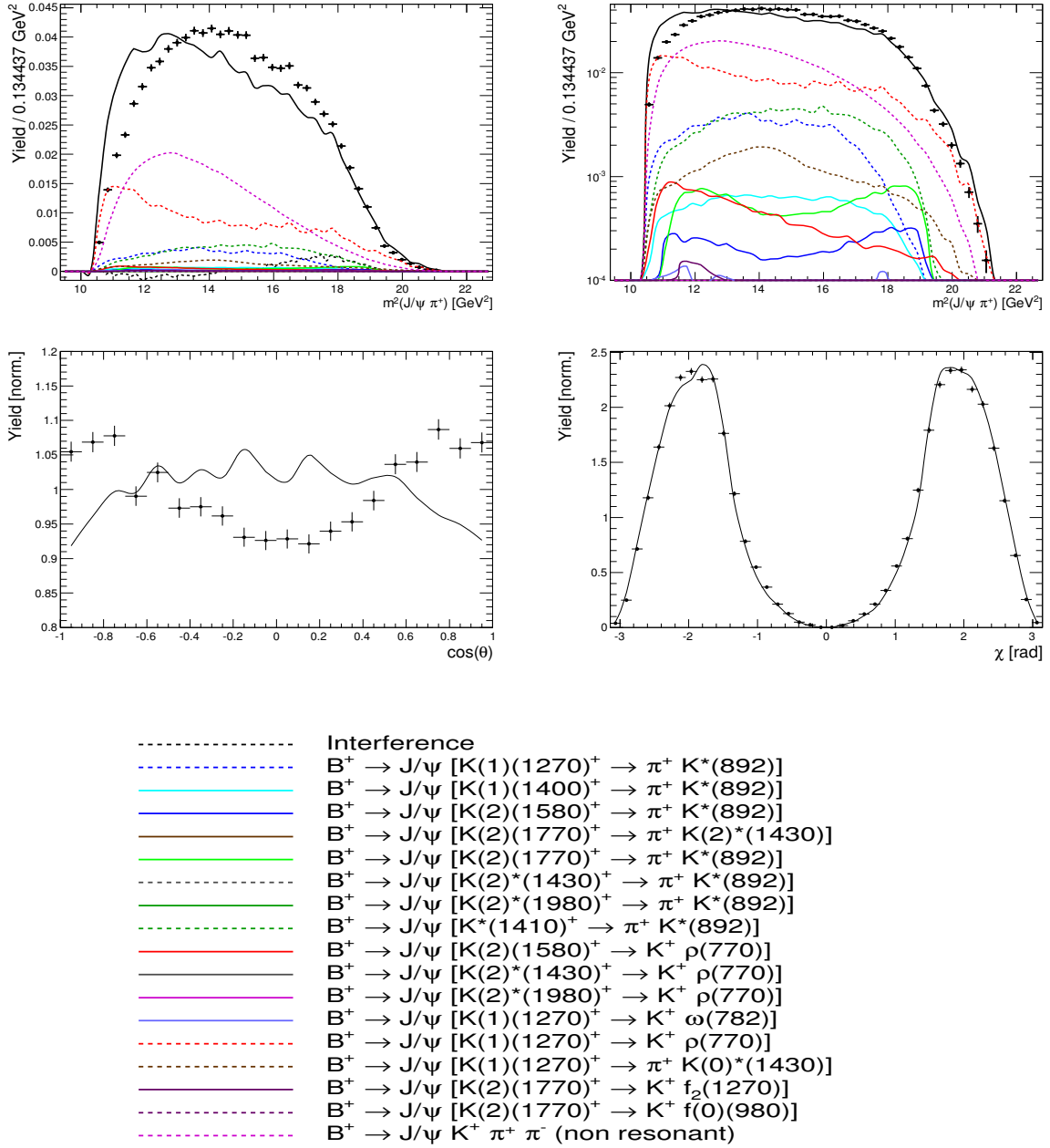
Figure 8.2: Distributions of the phase space observables for data (points with error bars) and fit projections based on the Belle model (black solid line). The individual amplitude contributions are color-coded as in the legend.

8.2 Baseline model

Based on the results of the previous section, a better resonance model is searched iteratively. First, the unphysical, constant non resonant amplitude is removed. Amplitudes are then successively added until a reasonable agreement between data and fit is achieved. The list of amplitudes implemented in MINT for this purpose is given in Appendix E. Besides additional decay channels of the already considered resonances decaying to $K^+\pi^+\pi^-$, contributions from $K^*(1680)^+$, $K_2(1820)^+$, $K_2(2250)^+ \to K^+\pi^+\pi^-$ are taken into account. Several charmonium(-like) resonances decaying to $J/\psi\,\pi^+\pi^-$ ($X(3872)$, $\psi(4040)$, $\psi(4160)$, $X(4260)$, $\psi(4415)$) or $J/\psi\,\pi^+$ ($Z(3900)$, $Z(4240)$, $Z(4430)$) are additionally considered. Moreover, single resonance amplitudes for the prominent resonances $K_1(1270)$, $K^*(892)$ and $\rho(770)$ as well as 25 non resonant amplitudes are implemented summing up to 96 amplitudes in total. Of course, this list makes no claims of being complete. Higher orbital angular momentum couplings are, for example, not considered except for the dominant decay channel $B^+ \to J/\psi\,K_1(1270)$.

This overwhelming abundance of amplitudes should clarify that the resonance model is necessary incomplete and there is nothing like the one and only "true" model. A further complication arises from the limited computing power. Due to the high statistics data sample and the complicated PDF, the likelihood fits are very time consuming. A fit with 20 amplitudes takes approximately four days on a single 2.8 GHz processor, where the required time scales with the number of amplitudes included. The likelihood fit also gets unstable when dealing with to many free parameters, where each added amplitude contributes two of them. Therefore, amplitudes with decay fractions smaller than 3% are (at least temporarily) removed from the model. As even contributions with tiny decay fractions can have a significant impact on the phase space distribution due to interference effects, amplitudes are added again if their removal significantly worsens the fit result judging from the χ^2 values and the fit projections.

More than 300 configurations are tested. The fitted parameters for the "best" model, in terms of the χ^2 values which yield $\chi^2_{7D}/\nu_{7D} = 2.1$ and $\chi^2_{5D}/\nu_{5D} = 2.4$, are listed in Table 8.2, while the fit projections are shown in Figs. 8.3 and 8.4. Reasonable agreement is observed between the fit and the data for most distributions. Exceptions are the $m^2(J/\psi\,\pi^+\pi^-)$ and $m^2(J/\psi\,\pi^+)$ projections. However, both are considerably improved with respect to the Belle model. The same applies, in particular, to the $\cos\theta$ distribution.

The main differences from the Belle model are the following: firstly, a significant P-wave contribution from the decay mode $B^+ \to J/\psi\,K_1(1270)$ with both $K_1(1270) \to K^+\rho(770)$ and $K_1(1270) \to K^*(892)\,\pi^+$ is observed, confirming the suspicion expressed in the previous section. This is clearly one of the main reasons for the improvement in the $\cos\theta$ and $m^2(J/\psi\,\pi^+)$ projections. The (constant) non resonant amplitude from the Belle model is replaced by a combination of two non resonant amplitudes with different angular momentum couplings among the final state particles leading to a more realistic non resonant decay fraction of 8.46% in total. The best model contains, in addition, the decay channels $K_1(1400) \to K^+\rho(770)$ and $K^*(1410) \to K^+\rho(770)$, while contributions from the

70

Table 8.2: Magnitudes and phases of the complex couplings and fractional contributions for each component of the baseline model. Only the statistical uncertainties are given.

Decay mode	$|a_i|$	ϕ_i [degrees]	Fraction F_i [%]
$B \to J/\psi \, [K_1(1270) \to K^*(892)\,\pi]$	0.299 ± 0.007	240.2 ± 1.3	1.90 ± 0.09
$B[P] \to J/\psi \, [K_1(1270) \to K^*(892)\,\pi]$	0.0453 ± 0.0006	205.0 ± 0.9	5.15 ± 0.09
$B \to J/\psi \, [K_1(1270) \to K\,\rho(770)]$	1.0 (fixed)	180 (fixed)	14.09 ± 0.24
$B[P] \to J/\psi \, [K_1(1270) \to K\,\rho(770)]$	0.0701 ± 0.0009	177.2 ± 0.8	12.25 ± 0.18
$B \to J/\psi \, [K_1(1270) \to K_0^*(1430)\,\pi]$	3.757 ± 0.067	274.3 ± 1.1	6.63 ± 0.19
$B \to J/\psi \, [K_1(1270) \to K\,f_0(980)]$	1.383 ± 0.024	297.7 ± 1.4	3.61 ± 0.11
$B \to J/\psi \, [K_1(1400) \to K^*(892)\,\pi]$	0.699 ± 0.012	238.6 ± 1.2	5.03 ± 0.14
$B \to J/\psi \, [K_1(1400) \to K\,\rho(770)]$	0.425 ± 0.010	175.7 ± 1.6	3.13 ± 0.13
$B \to J/\psi \, [K^*(1410) \to K^*(892)\,\pi]$	0.242 ± 0.003	263.5 ± 1.1	5.05 ± 0.11
$B \to J/\psi \, [K^*(1410) \to K\,\rho(770)]$	0.182 ± 0.003	61.2 ± 1.3	3.23 ± 0.12
$B \to J/\psi \, [K_2(1770) \to K^*(892)\,\pi]$	0.519 ± 0.008	326.5 ± 1.3	3.45 ± 0.09
$B \to J/\psi \, [K_2(1770) \to K\,f_2(1270)]$	0.526 ± 0.016	380.8 ± 2.4	0.99 ± 0.06
$B \to J/\psi \, [K_2(2250) \to K\,f_2(1270)]$	0.746 ± 0.058	37.3 ± 3.8	0.53 ± 0.04
$B \to K \, [X(3872) \to J/\psi\,\rho(770)]$	0.0639 ± 0.0015	121.9 ± 3.5	1.02 ± 0.05
$B \to J/\psi \, [K\,\rho(770)]_P$	0.268 ± 0.004	202.0 ± 1.3	8.47 ± 0.15
$B[P] \to \pi^+ \, [J/\psi \, (K\,\pi^-)_S]_S$	1.825 ± 0.034	175.4 ± 1.6	2.04 ± 0.07
$B[P] \to [J/\psi \, \pi^+]_S \, [K\pi^-]_S$	3.831 ± 0.051	363.8 ± 1.3	6.42 ± 0.13

resonances $K_2^*(1430)$ and $K_2^*(1980)$ are not included at all. A possible explanation for the absence of the $J^P = 2^+$ kaon excitations from the model could be that parity conservation forces *e.g.* the decay $K_2^*(1430) \to K^*(892)\,\pi^+$ to proceed in a relative D-wave such that the centrifugal barrier suppresses these decay modes relative to the $J^P = 2^-$ excitation $K_2(1770)$ which can decay in a relative P-wave to $K^*(892)\,\pi^+$. The $\omega(782)$ resonance is not part of the model either. Although the branching fraction for the decay mode $\omega \to \pi^+\pi^-$ ($\mathcal{B}(\omega \to \pi^+\pi^-) = 1.53\%$ [31]) is very small, the Belle amplitude analysis reports a significant impact from the $\omega(782)$ resonance through interference. This interference effect cannot be confirmed. Adding the $K_1(1270) \to K^+ \omega(782)$ amplitude to the best model results in a tiny decay fraction (smaller than 0.1%) and no change in fit quality. In return, amplitudes for the decay chains $K_1(1270) \to K^+ f_0(980)$ and $X(3872) \to J/\psi\,\rho(770)$ as well as a single $\rho(770)$ resonance amplitude are included resulting in decay fractions of 3.61%, 1.02% and 8.47%, respectively. The large fit fraction of the single $\rho(770)$ amplitude may hint to an additional broad kaon excitation that have not yet been considered such as the $K_3^*(1780)$ meson.

The presented model is in no way unique. Many alternative models of similar fit quality are observed, see Appendix F. The non resonant amplitudes might be replaced by another combination of two, three or four non resonant amplitudes without changing the fit result. In the same way, the amplitudes for the decay chains $K^*(1680) \to K^*(892)\,\pi^+$,

$K^*(1680) \to K^+ \rho(770)$ or $K_2(1580) \to K^*(892)\,\pi^+$ could be added resulting in decay fractions in the order of 1% without noticeable impact on the phase space distribution. It should therefore be considered as a baseline model based on which further studies of smaller intermediate resonance components are feasible.

8.3 Discussion of the results

Despite the remarkable improvement of the fit result with regard to the Belle model, there is still obvious disagreement between the fit and the data in some regions of the phase space. In particular, the region around $m^2(J/\psi\,\pi^+\pi^-) \approx 20\,\mathrm{GeV}^2$ is not properly described. The possible reasons are manifold: The mismatch could be due to negative interference at $4.4\,\mathrm{GeV}$ which is not correctly modeled by the PDF or related to the presence of a resonance decaying to $J/\psi\,\pi^+\pi^-$ near $4.3\,\mathrm{GeV}$. A suitable resonance with mass $4251\,\mathrm{MeV}$, called $X(4260)$ meson, was seen by the BABAR collaboration in the decay mode $X(4260) \to J/\psi\,f_0(980)$ [64] as well as by the Belle and the BESIII collaborations in the decay mode $X(4260) \to Z(3900)^{\pm}\pi^{\mp}$ [65, 66]. These decay modes could also explain the enhancements of the data distribution with respect to the fitted PDF near $m^2(\pi^+\pi^-) \approx 0.95\,\mathrm{GeV}^2$, related to the $f_0(980)$ channel, and $m^2(J/\psi\,\pi^+) \approx 15\,\mathrm{GeV}^2$, related to the $Z(3900)$ channel. However, no significant contribution from these decay channels is observed when adding them on top of the baseline model, see Appendix F. This might be caused by the masses and widths of the not yet established $X(4260)$ and $Z(3900)$ mesons, fixed to the PDG [31] values in the fit, being too far from their true values or that the assumed quantum numbers are not correct. On the other hand, the $m^2(J/\psi\,\pi^+\pi^-)$ and $m^2(J/\psi\,\pi^+)$ distributions are very sensible to the present kaon excitations such that the observed structures could also be caused by a reflection of a higher spin state in of the resonances decaying to $K^+\pi^+\pi^-$. Moreover, Figure 8.3 suggest that the (combined) decay fraction of the $K_1(1270)$ meson is slightly too large. This could be explained by a missing decay channel of the $K_1(1270)$ resonance which interferes negatively with the other decay channels or by the fact that the assumed width of the $K_1(1270)$ meson is too narrow. The latter may also be an explanation of the disagreement between data and fit at very low $m^2(K^+\pi^+\pi^-)$ values $(m^2(K^+\pi^+\pi^-) < 1\,\mathrm{GeV}^2)$.

The χ^2 values reported in the previous sections reflect the statistical error of the fit only. However, the precision of Dalitz analyses is commonly systematically limited, see *e.g.* Refs. [13, 19]. Due to the limited time for this thesis, the impact of the systematic error sources on the fit result could not have been investigated. Nevertheless, a brief overview of possible systematic error sources is given in the following. The systematic uncertainties are divided into two main categories: experimental and model-dependent uncertainties.

The experimental systematic uncertainties arise from imperfect background cancelation by applying the *sWeight* technique or unknown peaking background sources. Several uncertainties are related to the modeling of detector effects. The inclusion of the acceptance in the fit relies on simulated data which does not reproduce the real data exactly and is statistically limited. Moreover, the finite momentum resolution is ignored in the fit.

Model-dependent systematic errors include, besides the already discussed unknown resonance composition, the modeling of the spin-dependent angular distributions and line shapes. Where the isobar model ignores rescattering, the line shapes suffer from imprecise knowledge of the mass and width of resonances which are fixed in the fit but have mostly large associated uncertainties, see Appendix D. As an example, the uncertainty on the $K_1(1270)$ width amounts to 8% ($\Gamma_{K_1(1270)} = 87 \pm 7\,\text{MeV}$ [31]). Furthermore, the Blatt-Weisskopf barrier factors contain the meson radius r_{BW} whose value, fixed to $1.5\,\text{GeV}^{-1}$ in the fit, was observed in Ref. [13] to have significant impact on the line shapes.

With all this in mind, the fit result can be considered as reasonably good.

8.4   Limitations of the method

The large amount of possible intermediate resonance components together with the lacking experimental and theoretical knowledge necessitates a more sophisticated model finding algorithm gaining advantage over the naive trial and error approach used in this analysis. A genetic algorithm dedicated to the optimization of amplitude models has recently been proposed in Ref. [67]. However, it is a challenging task to obtain a good fit result in seven dimensions involving many free parameters, even if the contributing resonances would be known. The likelihood parameter space is highly non-trivial such that the fit can easily find a local minimum rather than converging to the true global minimum. This implies that two fits with the same PDF but different starting points for the parameters do not necessarily converge to the same solution which again complicates the model finding. A possible solution to this problem is presented in Ref. [68]. Here, the two software packages Geneva [69] and Minuit [70] are used in combination in order to find the true minimum in likelihood parameter space. Geneva is specialized to detect the rough region of the global minimum, which is then passed to Minuit to find the exact location. Minuit provides a higher precision and more accurate error estimates but is prone to be caught in a local minima. At the moment, only Minuit is used.

A further limitation is imposed by the finite processor speed. In fact, the MINT developer team is currently working on the parallelization of their fitter in order to speed up computing time significantly [71]. To execute the fit on multiple CPUs in parallel would allow to let the mass and width of resonances float as well (at least some of them). In any case, additional experimental input from other measurements is needed, such as more precise masses, widths or branching fractions, in order to achieve an enhanced result of the amplitude analysis.
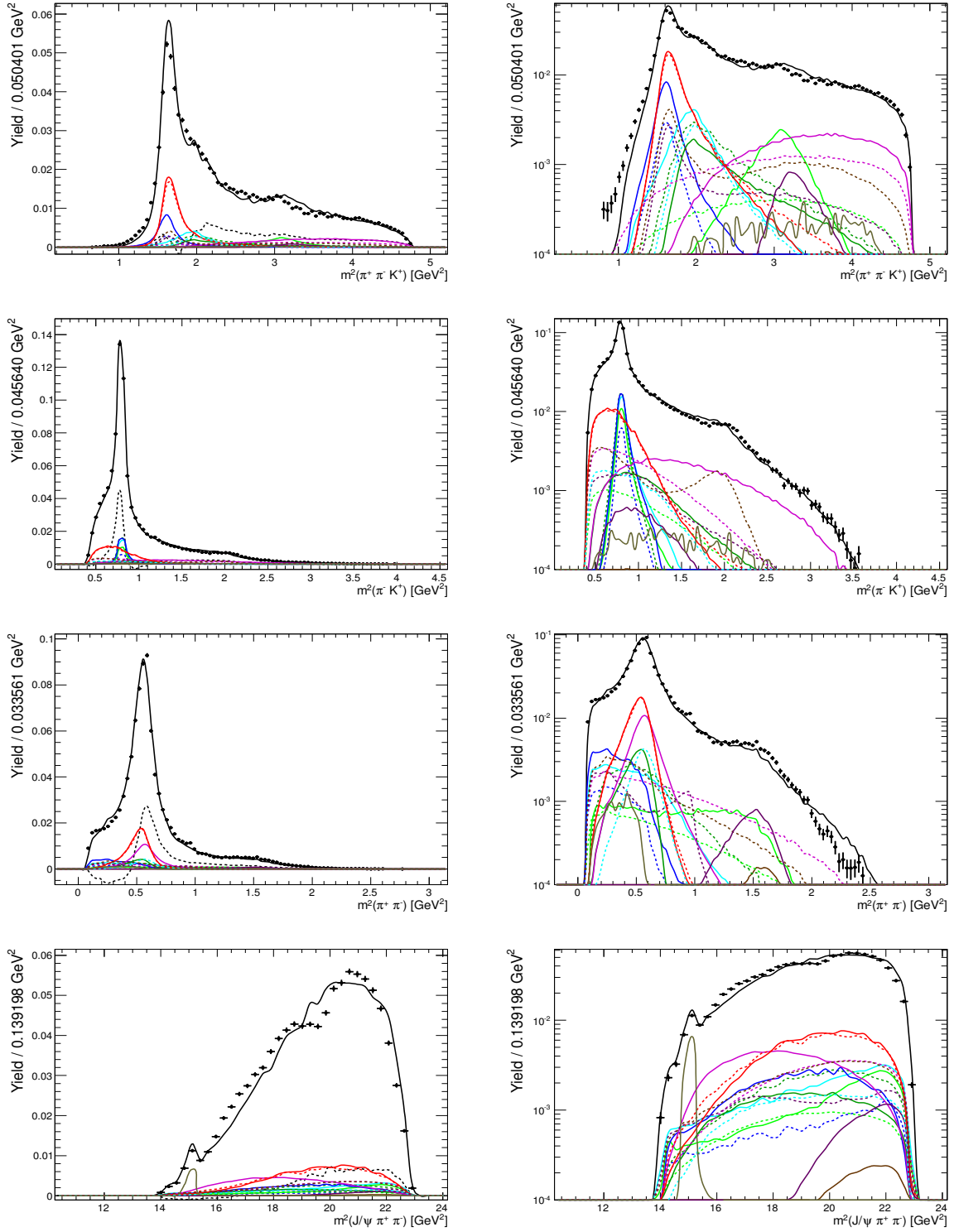
Figure 8.3: Distributions of the phase space observables for data (points with error bars) and best fit projections (black solid line). The individual amplitude contributions are color-coded as in the legend in Fig. 8.4.

74

Interference
$B^+ \rightarrow J/\psi\ [K(1)(1270)^+ \rightarrow \pi^+\ K^*(892)]$
$B^+ \rightarrow J/\psi\ [K(1)(1400)^+ \rightarrow \pi^+\ K^*(892)]$
$B^+ \rightarrow J/\psi\ [K(2)(1770)^+ \rightarrow \pi^+\ K^*(892)]$
$B^+ \rightarrow J/\psi\ [K(2)(2250)^+ \rightarrow K^+\ f(2)(1270)]$
$B^+ \rightarrow J/\psi\ [K^*(1410)^+ \rightarrow \pi^+\ K^*(892)]$
$B^+ \rightarrow \pi^+\ [NV \rightarrow J/\psi\ NS]$
$B^+[P] \rightarrow J/\psi\ [K(1)(1270)^+ \rightarrow \pi^+\ K^*(892)]$
$B^+ \rightarrow J/\psi\ [K^*(1410)^+ \rightarrow K^+\ \rho(770)]$
$B^+ \rightarrow J/\psi\ [NV \rightarrow K^+\ \rho(770)]$
$B^+ \rightarrow [NA \rightarrow J/\psi\ \pi^+]\ [NS \rightarrow K^+\ \pi^-]$
$B^+ \rightarrow J/\psi\ [K(1)(1270)^+ \rightarrow K^+\ f(0)(980)]$
$B^+ \rightarrow J/\psi\ [K(1)(1270)^+ \rightarrow K^+\ \rho(770)]$
$B^+[P] \rightarrow J/\psi\ [K(1)(1270)^+ \rightarrow K^+\ \rho(770)]$
$B^+ \rightarrow J/\psi\ [K(1)(1270)^+ \rightarrow \pi^+\ K(0)^*(1430)]$
$B^+ \rightarrow J/\psi\ [K(2)(1770)^+ \rightarrow K^+\ f_2(1270)]$
$B^+ \rightarrow J/\psi\ [K(1)(1400)^+ \rightarrow K^+\ \rho(770)]$
$B^+ \rightarrow K^+\ [X(3872) \rightarrow J/\psi\ \rho(770)]$
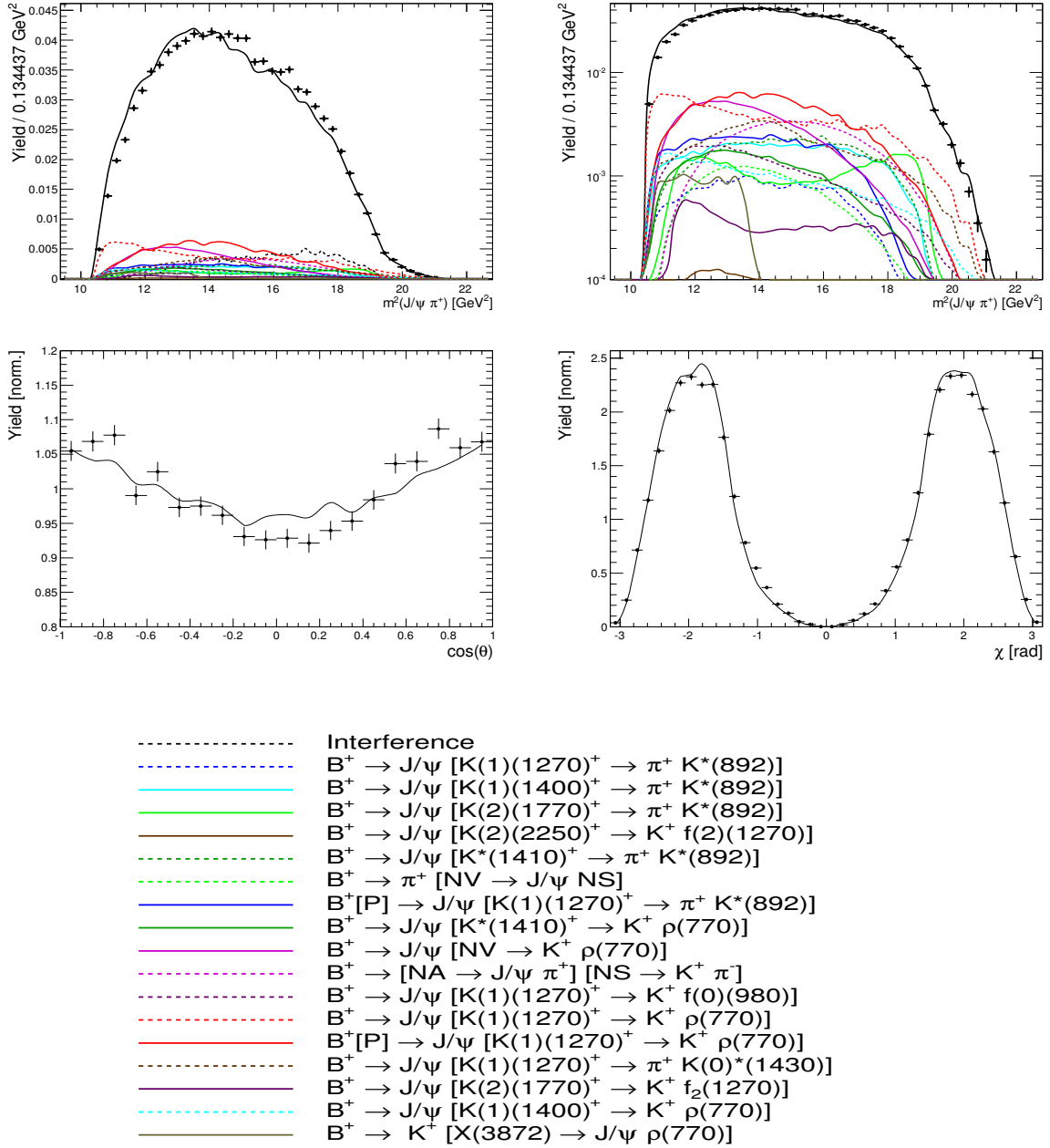
Figure 8.4: Distributions of the phase space observables for data (points with error bars) and best fit projections (black solid line). The individual amplitude contributions are color-coded as in the legend.

9   Summary, Conclusions and Outlook

In this thesis, the first amplitude analysis of the decay $B^+ \to J/\psi\,K^+\pi^+\pi^-$ in full seven-dimensional phase space is presented. The study is based on the dataset taken by the LHCb experiment in 2011 and 2012, corresponding to an integrated luminosity of $\mathcal{L} = 3\,\mathrm{fb}^{-1}$. By utilization of a multivariate classifier to discriminate signal from combinatorial background, a very clean sample of nearly 110 000 signal events is selected with a background level of 4% within $\pm 50\,\mathrm{MeV}$ of the signal peak.

The complicated resonant structure comprising multiple broad, overlapping resonances necessitates a sophisticated Dalitz plot analysis exploiting the full phase space information in order to identify the intermediate state contributions. For this purpose, the spin-dependent angular distributions for various decay chains are derived in a covariant tensor formalism accounting for angular momentum and, where appropriate, parity conservation. This formalism does not only allow the resonant structure of the $K^+\pi^+\pi^-$, $K^+\pi^-$ and $\pi^+\pi^-$ systems to be studied, but also those of the $J/\psi\,\pi^+\pi^-$ and $J/\psi\,\pi^\pm$ systems in contrast to the simplified three-dimensional approach used in a previous analysis by the Belle collaboration. Furthermore, different spin and angular momentum couplings between the decay products can be considered. The complex couplings to the decay channels, from which the fractional contributions can be inferred, are extracted from data by performing an unbinned maximum likelihood fit, where the theoretical distribution has to be corrected for experimental effects. For that reason, the impact of the selection and reconstruction efficiency as well as the finite momentum resolution on the phase space distribution is studied in detail. Where the latter is found to be negligible, the acceptance is incorporated in the amplitude fit by using fully simulated phase space MC events to numerically evaluate the normalization integral of the likelihood function.

The presented amplitude model contains a total of 17 components. The prominent contribution is found to be the $K_1(1270)$ resonance in the decay modes $K_1(1270) \to K^+\,\rho(770)$, $K_1(1270) \to K^*(892)\,\pi^+$, $K_1(1270) \to K_0^*(1430)\,\pi^+$ and $K_1(1270) \to K^+ f_0(980)$ with decay fractions 26.34%, 7.05%, 6.63% and 3.61%, respectively. Furthermore, a significant contribution of the decay channel $B^+ \to J/\psi\,K^+\rho(770)$ is observed. Except for the $X(3872)$ meson, no charmonium(-like) resonances decaying to $J/\psi\,\pi^+\pi^-$ or $J/\psi\,\pi^\pm$ could have been unambiguously identified within the current precision of the method.

Further studies are required to clarify the resonant substructure of the $J/\psi\,\pi^+\pi^-$ and $J/\psi\,\pi^\pm$ systems as well as the high mass region of the $K^+\pi^+\pi^-$ system ($m(K^+\pi^+\pi^-) > 1.5\,\mathrm{GeV}$). In particular, more precise masses and widths of the resonances as well as the possibility to let these parameters float in the fit are necessary to that end. Due to the overwhelming abundance of potential decay channels, the resonance model is necessarily incomplete making the model selection a delicate problem. At this point, the development of a more sophisticated model selection procedure is needed in order to find the optimal set of amplitudes. This set of amplitudes should yield a minimal χ^2 value on condition that the number of included amplitudes is as small as possible. The baseline model presented in this thesis should definitely provide an excellent starting point for this purpose.

One of the main achievements of this thesis is clearly the calculation of the spin factors for the general decay type $P \to V\,P\,P\,P$. These spin factors can be immediately applied to analyze similar decay channels such as $B^+ \to \psi(2S)K^+\pi^+\pi^-$. In fact, this decay mode would provide a simpler environment since the available $K^+\pi^+\pi^-$ phase space is much smaller due to the higher mass of the $\psi(2S)$ meson with respect to the J/ψ meson. Therefore, less exited kaon resonances are expected to contribute as intermediate states and the study of this decay would be an important cross check for the amplitude analysis of the decay $B^+ \to J/\psi\,K^+\pi^+\pi^-$. Additionally, it might be possible to confirm the existence of the exotic $Z(4430)$ meson which was previously observed in $B^0 \to \psi(2S)K^+\pi^-$ decays [13].

Another possible application is an amplitude analysis of the decay $B^+ \to J/\psi\,K^+K^+K^-$ which also promises several exciting substructures such as $X(4140) \to J/\psi\,(\phi(1020) \to K^+K^-)$ possibly seen by the D0 [72] and the CMS [73] collaborations.

Moreover, a study of the radiative decay $B^+ \to \gamma\,K^+\pi^+\pi^-$ might be feasible. This decay channel provides an uniquely clean window on the $K^+\pi^+\pi^-$ resonance composition since no bound states involving a photon are possible and, on top of that, allows measuring the photon polarization in the flavour-changing neutral-current transition $b \to s\gamma$ which is forbidden at tree-level [74]. Where the Standard model predicts the photon to be predominantly left-handed, several extension of the Standard Model predict a significant right-handed contribution due to the exchange of heavy fermions in the electroweak loop. In 2014, the LHCb collaboration reported the first observation of a non zero photon polarization by measuring the up-down asymmetry between the number of photons on each side of the $K^+\pi^+\pi^-$ decay plane in four bins of the $K^+\pi^+\pi^-$ mass [75]. However, the unknown $K^+\pi^+\pi^-$ structure prevents the translation of the up-down asymmetry to an actual value of the photon polarization. An amplitude analysis could therefore lead to the first measurement of the photon polarization in $b \to s\gamma$ transitions thereby searching for new physics beyond the Standard Model.

Appendix

A   Calculation of spin factors

In this section, the important intermediate steps to derive the spin factors in Table 2.2 are shown. In particular, the two-body amplitudes for each node of the decay tree, obtained from the general rule in Eq. 2.67, are explicitly given. The two-body amplitudes are then multiplied and spin sums are applied in order to obtain the spin factor as described in Sec. 2.2.4.

$$B^+[S] \to J/\psi \; \big[K_1(1270)^+[P] \to \pi^+ \big(K_0^*(1430)[S] \to K^+\pi^-\big)\big]$$

$$\langle A\,V_0, 0\,0|\mathcal{M}|B\rangle = \varepsilon_\alpha^*(V_0)\,\varepsilon^{*\alpha}(A) \tag{A.1}$$

$$\langle S\,P_1, 1\,0|\mathcal{M}|A\rangle = \varepsilon^\mu(A)\,L_{(1)\mu}(A) \tag{A.2}$$

$$\langle P_3\,P_2, 0\,0|\mathcal{M}|S\rangle = 1 \tag{A.3}$$

$$S_f = \varepsilon^{*\alpha}(V_0)\,L_{(1)\alpha}(A) \tag{A.4}$$

$$B^+[S] \to J/\psi \; \big[K^*(1410)^+[P] \to \pi^+ \big(K^*(892)[P] \to K^+\pi^-\big)\big]$$

$$\langle V_1\,V_0, 0\,0|\mathcal{M}|B\rangle = \varepsilon_\alpha^*(V_0)\,\varepsilon^{*\alpha}(V_1) \tag{A.5}$$

$$\langle V_2\,P_1, 1\,1|\mathcal{M}|V_1\rangle = \varepsilon_{\kappa\lambda\mu\nu}\,\varepsilon^\kappa(V_1)\,L_{(1)}^\lambda(V_1)\,p_{V_1}^\mu\,P_{(1)}^{\nu\xi}(V_1)\,\varepsilon_\xi^*(V_2) \tag{A.6}$$

$$\langle P_2\,P_3, 1\,0|\mathcal{M}|V_2\rangle = \varepsilon_\rho(V_2)\,L_{(1)}^\rho(V_2) \tag{A.7}$$

$$S_f = \varepsilon_\alpha^*(V_0)\,P_{(1)}^{\alpha\kappa}(V_1)\,\varepsilon_{\kappa\lambda\mu\nu}\,L_{(1)}^\lambda(V_1)\,p_{V_1}^\mu\,P_{(1)}^{\nu\xi}(V_1)\,L_{(1)\xi}(V_2) \tag{A.8}$$

$$B^+[P] \to J/\psi \; \big[K_2(1770)^+[S] \to \pi^+ \big(K_2^*(1430)[D] \to K^+\pi^-\big)\big]$$

$$\langle T_-\,V_0, 1\,1|\mathcal{M}|B\rangle = L_{(1)\alpha}(B)\,\varepsilon^{*\alpha\beta}(T_-)\,\varepsilon_\beta^*(V_0) \tag{A.9}$$

$$\langle T_+\,P_1, 0\,2|\mathcal{M}|T_-\rangle = \varepsilon_{\kappa\lambda}(T_-)\,P_{(2)}^{\kappa\lambda\mu\nu}(T_-)\,\varepsilon_{\mu\nu}^*(T_+) \tag{A.10}$$

$$\langle P_2\,P_3, 2\,0|\mathcal{M}|T_+\rangle = \varepsilon_{\rho\sigma}(T_+)\,L_{(2)}^{\rho\sigma}(T_+) \tag{A.11}$$

$$S_f = L_{(1)\alpha}(B)\,\varepsilon_\beta^*(V_0)\,P_{(2)}^{\alpha\beta\mu\nu}(T_-)\,L_{(2)\mu\nu}(T_+) \tag{A.12}$$

78

$B^+[P] \to J/\psi \; [K_2(1770)^+[P] \to \pi^+ \, (K^*(892)[P] \to K^+\pi^-)]$

$$\langle T_- \, V_0, 1\,1 | \mathcal{M} | B \rangle = L_{(1)\alpha}(B) \, \varepsilon^{*\alpha\beta}(T_-) \, \varepsilon^*_\beta(V_0) \tag{A.13}$$

$$\langle V \, P_1, 1\,1 | \mathcal{M} | T_- \rangle = \varepsilon_{\lambda\mu}(T_-) \, L^\lambda_{(1)}(T_-) \, P^{\mu\nu}_{(1)}(T_-) \, \varepsilon^*_\nu(V) \tag{A.14}$$

$$\langle P_2 \, P_3, 1\,0 | \mathcal{M} | V \rangle = \varepsilon_\rho(V) \, L^\rho_{(1)}(V) \tag{A.15}$$

$$S_f = L_{(1)\alpha}(B) \, \varepsilon^*_\beta(V_0) \, P^{\alpha\beta\lambda\mu}_{(2)}(T_-) \, L_{(1)\lambda}(T_-) \, P_{(1)\mu\nu}(T_-) \, L^\nu_{(1)}(V) \tag{A.16}$$

$B^+[P] \to J/\psi \; [K_2(1770)^+[D] \to K^+ \, (f_0(980)[S] \to \pi^+\pi^-)]$

$$\langle T_- \, V_0, 1\,1 | \mathcal{M} | B \rangle = L_{(1)\alpha}(B) \, \varepsilon^{*\alpha\beta}(T_-) \, \varepsilon^*_\beta(V_0) \tag{A.17}$$

$$\langle S \, P_1, 2\,0 | \mathcal{M} | T_- \rangle = \varepsilon_{\mu\nu}(T_-) \, L^{\mu\nu}_{(2)}(T_-) \tag{A.18}$$

$$\langle P_3 \, P_2, 0\,0 | \mathcal{M} | S \rangle = 1 \tag{A.19}$$

$$S_f = L_{(1)\alpha}(B) \, \varepsilon^*_\beta(V_0) \, L^{\alpha\beta}_{(2)}(T_-) \tag{A.20}$$

$B^+[P] \to J/\psi \; \left[K_2^*(1430)^+[D] \to \pi^+ \, (K^*(892)[P] \to K^+\pi^-) \right]$

$$\langle T_+ \, V_0, 1\,1 | \mathcal{M} | B \rangle = L_{(1)\alpha}(B) \, \varepsilon^{*\alpha\beta}(T_+) \, \varepsilon^*_\beta(V_0) \tag{A.21}$$

$$\langle V \, P_1, 2\,1 | \mathcal{M} | T_+ \rangle = \varepsilon_{\kappa\lambda\mu\nu} \, p^\kappa_{T_+} \, \varepsilon^{\lambda\xi}(T_+) \, L^\mu_{(2)\xi}(T_+) \, P^{\nu o}_{(1)}(T_+) \, \varepsilon^*_o(V) \tag{A.22}$$

$$\langle P_2 \, P_3, 1\,0 | \mathcal{M} | V \rangle = \varepsilon_\rho(V) \, L^\rho_{(1)}(V) \tag{A.23}$$

$$S_f = \varepsilon_{\kappa\lambda\mu\nu} \, p^\kappa_{T_+} \, L_{(1)\alpha}(B) \, \varepsilon^*_\beta(V_0) \, P^{\alpha\beta\lambda\xi}_{(2)} \, L^\mu_{(2)\xi}(T_+) \, P^{\nu\rho}_{(1)}(T_+) \, L_{(1)\rho}(V) \tag{A.24}$$

$B^+[P] \to K^+ \; [X(3872)[S] \to J/\psi \, (\rho(770)[P] \to \pi^+\pi^-)]$

$$\langle A \, P_1, 1\,1 | \mathcal{M} | B \rangle = L_{(1)\alpha}(B) \, \varepsilon^{*\alpha}(A) \tag{A.25}$$

$$\langle V \, V_0, 0\,1 | \mathcal{M} | A \rangle = \varepsilon_\xi(A) \, P^{\xi\kappa}_{(1)}(A) \, \varepsilon_{\kappa\lambda\mu\nu} \, p^\lambda_A \, \varepsilon^{*\mu}(V_0) \, \varepsilon^{*\mu}(V) \tag{A.26}$$

$$\langle P_2 \, P_3, 1\,0 | \mathcal{M} | V \rangle = \varepsilon_\rho(V) \, L^\rho_{(1)}(V) \tag{A.27}$$

$$S_f = L_{(1)\alpha}(B) \, P^{\alpha\kappa}_{(1)}(A) \, \varepsilon_{\kappa\lambda\mu\nu} \, p^\lambda_A \, \varepsilon^{*\mu}(V_0) \, L^\nu_{(1)}(V) \tag{A.28}$$

$B^+[P] \to K^+ \; [X(4260)[S] \to J/\psi \, (f_0(980)[S] \to \pi^+\pi^-)]$

$$\langle V \, P_1, 1\,1 | \mathcal{M} | B \rangle = L_{(1)\alpha}(B) \, \varepsilon^{*\alpha}(V) \tag{A.29}$$

$$\langle S \, V_0, 0\,1 | \mathcal{M} | V \rangle = \varepsilon^\mu(V) \, P_{(1)\mu\nu}(V) \, \varepsilon^{*\nu}(V_0) \tag{A.30}$$

$$\langle P_2 \, P_3, 0\,0 | \mathcal{M} | S \rangle = 1 \tag{A.31}$$

$$S_f = L_{(1)\alpha}(B) \, P^{\alpha\beta}_{(1)}(V) \, \varepsilon^*_\beta(V_0) \tag{A.32}$$

$B^+[P] \to K^+\ [X(4260)[S] \to \pi^\pm\, (Z(3900)^\mp[S] \to J/\psi\, \pi^\mp)]$

$$\langle V\, P_1, 1\, 1|\mathcal{M}|B\rangle = L_{(1)\alpha}(B)\, \varepsilon^{*\alpha}(V) \tag{A.33}$$

$$\langle A\, P_2, 0\, 1|\mathcal{M}|V\rangle = \varepsilon^\mu(V)\, P_{(1)\mu\nu}(V)\, \varepsilon^{*\nu}(A) \tag{A.34}$$

$$\langle V_0\, P_3, 0\, 1|\mathcal{M}|A\rangle = \varepsilon^\rho(A)\, P_{(1)\rho\sigma}(A)\, \varepsilon^{*\sigma}(V_0) \tag{A.35}$$

$$S_f = L_{(1)\alpha}(B)\, P_{(1)}^{\alpha\beta}(V)\, P_{(1)\beta\rho}(V)\, \varepsilon^{*\rho}(V_0) \tag{A.36}$$

$B^+[S] \to (Z(3900)^+[S] \to J/\psi\, \pi^+)\, (K^*(892)[P] \to K^+\pi^-)$

$$\langle A\, V, 0\, 0|\mathcal{M}|B\rangle = \varepsilon^{*\alpha}(A)\, \varepsilon_\alpha^*(V) \tag{A.37}$$

$$\langle V_0\, P_3, 0\, 1|\mathcal{M}|A\rangle = \varepsilon^\mu(A)\, P_{(1)\mu\nu}(A)\, \varepsilon^{*\nu}(V_0) \tag{A.38}$$

$$\langle P_2\, P_3, 1\, 0|\mathcal{M}|V\rangle = \varepsilon_\rho(V)\, L_{(1)}^\rho(V) \tag{A.39}$$

$$S_f = L_{(1)\alpha}(V)\, P_{(1)}^{\alpha\beta}(A)\, \varepsilon_\beta^*(V_0) \tag{A.40}$$

$B^+[P] \to (Z(4239)^+[P] \to J/\psi\, \pi^+)\, (K^*(892)[P] \to K^+\pi^-)$

$$\langle P\, V, 1\, 1|\mathcal{M}|B\rangle = L_{(1)}^\alpha(B)\, \varepsilon_\alpha^*(V) \tag{A.41}$$

$$\langle V_0\, P_3, 1\, 1|\mathcal{M}|P\rangle = L_{(1)}^\mu(P)\, \varepsilon_\mu^*(V_0) \tag{A.42}$$

$$\langle P_2\, P_3, 1\, 0|\mathcal{M}|V\rangle = \varepsilon_\rho(V)\, L_{(1)}^\rho(V) \tag{A.43}$$

$$S_f = L_{(1)\alpha}(B)\, L_{(1)}^\alpha(V)\, L_{(1)}^\mu(P)\, \varepsilon_\mu^*(V_0) \tag{A.44}$$

B   Comparison of data and simulation

Figures B.1 and B.2 compare the p, p_T and χ^2_{IP} distributions of all final state particles for *sWeighted* data and truth matched MC events.
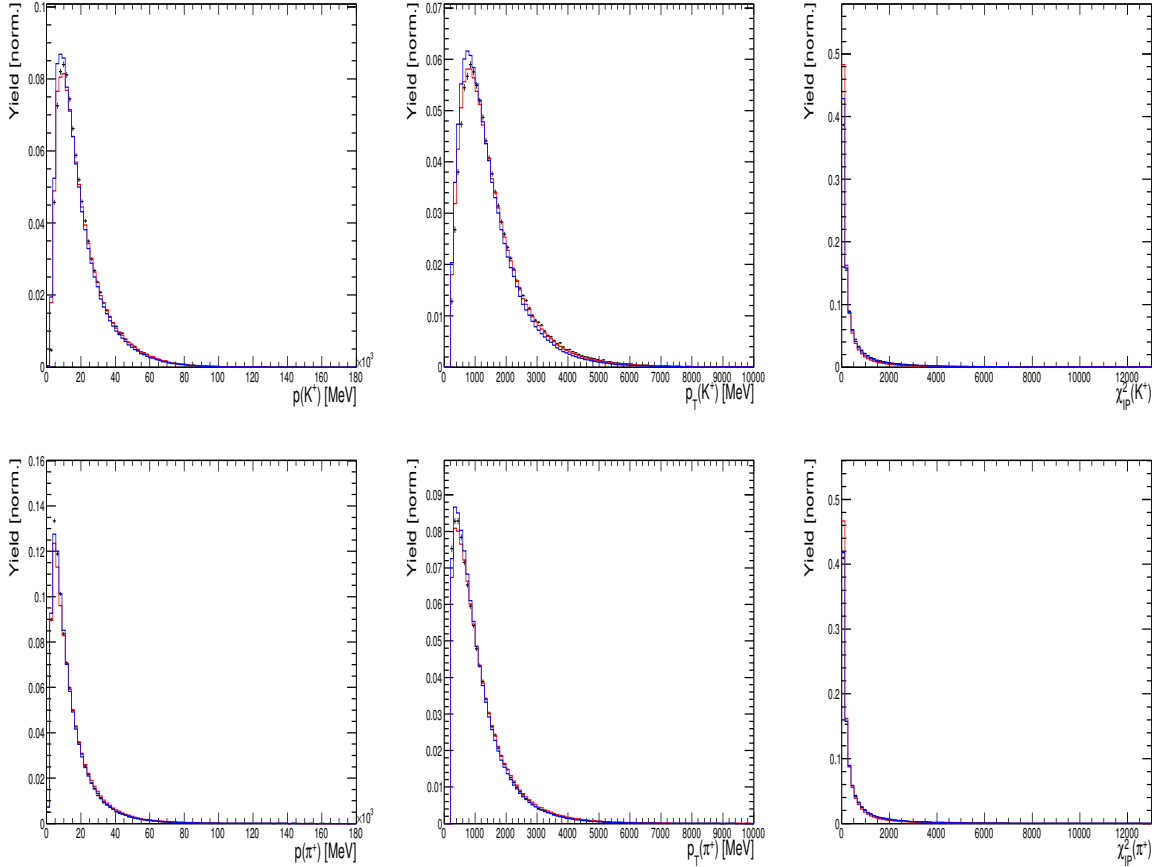
Figure B.1: Comparison of data (black) and MC simulated events before (red) and after applying all corrections (blue). The histograms are normalized to unity.
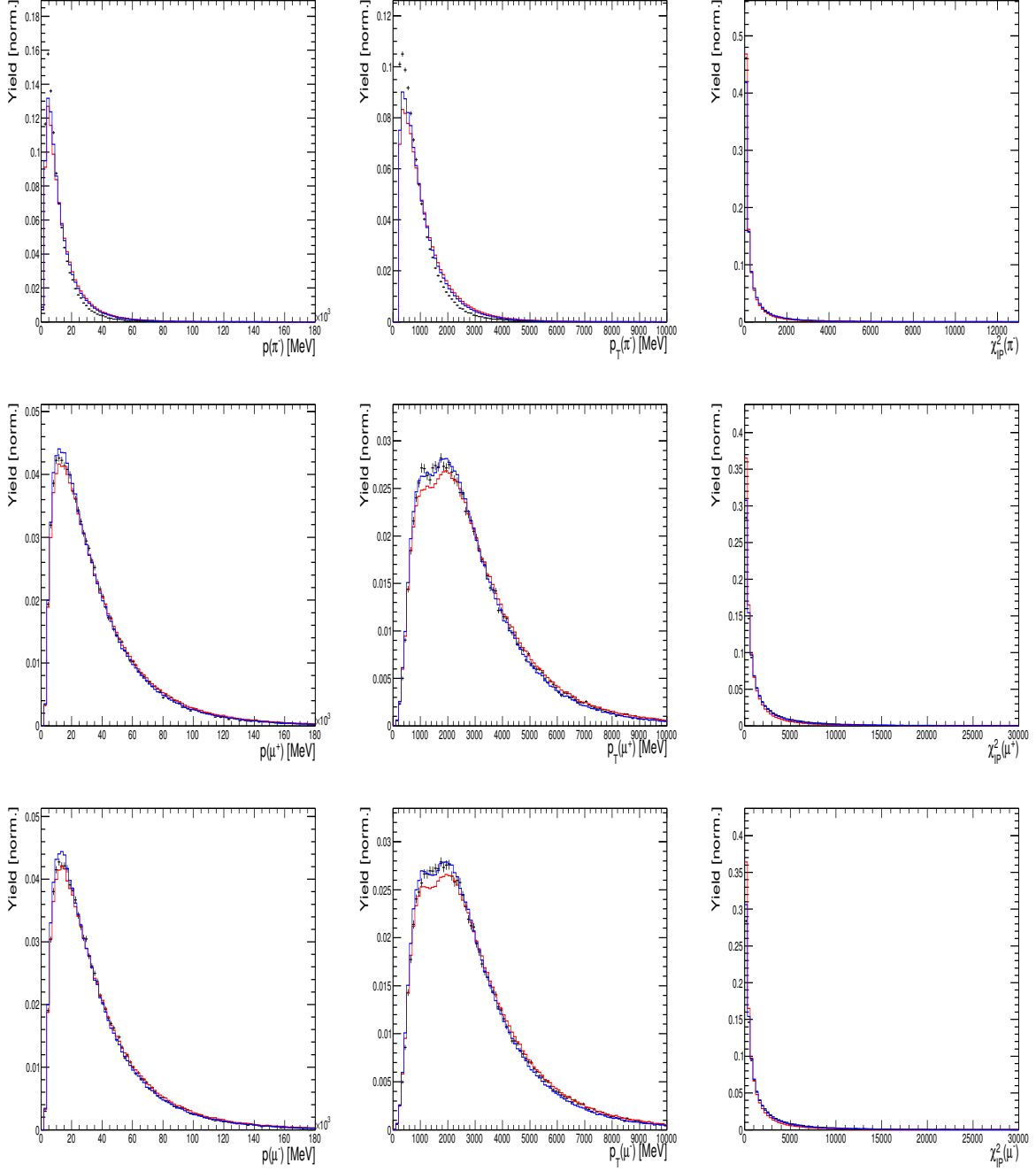
Figure B.2: Comparison of data (black) and MC simulated events before (red) and after applying all corrections (blue). The histograms are normalized to unity.

C Parameterization of the efficiency function

This section presents an alternative approach to determine the acceptance across the Dalitz plot $\varepsilon(D)$. Instead requiring a binning, the efficiency is parameterized in terms of Chebyshev polynomials. A similar approach has been used *e.g.* in Ref. [13]. The Chebyshev polynomials $T_n(x)$ are defined recursively as

$$T_0(x) = 1 \tag{C.1}$$

$$T_1(x) = x \tag{C.2}$$

$$T_{n+1}(x) = 2\,x\,T_n(x) - T_{n-1}(x) \tag{C.3}$$

and have the important property that they are orthogonal on the interval $[-1, 1]$ with respect to the weight $1/\sqrt{1-x^2}$:

$$\int_{-1}^{1} T_n(x)T_m(x)\,\frac{dx}{\sqrt{1-x^2}} = \begin{cases} 0 & : n \neq m \\ \pi & : n = m = 0 \\ \pi/2 & : n = m \neq 0 \end{cases} . \tag{C.4}$$

To exploit the orthogonality, the five invariant mass combinations $m_i^2 \in [m_{i,min}^2, m_{i,max}^2]$ are mapped to the interval $[-1, 1]$ by a linear transformation

$$x_i = 2\,\frac{m_i^2 - m_{i,min}^2}{m_{i,max}^2 - m_{i,min}^2} - 1 \,. \tag{C.5}$$

The efficiency weighted phase space distribution is then expanded in a series of Chebyshev polynomials as

$$\epsilon(\vec{x})\phi(\vec{x}) = \sum_{i,j,k,l,m} c_{ijklm}\,T_i(x_1)T_j(x_2)T_k(x_3)T_l(x_4)T_m(x_5) \,. \tag{C.6}$$

where the coefficients can be calculated by utilizing Eq. C.4 as:

$$c_{ijklm} = \frac{1}{\pi^5} \int_{-1}^{1} \epsilon(\vec{x})\,\phi(\vec{x})\,T_i(x_1)T_j(x_2)T_k(x_3)T_l(x_4)T_m(x_5)$$

$$\cdot\,\Theta(i)\Theta(j)\Theta(k)\Theta(l)\Theta(m)\,\frac{dx_1}{\sqrt{1-x_1^2}}\,\frac{dx_2}{\sqrt{1-x_2^2}}\,\frac{dx_3}{\sqrt{1-x_3^2}}\,\frac{dx_4}{\sqrt{1-x_4^2}}\,\frac{dx_5}{\sqrt{1-x_5^2}} \tag{C.7}$$

with $\Theta(i = 0) = 1$ and $\Theta(i \geq 0) = 2$. Equation C.7 is numerically evaluated by performing a MC integration using the selected $B^+ \to J/\psi\,K^+\pi^+\pi^-$ phase space MC sample

$$c_{ijklm} = \frac{1}{N_{MC}\,\pi^5} \sum_{e}^{N_{MC}} \frac{T_i(x_{1e})}{\sqrt{1-x_{1e}^2}}\,\frac{T_j(x_{2e})}{\sqrt{1-x_{2e}^2}}\,\frac{T_k(x_{3e})}{\sqrt{1-x_{3e}^2}}\,\frac{T_l(x_{4e})}{\sqrt{1-x_{4e}^2}}\,\frac{T_m(x_{5e})}{\sqrt{1-x_{5e}^2}}\,\Theta(i)\Theta(j)\Theta(k)\Theta(l)\Theta(m) \,. \tag{C.8}$$
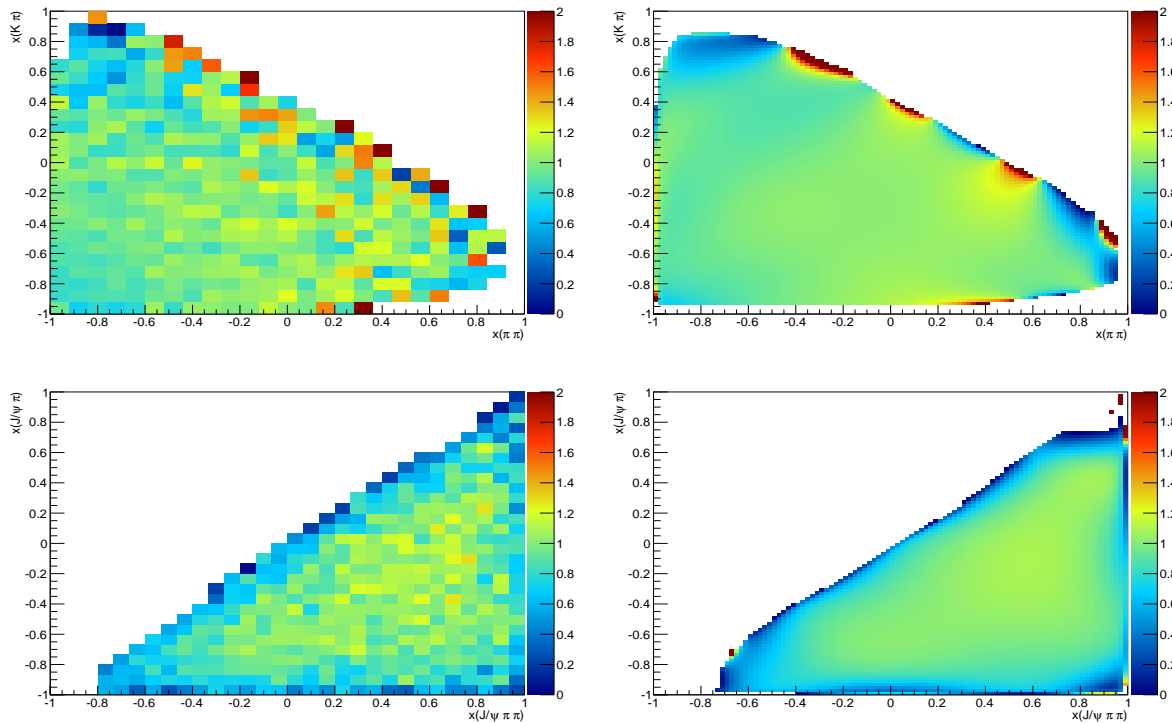
Figure B.1: Two-dimensional projections of the efficiency (left) and parameterized efficiency (right).

The same procedure is applied to expand the phase space distribution, $\phi(\vec{x})$, using a generator level MC sample. The efficiency is then given by $\varepsilon(\vec{x}) = \frac{\varepsilon(\vec{x}) \phi(\vec{x})}{\phi(\vec{x})}$. In the limit of infinite number of orders and infinite MC statistics, the efficiency is reproduced exactly. However, in practice, the expansion has to be truncated at some point. In this case, the number of orders per dimension is restricted to eight leading to $32\,768$ coefficients c_{ijklm} to calculate in total. The two-dimensional projections of the parameterized efficiency are shown in Fig. B.1 while Fig. B.2 shows the one-dimensional projections superimposed on the MC distribution. An overall good agreement is observed. However, it can happen that the expansion returns values smaller than zero. In that case, the efficiency is set to zero. Especially the corners of the phase space are prone to that problem as can be seen in Fig. B.1. Possible solutions are to include even more orders or the usage of a different set of orthogonal polynomials, *e.g.* Legendre polynomials, which might be better suited for the expansion.
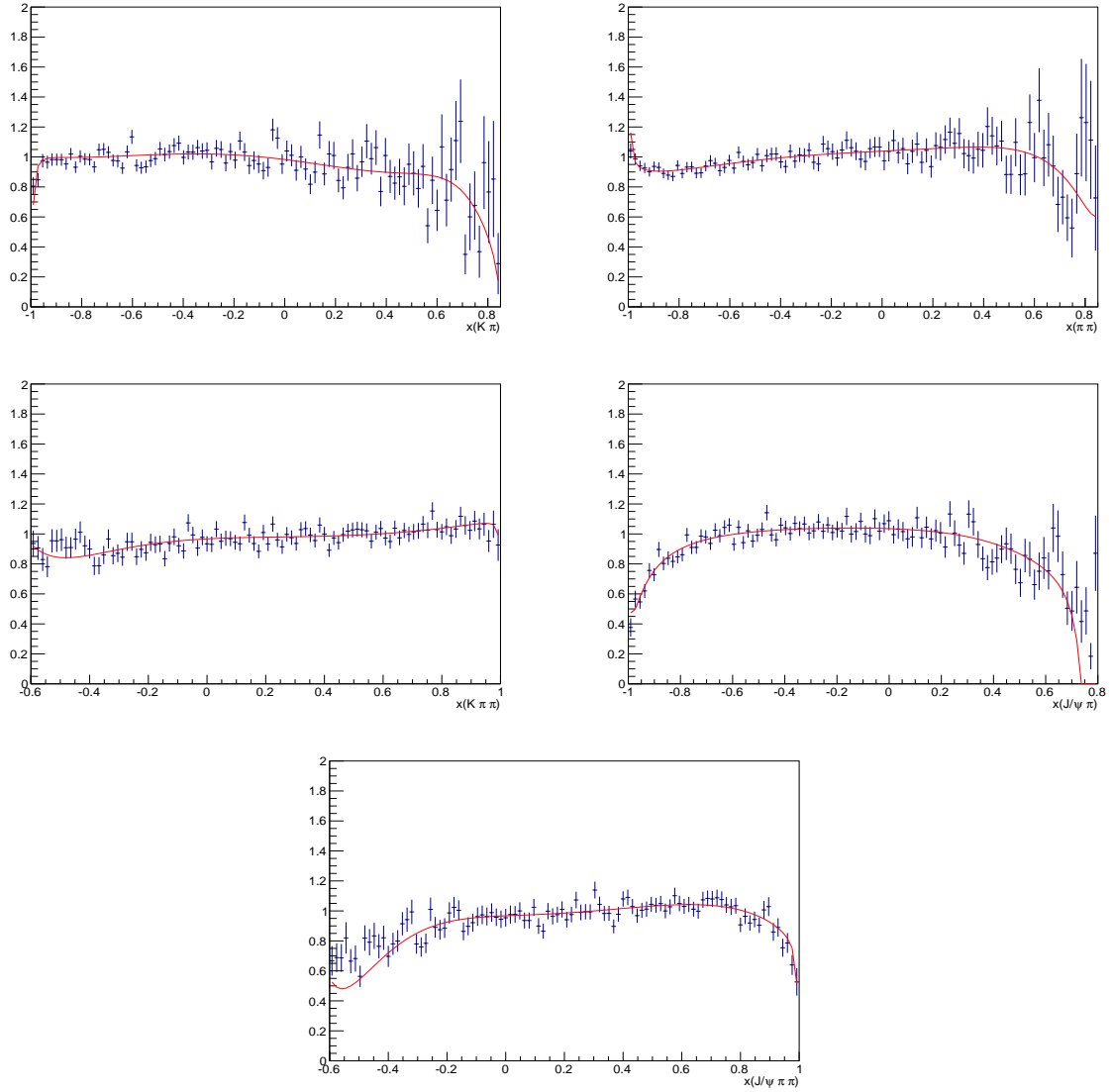
Figure B.2: One-dimensional projections of the parameterized efficiency superimposed on the MC distribution. The normalization corresponds to an average efficiency of unity.

D Mass and width of resonances

The masses, widths and spin-parity values of the resonances considered in this analysis are listed in Table D.1.

Table D.1: Masses, widths and spin-parity values of resonances. All values are taken from the PDG [31], except for the values for the resonances $Z(4240)$ and $Z(4430)$ which are taken from Ref. [13].

Resonance	Mass [MeV]	Width [MeV]	$\mathbf{J^P}$
$\rho(770)$	775.26 ± 0.25	147.8 ± 0.9	1^-
$\omega(782)$	782.65 ± 0.12	8.49 ± 0.08	1^-
$K^*(892)$	895.81 ± 0.19	47.4 ± 0.6	1^-
$f_0(980)$	990 ± 20	$50 \ ^{+50}_{-20}$	0^+
$f_2(1270)$	1275.1 ± 1.2	$184.2 \ ^{+4}_{-2.4}$	2^+
$K_1(1270)$	1272 ± 7	90 ± 20	1^+
$K_1(1400)$	1403 ± 7	174 ± 13	1^+
$K^*(1410)$	1414 ± 15	232 ± 21	1^-
$K_0^*(1430)$	1425 ± 50	270 ± 80	0^+
$K_2^*(1430)$	1425.6 ± 1.5	98.5 ± 2.9	2^+
$K_2(1580)$	1580	110	2^-
$K^*(1680)$	1717 ± 27	322 ± 110	1^-
$K_2(1770)$	1773 ± 8	186 ± 14	2^-
$K_2(1820)$	1816 ± 13	276 ± 35	2^-
$K_2^*(1980)$	$1973 \pm 8 \pm 25$	$373 \pm 33 \pm 60$	2^+
$K_2(2250)$	2247 ± 17	180 ± 30	2^-
$\psi(2S)$	$3686.108 \ ^{+0.011}_{-0.014}$	0.286 ± 0.016	1^-
$X(3872)$	3871.68 ± 0.17	< 1.2	1^+
$Z(3900)$	3888.7 ± 3.4	35 ± 7	1^+
$\psi(4040)$	4039.6 ± 4.3	84.5 ± 12.3	1^-
$\psi(4160)$	4191 ± 5	70 ± 10	1^-
$Z(4240)$	$4239 \pm 18 \ ^{+45}_{-10}$	$220 \pm 47 \ ^{+108}_{-74}$	0^-
$\psi(4415)$	4415.1 ± 7.9	71.5 ± 19.0	1^-
$Z(4430)$	$4485 \pm 7 \ ^{+15}_{-25}$	$172 \pm 13 \ ^{+37}_{-34}$	1^+

E Decay chains

The amplitudes that have been implemented in MINT are listed below. The numbering of the spin factors refers to Table 2.2.

Table E.1: Cascade decays of *strange* resonances. Part one.

Decay chain	Spin factor
$B \rightarrow J/\psi\,[K_1(1270) \rightarrow K^*(892)\,\pi]$	1,2,3,4
$B \rightarrow J/\psi\,[K_1(1270) \rightarrow K_0^*(1430)\,\pi]$	5
$B \rightarrow J/\psi\,[K_1(1270) \rightarrow K\,\rho(770)]$	1,2,3,4
$B \rightarrow J/\psi\,[K_1(1270) \rightarrow K\,\omega]$	1,2,3,4
$B \rightarrow J/\psi\,[K_1(1270) \rightarrow K\,f_0(980)]$	5
$B \rightarrow J/\psi\,[K_1(1270) \rightarrow K\,f_0(1370)]$	5
$B \rightarrow J/\psi\,[K_1(1400) \rightarrow K^*(892)\,\pi]$	1,2,3,4
$B \rightarrow J/\psi\,[K_1(1400) \rightarrow K\,\rho(770)]$	1,2,3,4
$B \rightarrow J/\psi\,[K_1(1400) \rightarrow K\,\omega]$	1,2,3,4
$B \rightarrow J/\psi\,[K_1^*(1410) \rightarrow K^*(892)\,\pi]$	6
$B \rightarrow J/\psi\,[K_1^*(1410) \rightarrow K\,\rho(770)]$	6
$B \rightarrow J/\psi\,[K_1^*(1410) \rightarrow K\,\omega]$	6
$B \rightarrow J/\psi\,[K_2^*(1430) \rightarrow K^*(892)\,\pi]$	10
$B \rightarrow J/\psi\,[K_2^*(1430) \rightarrow K\,\rho(770)]$	10
$B \rightarrow J/\psi\,[K_2^*(1430) \rightarrow K\,\omega]$	10
$B \rightarrow J/\psi\,[K_2(1580) \rightarrow K^*(892)\,\pi]$	8
$B \rightarrow J/\psi\,[K_2(1580) \rightarrow K_2^*(1430)\,\pi]$	7
$B \rightarrow J/\psi\,[K_2(1580) \rightarrow K\,\rho(770)]$	8
$B \rightarrow J/\psi\,[K_2(1580) \rightarrow K\,\omega]$	8
$B \rightarrow J/\psi\,[K_2(1580) \rightarrow K\,f_0(980)]$	9
$B \rightarrow J/\psi\,[K_2(1580) \rightarrow K\,f_2(1270)]$	7
$B \rightarrow J/\psi\,[K_1^*(1680) \rightarrow K^*(892)\,\pi]$	6
$B \rightarrow J/\psi\,[K_1^*(1680) \rightarrow K\,\rho(770)]$	6
$B \rightarrow J/\psi\,[K_1^*(1680) \rightarrow K\,\omega]$	6

Table E.2: Cascade decays of *strange* resonances. Part two.

Decay chain	Spin factor
$B \to J/\psi \, [K_2(1770) \to K^*(892) \, \pi]$	8
$B \to J/\psi \, [K_2(1770) \to K_2^*(1430) \, \pi]$	7
$B \to J/\psi \, [K_2(1770) \to K \, \rho(770)]$	8
$B \to J/\psi \, [K_2(1770) \to K \, \omega]$	8
$B \to J/\psi \, [K_2(1770) \to K \, f_0(980)]$	9
$B \to J/\psi \, [K_2(1770) \to K \, f_2(1270)]$	7
$B \to J/\psi \, [K_2(1820) \to K^*(892) \, \pi]$	8
$B \to J/\psi \, [K_2(1820) \to K_2^*(1430) \, \pi]$	7
$B \to J/\psi \, [K_2(1820) \to K \, \rho(770)]$	8
$B \to J/\psi \, [K_2(1820) \to K \, \omega]$	8
$B \to J/\psi \, [K_2(1820) \to K \, f_0(980)]$	9
$B \to J/\psi \, [K_2(1820) \to K \, f_2(1270)]$	7
$B \to J/\psi \, [K_2^*(1980) \to K^*(892) \, \pi]$	10
$B \to J/\psi \, [K_2^*(1980) \to K \, \rho(770)]$	10
$B \to J/\psi \, [K_2^*(1980) \to K \, \omega]$	10
$B \to J/\psi \, [K_2(2250) \to K^*(892) \, \pi]$	8
$B \to J/\psi \, [K_2(2250) \to K_2^*(1430) \, \pi]$	7
$B \to J/\psi \, [K_2(2250) \to K \, \rho(770)]$	8
$B \to J/\psi \, [K_2(2250) \to K \, \omega]$	8
$B \to J/\psi \, [K_2(2250) \to K \, f_0(980)]$	9
$B \to J/\psi \, [K_2(2250) \to K \, f_2(1270)]$	7

Table E.3: Single resonance amplitudes.

Decay chain	Spin factor
$B \to J/\psi \, [K_1(1270) \to (K^+\pi^+)_P \, \pi^-]$	1
$B \to J/\psi \, [K_1(1270) \to K^+ \, (\pi^+\pi^-)_P]$	1
$B \to J/\psi \, [K_1(1270) \to (K^+\pi^-)_P \, \pi^+]$	1
$B \to J/\psi \, K^+ \, \rho(770)$	1,2,6
$B \to J/\psi \, K^*(892) \, \pi^+$	1,2,6

Table E.4: Decay channels involving charmonium(-like) resonances.

Decay chain	Spin factor
$B \to K\,[X(3872) \to J/\psi\,\rho]$	13
$B \to K\,[\psi(4040) \to J/\psi\,f_0(980)]$	12
$B \to K\,[\psi(4160) \to J/\psi\,f_0(980)]$	12
$B \to K\,[X(4260) \to J/\psi\,f_0(980)]$	12
$B \to K\,[X(4260) \to K\,Z(3900)]$	11
$B \to K\,[\psi(4415) \to J/\psi\,f_0(980)]$	12
$B \to K^*(892)\,[Z(3900) \to J/\psi\,\pi]$	14
$B \to K^*(892)\,[Z(4239) \to J/\psi\,\pi]$	15
$B \to K^*(892)\,[Z(4430) \to J/\psi\,\pi]$	14

Table E.5: Non resonant amplitudes.

Decay chain	Spin factor
$B \to J/\psi\,(K\,(\pi\,\pi)_P)_S$	1
$B \to J/\psi\,(\pi^+\,(K\,\pi^-)_P)_S$	1
$B \to J/\psi\,(\pi^-\,(K\,\pi^+)_P)_S$	1
$B \to J/\psi\,(K\,(\pi\,\pi)_S)_P$	5
$B \to J/\psi\,(\pi^+\,(K\,\pi^-)_S)_P$	5
$B \to J/\psi\,(\pi^-\,(K\,\pi^+)_S)_P$	5
$B[P] \to K\,(J/\psi\,(\pi\,\pi)_S)_S$	12
$B[P] \to \pi^+\,(J/\psi\,(K\,\pi^-)_S)_S$	12
$B[P] \to \pi^-\,(J/\psi\,(K\,\pi^+)_S)_S$	12
$B \to (J/\psi\,K)_S\,(\pi\,\pi)_P$	14
$B \to (J/\psi\,\pi^+)_S\,(K\,\pi^-)_P$	14
$B \to (J/\psi\,\pi^-)_S\,(K\,\pi^+)_P$	14
$B \to (J/\psi\,K)_P\,(\pi\,\pi)_P$	15
$B \to (J/\psi\,\pi^+)_P\,(K\,\pi^-)_P$	15
$B \to (J/\psi\,\pi^-)_P\,(K\,\pi^+)_P$	15

F   Alternative resonance models

The fit fractions and χ^2 values of the baseline and several alternative models are summarized in Table F.1.

Table F.1: Fractional contributions in percent for each component of the baseline model and various alternative models. Only the statistical uncertainties are given.

Decay mode	Baseline	1	2	3	4
$B \to J/\psi \, [K_1(1270) \to K^*(892)\,\pi]$	1.90 ± 0.09	1.89 ± 0.09	1.81 ± 0.08	2.03 ± 0.08	2.84 ± 0.11
$B[P] \to J/\psi \, [K_1(1270) \to K^*(892)\,\pi]$	5.15 ± 0.09	5.13 ± 0.09	5.14 ± 0.08	5.02 ± 0.09	5.49 ± 0.10
$B \to J/\psi \, [K_1(1270) \to K\,\rho(770)]$	14.09 ± 0.24	14.03 ± 0.24	14.67 ± 0.31	0.14 ± 0.28	12.06 ± 0.25
$B[P] \to J/\psi \, [K_1(1270) \to K\,\rho(770)]$	12.25 ± 0.18	12.19 ± 0.18	11.78 ± 0.20	12.06 ± 0.17	11.90 ± 0.17
$B \to J/\psi \, [K_1(1270) \to K\,\omega(782)]$		0.010 ± 0.002			
$B \to J/\psi \, [K_1(1270) \to K_0^*(1430)\,\pi]$	6.63 ± 0.19	6.60 ± 0.19	6.37 ± 0.15	5.40 ± 0.15	7.50 ± 0.17
$B \to J/\psi \, [K_1(1270) \to K\,f_0(980)]$	3.61 ± 0.11	3.59 ± 0.11	3.38 ± 0.10	3.87 ± 0.10	4.95 ± 0.14
$B \to J/\psi \, [K_1(1400) \to K^*(892)\,\pi]$	5.03 ± 0.14	5.01 ± 0.14	4.62 ± 0.14	4.76 ± 0.11	2.84 ± 0.14
$B \to J/\psi \, [K_1(1400) \to K\,\rho(770)]$	3.13 ± 0.13	3.12 ± 0.13	3.12 ± 0.14	3.10 ± 0.12	2.82 ± 0.14
$B \to J/\psi \, [K^*(1410) \to K^*(892)\,\pi]$	5.05 ± 0.11	5.03 ± 0.11	4.10 ± 0.09	6.74 ± 0.11	7.24 ± 0.15
$B \to J/\psi \, [K^*(1410) \to K\,\rho(770)]$	3.23 ± 0.12	3.21 ± 0.12	3.28 ± 0.10	1.58 ± 0.09	3.00 ± 0.13
$B \to J/\psi \, [K_2(1580) \to K^*(892)\,\pi]$			0.63 ± 0.05		0.67 ± 0.05
$B \to J/\psi \, [K_2(1770) \to K^*(892)\,\pi]$	3.45 ± 0.09	3.44 ± 0.09	2.23 ± 0.08	2.92 ± 0.06	1.83 ± 0.11
$B \to J/\psi \, [K_2(1770) \to K\,f_2(1270)]$	0.99 ± 0.06	0.99 ± 0.06	1.24 ± 0.06	0.54 ± 0.03	0.93 ± 0.07
$B \to J/\psi \, [K_2(2250) \to K\,f_2(1270)]$	0.53 ± 0.04	0.53 ± 0.04	0.27 ± 0.03	4.75 ± 0.13	3.35 ± 0.10
$B \to K \, [X(3872) \to J/\psi \, \rho(770)]$	1.02 ± 0.05	1.01 ± 0.05	1.00 ± 0.05	1.03 ± 0.05	1.06 ± 0.04
$B \to K \, [X(4260) \to J/\psi \, f_0(980)]$				0.52 ± 0.03	
$B \to K \, [X(4260) \to \pi^- \, Z(3900)]$				0.45 ± 0.02	
$B \to J/\psi \, [K\,\rho(770)]_P$	8.47 ± 0.15	8.44 ± 0.15	8.45 ± 0.16	10.62 ± 0.18	5.00 ± 0.15
$B[P] \to \pi^+ \, [J/\psi \, (K\,\pi^-)_S]_S$	2.04 ± 0.07	2.03 ± 0.07	2.16 ± 0.07		
$B[P] \to [J/\psi \, \pi^+]_S \, [K\pi^-]_S$	6.42 ± 0.13	6.39 ± 0.13	6.84 ± 0.14	2.6 ± 0.09	
$B \to J/\psi \, [K\,(\pi^+\pi^-)_P]_S$					3.57 ± 0.12
Sum	82.69 ± 0.30	82.64 ± 0.30	81.07 ± 0.31	82.34 ± 0.25	77.07 ± 0.32
χ^2_{5D}		2.48	2.48	2.47	2.44	2.52
χ^2_{7D}		2.12	2.12	2.11	2.14	2.33

References

[1] M. E. Peskin and D. V. Schroeder, *An Introduction To Quantum Field Theory (Frontiers in Physics)*, Westview Press, 1995.

[2] S. L. Glashow, J. Iliopoulos, and L. Maiani, *Weak interactions with lepton-hadron symmetry*, Phys. Rev. D **2** (1970) 1285.

[3] A. Salam and J. Ward, *Weak and electromagnetic interactions*, Il Nuovo Cimento Series 10 **11** (1959), no. 4 568.

[4] S. Weinberg, *A model of leptons*, Phys. Rev. Lett. **19** (1967) 1264.

[5] M. Gell-Mann, *A Schematic Model of Baryons and Mesons*, Phys. Lett. **8** (1964) 214.

[6] http://commons.wikimedia.org/wiki, 2014.

[7] Belle Collaboration, S. Choi *et al.*, *Observation of a narrow charmonium - like state in exclusive* $B^+ \rightarrow J/\psi K^+ \pi^+ \pi^-$ *decays*, Phys. Rev. Lett. **91** (2003) 262001, `arXiv:hep-ex/0309032`.

[8] LHCb, R. Aaij *et al.*, *Determination of the X(3872) meson quantum numbers*, Phys. Rev. Lett. **110** (2013) 222001, `arXiv:1302.6269`.

[9] T. Barnes and S. Godfrey, *Charmonium options for the X(3872)*, Phys. Rev. **D69** (2004) 054008, `arXiv:hep-ph/0311162`.

[10] N. A. Tornqvist, *Isospin breaking of the narrow charmonium state of Belle at 3872-MeV as a deuson*, Phys. Lett. **B590** (2004) 209, `arXiv:hep-ph/0402237`.

[11] L. Maiani, F. Piccinini, A. D. Polosa, and V. Riquer, *Diquark-antidiquark states with hidden or open charm and the nature of x(3872)*, Phys. Rev. D **71** (2005) 014028.

[12] B. A. Li, *Is X(3872) a possible candidate of hybrid meson*, Phys. Lett. **B605** (2005) 306, `arXiv:hep-ph/0410264`.

[13] LHCb collaboration, R. Aaij *et al.*, *Observation of the resonant character of the* $Z(4430)^-$ *state*, Phys. Rev. Lett. **112** (2014) 222002, `arXiv:1404.1903`.

[14] C. Amsler and N. Tornqvist, *Mesons beyond the naive quark model*, Phys. Rept. **389** (2004) 61.

[15] R. H. Dalitz, *Decay of τ mesons of known charge*, Phys. Rev. **94** (1954) 1046.

[16] M. V. Purohit, *Amplitude Analyses of D Decay Dalitz Plots*, `arXiv:1210.1393`.

[17] E. Byckling and K. Kajantie, *Particle Kinematics*, John Wiley & Sons, 1973.

[18] Belle Collaboration, K. Abe *et al.*, *Observation of $B \to J/\psi \, K(1)(1270)$*, Phys. Rev. Lett. **87** (2001) 161601, `arXiv:hep-ex/0105014`.

[19] Belle Collaboration, H. Guler *et al.*, *Study of the $K^+\pi^+\pi^-$ Final State in $B^+ \to J/\psi K^+\pi^+\pi^-$ and $B^+ \to \psi' K^+\pi^+\pi^-$*, Phys. Rev. **D83** (2011) 032005, `arXiv:1009.5256`.

[20] S. Mandelstam, J. Paton, R. F. Peierls, and A. Sarker, *Isobar approximation of production processes*, Annals of Physics **18** (1962), no. 2 198 .

[21] D. J. Herndon, P. Söding, and R. J. Cashmore, *Generalized isobar model formalism*, Phys. Rev. D **11** (1975) 3165.

[22] J. Brehm, *Unitarity and the isobar model: Two-body discontinuities*, Annals of Physics **108** (1977), no. 2 454 .

[23] C. Zemach, *Use of angular momentum tensors*, Phys. Rev. **140** (1965) B97.

[24] C. Zemach, *Determination of the Spins and Parities of Resonances*, Phys. Rev. **140** (1965) B109.

[25] V. Filippini, A. Fontana, and A. Rotondi, *Covariant spin tensors in meson spectroscopy*, Phys. Rev. **D51** (1995) 2247.

[26] B. Zou and D. Bugg, *Covariant tensor formalism for partial wave analyses of psi decay to mesons*, Eur. Phys. J. **A16** (2003) 537, `arXiv:hep-ph/0211457`.

[27] M. Williams, *Measurement of differential cross sections and spin density matrix elements along with a partial wave analysis for $\gamma p \to p\omega$ using CLAS at Jefferson Lab*, PhD thesis, Carnegie Mellon University, 2007, AAT-3299665.

[28] J. Blatt and V. Weisskopf, *Theoretical Nuclear Physics*, John Wiley & Sons, 1952.

[29] F. von Hippel and C. Quigg, *Centrifugal-barrier effects in resonance partial decay widths, shapes, and production amplitudes*, Phys. Rev. D **5** (1972) 624.

[30] J. Jackson, *Remarks on the phenomenological analysis of resonances*, Il Nuovo Cimento Series 10 **34** (1964), no. 6 1644.

[31] Particle Data Group, J. Beringer *et al.*, *Review of particle physics*, Phys. Rev. **D86** (2012) 010001.

[32] S. Flatté, *Coupled-channel analysis of the $\pi\eta$ and KK systems near KK threshold*, Physics Letters B **63** (1976), no. 2 224 .

[33] BES Collaboration, M. Ablikim *et al.*, *Resonances in $J/\psi \to \phi\pi^+\pi^-$ and $\phi K^+ K^-$*, Phys. Lett. **B607** (2005) 243, `arXiv:hep-ex/0411001`.

[34] G. J. Gounaris and J. J. Sakurai, *Finite-width corrections to the vector-meson-dominance prediction for $\rho \to e^+e^-$*, Phys. Rev. Lett. **21** (1968) 244.

[35] J.-J. Zhu, *Explicit expressions of spin wave functions*, arXiv:hep-ph/9906250.

[36] W. Rarita and J. Schwinger, *On a theory of particles with half integral spin*, Phys. Rev. **60** (1941) 61.

[37] CLEO Collaboration, M. Artuso *et al.*, *Amplitude analysis of $D^0 \to K^+K^-\pi^+\pi^-$*, Phys. Rev. **D85** (2012) 122002, arXiv:1201.5716.

[38] J. Rademacker and G. Wilkinson, *Determining the unitarity triangle gamma with a four-body amplitude analysis of $B^\pm \to (K^+K^-\pi^+\pi^-)_D K^\pm$ decays*, Phys. Lett. **B647** (2007) 400, arXiv:hep-ph/0611272.

[39] D. J. Lange, *The EvtGen particle decay simulation package*, Nucl. Instrum. Meth. **A462** (2001) 152.

[40] M. Jacob and G. Wick, *On the general theory of collisions for particles with spin*, Annals of Physics **7** (1959), no. 4 404 .

[41] J. D. Richman, *An Experimenter's Guide to the Helicity Formalism*, 1984.

[42] S. U. Chung, *General formulation of covariant helicity-coupling amplitudes*, Phys. Rev. D **57** (1998) 431.

[43] L. Evans and P. Bryant, *LHC Machine*, Journal of Instrumentation **3** (2008), no. 08 S08001.

[44] http://cds.cern.ch/record/1087860, 2014.

[45] LHCb collaboration, A. A. Alves Jr. *et al.*, *The LHCb detector at the LHC*, JINST **3** (2008) S08005.

[46] T. Sjöstrand, S. Mrenna, and P. Skands, *PYTHIA 6.4 physics and manual*, JHEP **05** (2006) 026, arXiv:hep-ph/0603175.

[47] P. Golonka and Z. Was, *PHOTOS Monte Carlo: a precision tool for QED corrections in Z and W decays*, Eur. Phys. J. **C45** (2006) 97, arXiv:hep-ph/0506026.

[48] GEANT4 collaboration, S. Agostinelli *et al.*, *GEANT4: A simulation toolkit*, Nucl. Instrum. Meth. **A506** (2003) 250.

[49] GEANT4 collaboration, J. Allison *et al.*, *Geant4 developments and applications*, IEEE Trans. Nucl. Sci. **53** (2006) 270.

[50] M. Pivk and F. R. Le Diberder, *Plots: A statistical tool to unfold data distributions*, Nuclear Instruments and Methods in Physics Research A **555** (2005) 356, physics/0.

[51] Y. Xie, *sFit: a method for background subtraction in maximum likelihood fit*, ArXiv e-prints (2009) `arXiv:0905.0724`.

[52] R. Aaij *et al.*, *The LHCb trigger and its performance*, `arXiv:1211.3055`.

[53] LHCb HLT project, J. Albrecht, V. Gligorov, G. Raven, and S. Tolk, *Performance of the LHCb High Level Trigger in 2012*, J. Phys. Conf. Ser. **513** (2014) 012001, `arXiv:1310.8544`.

[54] LHCb collaboration, R. Aaij *et al.*, *First observations of the rare decays $B^+ \to K^+\pi^+\pi^-\mu^+\mu^-$ and $B^+ \to \phi K^+\mu^+\mu^-$*, `arXiv:1408.1137`.

[55] F. Archilli *et al.*, *Performance of the Muon Identification at LHCb*, JINST **8** (2013) P10020, `arXiv:1306.0249`.

[56] T. Skwarnicki, *A study of the radiative cascade transitions between the Upsilon-prime and Upsilon resonances*, PhD thesis, Institute of Nuclear Physics, Krakow, 1986, DESY-F31-86-02.

[57] L. Breiman, J. H. Friedman, R. A. Olshen, and C. J. Stone, *Classification and regression trees*, Wadsworth international group, Belmont, California, USA, 1984.

[58] A. Hoecker *et al.*, *TMVA - Toolkit for Multivariate Data Analysis*, ArXiv Physics e-prints (2007) `arXiv:physics/0703039`.

[59] R. E. Schapire and Y. Freund, *A decision-theoretic generalization of on-line learning and an application to boosting*, Jour. Comp. and Syst. Sc. **55** (1997) 119.

[60] LHCb collaboration, R. Aaij *et al.*, *Measurement of the track reconstruction efficiency at LHCb*, `arXiv:1408.1251`.

[61] PIDCalibPackage. https://twiki.cern.ch/twiki/bin/view/LHCb/PIDCalibPackage, 2014.

[62] LHCb Collaboration, R. Aaij *et al.*, *Model-independent search for CP violation in $D^0 \to K^-K^+\pi^-\pi^+$ and $D^0 \to \pi^-\pi^+\pi^+\pi^-$ decays*, Phys. Lett. **B726** (2013) 623, `arXiv:1308.3189`.

[63] W. D. Hulsbergen, *Decay chain fitting with a Kalman filter*, Nuclear Instruments and Methods in Physics Research A **552** (2005) 566, `arXiv:physics/0503191`.

[64] BABAR Collaboration, J. P. Lees *et al.*, *Study of the reaction $e^+e^- \to J/\psi\pi^+\pi^-$ via initial-state radiation at BABAR*, Phys. Rev. D **86** (2012) 051102.

[65] Belle Collaboration, Z. Q. Liu *et al.*, *Study of $e^+e^- \to \pi^+\pi^- J/\psi$ and Observation of a Charged Charmoniumlike State at Belle*, Phys. Rev. Lett. **110** (2013) 252002.

[66] BESIII Collaboration, M. Ablikim *et al.*, *Observation of a Charged Charmoniumlike Structure in* $e^+e^- \to \pi^+\pi^- J/\psi$ *at* $\sqrt{s} = 4.26$ GeV, Phys. Rev. Lett. **110** (2013) 252001.

[67] J. Benton, *Finding an Amplitude Model for* $D^0 \to \pi^-\pi^+\pi^+\pi^-$ *using CLEO-c Data*, arXiv:1312.3821.

[68] J. Pychy, *Untersuchungen zur Partialwellenanalyse der Reaktion* $\bar{p}p \to \omega\pi^0$, .

[69] https://www.gemfony.eu, 2014.

[70] F. James, *MINUIT Function Minimization and Error Analysis: Reference Manual Version 94.1*, .

[71] University of Bristol, J. Dalseno and J. Rademacker, *private communication*, 2014.

[72] D0 Collaboration, V. M. Abazov *et al.*, *Search for the X(4140) state in* $B^+ \to J/\psi\,\phi K^+$ *decays with the D0 detector*, Phys. Rev. **D89** (2014), no. 1 012004, arXiv:1309.6580.

[73] CMS Collaboration, S. Chatrchyan *et al.*, *Observation of a peaking structure in the J/psi phi mass spectrum from B(+/-) to J/psi phi K(+/-) decays*, Phys. Lett. **B734** (2014) 261, arXiv:1309.6920.

[74] M. Gronau and D. Pirjol, *Photon polarization in radiative B decays*, Phys. Rev. **D66** (2002) 054008, arXiv:hep-ph/0205065.

[75] LHCb Collaboration, R. Aaij *et al.*, *Observation of photon polarization in the* $b \to s\gamma$ *transition*, Phys. Rev. Lett. **112** (2014) 161801, arXiv:1402.6852.

Erklärung:

Ich versichere, dass ich diese Arbeit selbstständig verfasst habe und keine anderen als die angegebenen Quellen und Hilfsmittel benutzt habe.

Heidelberg, den 15.12.2014   . . . .